

Assessing the Space-Worthiness of Additively Manufactured Liquid Crystal Polymers

E.L. Claassen



Delft University of Technology

Assessing the Space-Worthiness of Additively Manufactured Liquid Crystal Polymers

Master Thesis

Evelien Leandra Claassen

to obtain the degree of Master of Science
at the Delft University of Technology, Faculty Aerospace Engineering,
to be defended publicly on Monday October 28, 2024 at 13:00.

Student number:	5183960	
Thesis committee:	Prof. Clemens A. Dransfeld	TU Delft, Chair
	Dr. Yinglu Tang	TU Delft, Examiner
	Dr. Kunal Masania	TU Delft, Examiner & Supervisor
	Ir. Caroline C.M.C.A.G.P. Houriet	TU Delft, Daily Supervisor

An electronic version of this thesis is available at <https://repository.tudelft.nl/>.

Cover: Photograph of the Van de Graaff accelerator (Radiation Institute, TU Delft)



Acknowledgement

With this thesis, I conclude my master's journey at Delft University of Technology. I would like to extend my heartfelt gratitude to everyone who supported me along the way. Firstly, I am deeply thankful to my supervisors, Dr. Kunal Masania and Ir. Caroline Houriet. This thesis would not have been possible without your guidance. Your expertise and insights helped me grow as a researcher, continually pushing me to explore further. Special thanks to Caroline for being available daily, for teaching me about 3D printing and experimental set-ups, and for assisting with experiments and processing.

I am grateful to the Shaping Matter Lab research group, particularly Dr. Momo (Kathrin) Weiland, for clarifying unexpected chemistry aspects; Dr. Sourav Patranabish, for discussions on LCP and crystallinity; and Derin Goulart Ulcay for our motivational coffee talks. My thanks also to alumni Ir. Sander Wildenborg, who introduced me to SML, and Dr. Vinay Damodaran for help at the Radiation Institute.

Thanks to Ir. Lennart van den Hengel from the TU Delft Radiation Institute for irradiating the samples and Prof. Ferdinand Grozema for post-irradiation visit supervision. From ESA ESTEC, I am grateful to Dr. Ugo Lafont for supervising our visit, René Dohmen for assistance with TVAC, and Ir. Szilvia Szmolka for support with reflectance spectra.

My deepest appreciation goes to the DASML technicians. Dr. Roy Awater and Ir. Chantal de Zeeuw, thank you for helping with DMA and DSC, and Ing. Dave Ruijtenbeek and Ir. Chantal for setting up the tensile testing bench. Special thanks to Ing. Alexander Uithol for always being available to answer my questions and to Victor Horbowiec for diligently handling the challenging task of sawing LCP samples.

I would also like to thank coaches Mirte Brouwer and Rodrigo Fonseca de Carvalho from the Writing Center for organizing the thesis boost writing sessions, which helped me improve my writing and stay motivated.

Lastly, I am thankful to my friends and study partners at TU Delft, who were always there to cheer me up and motivate me. Additionally, my heartfelt gratitude goes to my sister and godmother for constantly checking in, offering help, and proofreading my texts, even though both majored in biology. Lastly, a special thanks to Zanan Sorgucu, my biggest supporter throughout this thesis—what a journey it has been.

*Evelien Claassen,
October 13, 2024*

Abstract

As space exploration advances toward colonization missions on the Moon and Mars, there is an increasing need for lightweight, recyclable, and space-worthy materials. These materials must optimize payload and sustainability by integrating 3D printing and recycling mechanisms, minimizing the need to transport bulky construction materials from Earth and reducing space debris. Additive manufacturing, particularly Fused Filament Fabrication (FFF), offers significant design flexibility, ideal for zero/low gravity environments. However, the relatively low material properties and durability of polymers in space restrict their potential compared to metals. Liquid Crystal Polymers (LCPs) show promise due to their high crystallinity, flame retardancy, and thermotropic properties. Yet, their behavior in space environments remains underexplored. The goal of this research is to evaluate the performance of Vectra A950, an LCP, under electron beam radiation and thermal vacuum (TVAC) exposure, as well as its recyclability after FFF processing.

The study examines the mechanical strength, thermal stability, and crystallinity of 3D-printed LCP under space-like conditions. Samples were subjected to three levels of electron beam radiation and TVAC. Electron irradiation induced annealable color centers, manifesting as a green hue that intensified with higher radiation doses, which could be reversed by annealing for 20 minutes at 200°C. The findings indicate that while exposure to electron beam radiation and TVAC has a measurable impact on the mechanical properties of LCP, the changes are not significant enough to compromise its structural integrity. For irradiated samples, no substantial variations were observed in Young's modulus or ultimate tensile strength (UTS) across different radiation fluences, even after TVAC exposure. However, when exposing unirradiated samples printed at low printing temperatures (295°C and 310°C) to TVAC, slight reductions in Young's modulus were observed with no significant impact on UTS. Thermal analysis revealed that electron beam radiation modestly shifted the β -peak temperature, while TVAC increased the glass transition temperature by 5°C in irradiated samples. Samples exposed to high fluence displayed a permanent decrease in melting temperature by over 7°C, suggesting irreversible changes to the polymer structure.

The study also explored the effects of electron beam radiation, annealing and FFF processing on the recyclability of LCP. Results indicate that while these processes alter thermal and mechanical properties, the effects of annealing and FFF are potentially thermoreversible. FTIR analysis revealed no chemical modifications to the polymer structure, confirming that FFF does not chemically alter LCP, reinforcing its potential for in-situ recycling during planetary exploration. While LCP shows promising recyclability under various conditions, further research is needed to fully understand the reversibility of these changes and their implications for in-situ recycling in space environments.

Overall, the study concludes that, LCP demonstrates mechanical and thermal stability under moderate radiation and thermal vacuum exposure, making it suitable for long-term use in space. Its potential for recyclability, combined with the design flexibility of FFF, supports its viability for space missions, particularly in optimizing sustainability and resource utilization.

Keywords: Liquid Crystal Polymer, electron beam radiation, thermal vacuum, mechanical properties, thermal resistance, Fused Filament Fabrication, annealing, space applications, recyclability.

Table of Contents

ACKNOWLEDGEMENT	I
ABSTRACT.....	III
NOMENCLATURE.....	VIII
LIST OF ABBREVIATIONS.....	VIII
LIST OF SYMBOLS.....	VIII
1 INTRODUCTION.....	1
2 THEORETICAL BACKGROUND	2
2.1 LIQUID CRYSTAL POLYMERS	2
2.1.1 <i>Material Properties and Aerospace Application of LCP</i>	2
2.1.2 <i>Characteristics of Additive Manufactured LCP</i>	3
2.1.3 <i>Crystallinity in LCP</i>	4
2.1.4 <i>The Effect of Annealing on Material Properties and Crystallinity of LCP</i>	4
2.1.5 <i>Recyclability of Vectra®</i>	4
2.2 MANUFACTURING OF LCP THROUGH FUSED FILAMENT FABRICATION	5
2.2.1 <i>Benefits and Considerations for FFF of LCP</i>	5
2.2.2 <i>Impact of FFF on Microstructure of LCP</i>	5
2.2.3 <i>Influence of FFF on Material Properties of LCP</i>	6
2.3 SPACE ENVIRONMENT AND ITS EFFECT ON POLYMERS.....	7
2.3.1 <i>Effect of Radiation on Polymers</i>	7
2.3.2 <i>State of the Art Research on Irradiating Polymers</i>	8
3 RESEARCH DEFINITION	9
3.1 PROBLEM STATEMENT AND RESEARCH OBJECTIVE.....	9
3.2 RESEARCH QUESTIONS.....	9
3.3 RESEARCH DESIGN AND SCOPE	10
3.4 HYPOTHESES	10
3.5 FEASIBILITY	10
4 METHODOLOGY	11
4.1 CHARACTERIZING OF THE MATERIAL PROPERTIES	11
4.1.1 <i>Tensile Testing: Procedure and Equipment</i>	11
4.1.2 <i>Dynamic Mechanical Analysis: Procedure and Equipment</i>	11
4.1.3 <i>Differential Scanning Calorimetry: Procedure and Equipment</i>	12
4.1.4 <i>Fourier Transform Infrared Spectroscopy: Procedure and Equipment</i>	12
4.1.5 <i>UV/VIS/NIR Spectroscopy: Procedure and Equipment</i>	13
4.2 SAMPLE PREPARATION AND FABRICATION PROCESS.....	13
4.2.1 <i>Specifications for Fused Filament Fabrication of LCP Samples</i>	14

4.2.2	<i>Preparation of LCP Sample Cross-Sections for VR Microscopy</i>	14
4.3	EXPOSURE OF LCP TO SIMULATED SPACE ENVIRONMENT	14
4.3.1	<i>Thermal Vacuum Cycling of LCP</i>	14
4.3.2	<i>Electron Beam Irradiation of LCP Using Van de Graaff Accelerator</i>	15
5	COLOR CENTERS FORMED IN LCP DUE TO ELECTRON BEAM RADIATION	16
5.1	RADIATION INDUCED RADICALS AND COLOR CENTERS.....	17
5.2	ANNEALING OF COLOR CENTERS IN IRRADIATED LCP	18
5.3	VR MICROSCOPY ON CROSS-SECTION OF IRRADIATED LCP	19
5.4	UV-VIS-NIR REFLECTANCE SPECTRA OF IRRADIATED LCP EXPOSED TO TVAC	21
6	IMPACT OF SPACE ENVIRONMENT AND FFF ON TENSILE PROPERTIES OF LCP	22
6.1	INFLUENCE OF ELECTRON BEAM AND TVAC ON TENSILE PROPERTIES	22
6.2	INFLUENCE OF TVAC AND PRINTING TEMPERATURES ON TENSILE PROPERTIES	23
7	IMPACT OF SPACE ENVIRONMENT ON DYNAMIC MECHANICAL PROPERTIES OF LCP	26
7.1	INFLUENCE OF ELECTRON BEAM ON DYNAMIC MECHANICAL PROPERTIES.....	26
7.2	INFLUENCE OF ELECTRON BEAM AND TVAC ON DYNAMIC MECHANICAL PROPERTIES.....	27
7.3	INFLUENCE OF ELECTRON BEAM AND ANNEALING ON DYNAMIC MECHANICAL PROPERTIES	28
8	IMPACT OF SPACE ENVIRONMENT AND FFF ON THERMAL PROPERTIES OF LCP	30
8.1	INFLUENCE OF ELECTRON BEAM ON THERMAL PROPERTIES OF LCP.....	31
8.2	INFLUENCE OF FFF ON THERMAL PROPERTIES OF PRISTINE LCP.....	32
8.3	INFLUENCE OF ANNEALING LCP ON THERMAL PROPERTIES	34
9	FTIR ANALYSIS OF SPACE ENVIRONMENT AND FFF EFFECTS ON LCP	37
9.1	INFLUENCE OF ELECTRON BEAM ON FTIR SPECTRA OF LCP	37
9.2	INFLUENCE OF TVAC AND ELECTRON BEAM ON FTIR SPECTRA OF LCP	38
9.3	INFLUENCE OF ANNEALING ON FTIR SPECTRA OF LCP	39
9.4	INFLUENCE OF FFF ON FTIR SPECTRA OF PRISTINE LCP	40
10	DISCUSSION	41
10.1	INFLUENCE OF SPACE ENVIRONMENT ON MECHANICAL PROPERTIES OF LCP	41
10.2	INFLUENCE OF SPACE ENVIRONMENT ON THERMAL RESISTANCE OF LCP	42
10.3	INFLUENCE OF ELECTRON BEAM, ANNEALING AND FFF PROCESSING ON RECYCLABILITY OF LCP	43
11	CONCLUSION	44
12	RECOMMENDATIONS FOR FUTURE RESEARCH	45
	WORKS CITED	46
	APPENDICES	51
	APPENDIX A - IRRADIATION REPORT VAN DE GRAAFF ELECTRON ACCELERATOR	51
	APPENDIX B - DSC DATA PROCESSING	52
	APPENDIX C – COLOR TRACKING OF FFF LCP CROSS-SECTIONS WITH VR MICROSCOPE	53
	APPENDIX D - DMA	55
	D.1 – DMA Loss Modulus Graphs	55

<i>D.2 – Numerical Data DMA</i>	56
<i>D.3 – DMA Comparison</i>	57
APPENDIX E - DSC DATA	58
<i>E.1 - DSC Data Irradiated</i>	58
<i>E.2 - DSC Data Pristine</i>	59
<i>E.3 - DSC Data Annealed</i>	60
APPENDIX F – FTIR CHARACTERISTIC PEAK ASSIGNMENTS.....	62

Nomenclature

List of Abbreviations

<i>3PB</i>	Three-Point Bending
<i>ATOX</i>	Atomic Oxygen
<i>DMA</i>	Dynamic Mechanical Analysis
<i>DSC</i>	Differential Scanning Calorimetry
<i>ELV</i>	End-of-Life Vehicles Directive
<i>EPR</i>	Electron Paramagnetic Resonance
<i>ESA</i>	European Space Agency
<i>ESTEC</i>	European Space Research and Technology Centre
<i>EU</i>	European Union
<i>EVA</i>	Extravehicular Activity
<i>FCO</i>	Forced Convection Oven
<i>FFF</i>	Fused Filament Fabrication
<i>FTIR</i>	Fourier Transform Infrared Spectroscopy
<i>GCR</i>	Galactic Cosmic Rays
<i>HBA</i>	Hydroxybenzoic Acid
<i>HNA</i>	Hydroxynaphthoic Acid
<i>LC</i>	Liquid Crystal
<i>LCP</i>	Liquid Crystal Polymer
<i>LEO</i>	Low Earth Orbit
<i>NASA</i>	National Aeronautics and Space Administration
<i>PEEK</i>	Polyether Ether Ketone
<i>PEI</i>	Polyetherimide
<i>PES</i>	Polyethersulfone
<i>PET</i>	Polyethylene Terephthalate
<i>PLA</i>	Polylactic Acid
<i>RoHS</i>	Restriction of Hazardous Substances
<i>SPE</i>	Solar Proton Event
<i>TA</i>	Manufacturer of thermal analysis instruments
<i>Instruments</i>	
<i>TU Delft</i>	Technical University Delft
<i>TVAC</i>	Thermal Vacuum Chamber
<i>UD</i>	Uni-directional
<i>UTS</i>	Ultimate Tensile Strength
<i>UV</i>	Ultraviolet
<i>WEEE</i>	Waste Electrical and Electronic Equipment
<i>XPS</i>	X-ray Photoelectron Spectroscopy
<i>XRD</i>	X-ray Diffraction

List of Symbols

$^{\circ}\text{C}$	Degrees Celsius
<i>1E0, 1E14, 1E15, 1E16</i>	Scientific notation for electron fluence levels [e^-/cm^2]
<i>A</i>	Ampere (unit of electric current)
<i>C</i>	Carbon
<i>cm</i>	Centimeters (unit of length)
C_p	Heat capacity
<i>D</i>	Fluence
<i>E</i>	Young's modulus
E'	Storage modulus
E''	Loss modulus
e^-	Electron
<i>eV</i>	Electron volt
<i>G</i>	Giga (10^9)
<i>g</i>	Grams
<i>Gy</i>	Grays (unit of radiation dose)
<i>H</i>	Hydrogen
<i>Hz</i>	Hertz (unit of frequency)
<i>I</i>	Beam current
<i>K</i>	Kilo (10^3)
<i>M</i>	Mega (10^6)
<i>min</i>	Minutes
<i>mm</i>	Millimeters (unit of length)
<i>mol%</i>	Mole percent
<i>N</i>	Newton (unit of force)
<i>O</i>	Oxygen
<i>Pa</i>	Pascal (unit of pressure)
<i>rad</i>	(Unit of absorbed radiation dose)
<i>s</i>	Seconds
<i>T</i>	Temperature
$\tan\delta$	Damping factor
T_g	Glass transition temperature
T_m	Melting temperature
T_{mc}	Solidification temperature
T_p	Melting peak temperature
T_{pc}	Solidification peak temperature
α	Glass transition and motion of HNA and HBA moieties
β	Motion of the HNA moiety
ΔH	Enthalpy of Fusion
μm	Micrometer (unit of length)

1 Introduction

As space exploration progresses with missions to Mars and the Moon, the need for innovative materials capable of supporting non-return flights and extensive colonization efforts becomes increasingly critical. To enhance payload efficiency and sustainability, integrating 3D printing and recycling mechanisms into space colonization infrastructure is essential. This approach eliminates the reliance on Earth for transporting bulky construction materials and helps mitigate space debris.

Additive manufacturing, particularly Fused Filament Fabrication (FFF), offers significant design flexibility, performs well in microgravity environments, and promotes sustainability through minimal material waste. However, this technology has been constrained by the relatively low mechanical properties of available polymers compared to metals and the insufficient durability of most polymers in space conditions. The challenge lies in identifying or developing materials that combine high performance with the ability to withstand the harsh conditions of space. Using indigenous raw materials such as lunar or Martian regolith for habitat construction would reduce payload. However, it raises ethical concerns about potential environmental impacts and disruptions to planetary ecosystems. Therefore, there is a pressing need for lightweight and recyclable materials that can be 3D printed and possess high material properties suitable for space applications.

Liquid Crystal Polymers (LCPs) are emerging as a promising material due to their high crystallinity, inherent flame retardancy, and thermotropic properties. Offering mechanical properties comparable to metals, with the added benefit of easier recycling due to the lack of additives in LCP. A notable example is the melt-spun HBA/HNA 73:27 (Vectran™), which has proven its effectiveness in space missions, including Pathfinder airbags, Extravehicular Activity (EVA) gloves, EVA spacesuits, and inflatable habitats (NASA, 2020). Its additively manufactured counterpart, Vectra®, shares the same monomer ratio and is a high-performance plastic with a unique molecular arrangement that shows strong potential for space applications, and is compatible with Fused Filament Fabrication. However, 3D printed LCPs are relatively new materials, and further research is needed to thoroughly evaluate their space-worthiness and the resistance of their material properties to the harsh conditions of the space environment.

This thesis explores the space-worthiness and recycling potential of 3D-printed LCP. It begins with a summary of the literature review, emphasizing the unique properties of LCPs, their advantages in the FFF process, and how the space environment affects polymers. The research definition and feasibility are discussed, leading into a detailed methodology that outlines the experimental approach. This approach entails exposing 3D-printed LCP samples to conditions simulating space, including electron beam radiation and thermal vacuum cycling, followed by an assessment of mechanical and thermal performance, with a focus on material degradation and recyclability potential. The results are analyzed and presented in separate chapters dedicated to each experiment, providing a discussion and interpretation of the data. Finally, the thesis synthesizes the findings, highlights their implications for space applications, and offers recommendations for future research aimed at optimizing the use of LCPs in extraterrestrial environments.

2 Theoretical Background

This chapter summarizes key findings from the literature review conducted prior to this thesis, providing the essential background needed to support the research. For a more comprehensive understanding, the full literature review report is available. First, the properties and advantages of LCPs are explored. Next, the FFF manufacturing process of LCPs is examined, covering the benefits, considerations, and the impact of FFF on microstructure and material properties. Following that, the space environment and its effects on polymers are discussed, with a focus on radiation effects on LCPs and other relevant polymers.

2.1 Liquid Crystal Polymers

Liquid crystals (LCs) are unique materials that combine liquid-like flow properties with crystalline order, resulting in anisotropic behaviors such as optical, electrical, and magnetic properties (Stephen & Straley, 1974; Andrienko, 2018). Liquid crystal polymers (LCPs), a subset of LCs, are classified into thermotropic and lyotropic types (Exner et al., 2015). Thermotropic LCPs (TLCPs) are notable for their suitability for conventional processing methods like Fused Filament Fabrication (FFF) (Nayak & Das, 2015). LCPs consist of rigid mesogenic groups attached to flexible polymer chains, which align and order themselves, impacting mechanical and optical properties (Hamley et al., 1996). These mesogenic groups can form different phases, visible in Figure 1, such as nematic, smectic, and cholesteric, depending on the degree of molecular order.

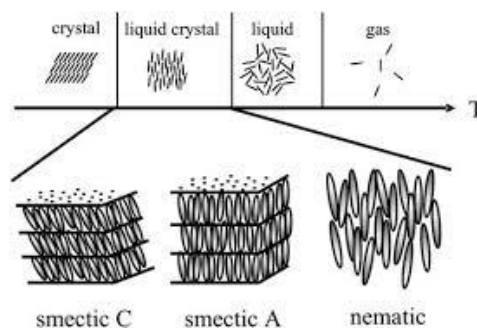


Figure 1: LC Phase and Ordering. Liquid crystal (LC) phase occurs between solid and liquid states, with the alignment of mesogenic groups shown in nematic and smectic configurations. Extracted from (Dierking, 2010)

The nematic phase, common in LCPs, features molecules aligned in one dimension parallel (Noel, 1992; Islam et al., 2014; Mulligan et al., 1996), while smectic phases have more structured layers (Pavel, 2016), and cholesteric phases exhibit twisted molecular orientations (Blackwell & Biswas, 1987). The specific phase behavior depends on how the mesogenic groups are incorporated into the polymer structure, such as in main-chain or side-chain configurations. The balance between the rigidity of the mesogenic groups and the flexibility of the polymer chains determines the phase transitions and overall stability of the LCPs (Collyer, 1996; Pavel, 2016).

In space environments, the balance between molecular order and entropy in LCPs could be disrupted, leading to changes in phase behavior and thermal properties. These changes are likely to manifest as shifts in thermal transition phases, revealed during testing, providing insights into the stability and adaptability of LCPs for space applications. In summary, LCPs combine the structural characteristics of crystalline solids with the fluidity of liquids, making them versatile materials for advanced industrial applications, including potential use in space.

2.1.1 Material Properties and Aerospace Application of LCP

LCPs are highly valued in aerospace due to their high specific strength, stiffness, low weight, durability, and minimal sensitivity to radiation (Celanese, 2013; Jaffe et al., 2018). These properties, combined with their low melt viscosity, enable complex geometries through 3D printing. LCPs surpass traditional polymers such as PLA, PEEK, and PEI in mechanical performance, as shown in Table 1 (Cicala et al., 2018; Gantenbein et al., 2018), with tensile

strengths of 400-500 MPa and a Young's modulus of nearly 18 GPa, and improved toughness after annealing. LCPs exhibit specific strength that approach those of carbon-fiber-reinforced polymers, as shown in Figure 4, while offering the added benefit of recyclability.

Vectran™, a melt-spun thermotropic LCP made from HBA/HNA monomers in a 73:27 ratio, exhibits exceptional mechanical properties, including high crystallinity, flame retardancy, and resistance to creep (Celanese, 2013; Limeneh & Yilma, 2021). It has been used in demanding applications, such as Mars Pathfinder airbags and inflatable habitat structures, where its non-isotropic properties outperform metals (Cadogan et al., 2002; Litteken, 2019). Vectra®, the filament form of Vectran™, was shown to approach the performance of metals in a CubeSat structural bus study (Slejko et al., 2021). LCP was highlighted as the only polymer approaching the performance of the best metal choices for aerospace structures, particularly in terms of weight reduction and faster demise during atmospheric re-entry. LCPs also provide thermal stability and resilience to radiation, making them ideal candidates for future aerospace missions.

Table 1: Ultimate tensile strength and Young's modulus of 3D-printed Materials. Including PEEK, PEI, PLA, and LCP.

	UTS (MPa)	E (GPa)
PEEK	92.7	3.35
PEI	101	3.1
PLA	61.3	2.9
LCP	±450	±18

2.1.2 Characteristics of Additive Manufactured LCP

Vectra® liquid crystal polymers are high-performance materials with rigid, rod-like macromolecules that align into liquid crystal structures when melted, allowing for standard thermoplastic processing like injection molding and fused filament fabrication (Celanese, 2013). Vectra A950 is a thermotropic aromatic random copolyester consisting of 73 mol% hydroxybenzoic acid (HBA) and 27 mol% hydroxynaphthoic acid (HNA). As shown in Figure 2 and Figure 3, HBA contains a single aromatic ring, while HNA features two fused aromatic rings. The rigid structure of HBA contributes to the polymer's stiffness, while HNA introduces flexibility, leading to a lower melting point and reduced crystallinity (Celanese, 2013; Jaffe et al., 2018). This composition enables Vectra to be processed using conventional methods and achieve high mechanical performance, comparable to metals but with a lightweight density of around 1.4 g/cm³.

The material exhibits multiple molecular relaxations, detectable by Dynamic Mechanical Analysis (DMA), including cooperative motions at 100°C and relaxations of HNA and HBA moieties at lower temperatures (Romo-Urbe et al., 2022). Vectra self-assembles into nematic domains above its melting point, with reported melting temperatures ranging from 277°C to 285°C, depending on its thermal history (Chung et al., 1999; Jaffe et al., 2018). Vectra's processing temperatures should remain below 330°C to avoid thermal decomposition and off-gassing (Celanese, 2013). Differential Scanning Calorimetry (DSC) can be used to detect melting regions and changes in crystallinity, which are critical for assessing the thermal and mechanical properties and performance of polymers (Kong & Hay, 2002).

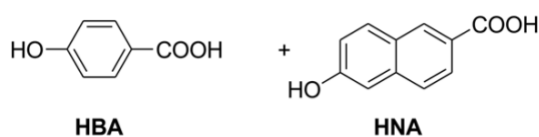


Figure 2: Chemical formula of HBA and HNA monomers. Extracted from (Padias & Hall, 2011)

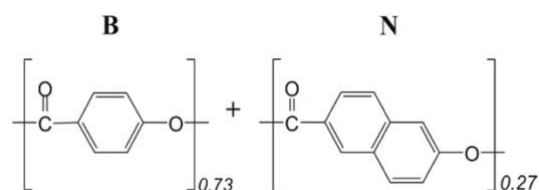


Figure 3: Chemical formula of B-N thermotropic copolyester. Extracted from (Romo-Urbe et al., 2022)

2.1.3 Crystallinity in LCP

Crystallites act as crosslinks within the polymer matrix, causing the material to behave like a crosslinked network, but they break down as the temperature nears the melting point, leading to gradual structural changes (Cowie & Arrighi, 2007). Crystallinity in LCPs refers to the degree of ordered molecular arrangement, which enhances mechanical and thermal properties. Nematic alignment, on the other hand, describes the parallel orientation of rod-like molecules in a liquid crystal phase, where molecules are aligned but not fixed in position. While crystallinity provides structural stability, nematic alignment affects the material's optical and fluidic properties.

Unlike conventional polymers, Vectra® LCP crystallizes differently due to its rigid main-chain structure, requiring significant molecular movement for recrystallization (Jaffe et al., 2018). LCPs undergo two crystallization processes: a rapid transition producing hexagonal packing and a slower transition resulting in orthorhombic packing, though the mechanisms remain unclear (Chung et al., 1999). Changes in crystallinity can be detected using DSC, which measures the melting temperature and enthalpy of fusion, with methods for calculating crystallinity reviewed by Kong & Hay (2002). Several studies have identified two endothermic peaks in LCPs with HBA/HNA copolymers: the first related to a transition from solid to pseudo-hexagonal crystals, and the second marking the transition to the nematic liquid crystal phase (Cheng, 1988; Chung et al., 1999; Kalfon-Cohen et al., 2009). Crystallinity is highly dependent on thermal history and can be influenced by annealing (Lin & Winter, 1988).

2.1.4 The Effect of Annealing on Material Properties and Crystallinity of LCP

Annealing LCPs near their melting temperature can increase crystallinity and mechanical strength, which may be thermo-reversible or lead to non-reversible crosslinking (Yuan et al., 2022). Annealing has been shown to improve mechanical properties by enhancing molecular order and inter-filament adhesion. For example, Gantenbein et al. (2018) observed a 75% increase in shear strength and a slight increase in Young's modulus after 96 hours of annealing at 270°C. Johann et al. (2024) observed a 3-6% increase in sample density and a color shift from bright yellow ochre to dark brown ochre after annealing at 260°C. According to Vectra®'s design guide (Celanese, 2013), annealing in air or nitrogen can raise the heat deflection temperature by 30-50°C. The guide recommends a stepwise annealing process within a 220-250°C range, noting that any color change does not affect material quality.

2.1.5 Recyclability of Vectra®

Vectra® complies with EU sustainability directives like WEEE, RoHS, and ELV, positioning it as a promising candidate for space applications focused on recycling (Celanese, 2013). Research shows that Vectra® is thermo-resettable, as heating to 500°C for 5 seconds removes thermal history (Wissbrun & Yoon, 1989), just below the decomposition temperature of 501°C (Reyes-Mayer et al., 2013). Gantenbein et al. (2018) explored recyclability and found that recycled printed parts had similar fluidity to pristine pellets at 285°C, but annealed parts showed reduced melt flow index (MFI). Lin & Winter (1988) also found that modulus growth is reversible after heating to 320°C. However, annealing may cause irreversible crosslinking (Kim & Economy, 1999), complicating recyclability. Therefore, alternative recycling strategies or the development of LCPs with reversible crosslinking are needed to improve sustainability.

2.2 Manufacturing of LCP through Fused Filament Fabrication

Liquid Crystal Polymers (LCPs) are anisotropic materials, meaning their mechanical properties are strongly influenced by processing techniques, unlike isotropic materials like metals. Fused Filament Fabrication (FFF) is a 3D-printing and additive manufacturing technology that builds objects layer by layer by extruding a thermoplastic filament through a heated nozzle. It offers benefits like reduced material waste, faster production times, and the ability to create complex geometries at lower costs, making it suitable for both prototyping and functional parts. FFF of LCPs is particularly advantageous due to the unique molecular alignment that occurs during the printing process, which significantly impacts mechanical properties (Pavel, 2016). Understanding the effect of processing conditions on the final structure and crystallinity is crucial, as small changes in the chemical composition or processing parameters can greatly affect crystalline quality and the degree of crystallinity (Venkatram et al., 2023). These factors are especially relevant to research focused on ensuring LCP performance in space applications, where thermal stability and structural integrity are critical.

2.2.1 Benefits and Considerations for FFF of LCP

FFF provides significant design flexibility, reduces material waste, and allows for in-situ manufacturing in space environments due to its compatibility with low and zero-gravity conditions. This versatility is particularly advantageous for space missions, where material resources are limited, and the ability to recycle and manufacture on-site can optimize payload efficiency. LCPs, due to their anisotropic nature, align their molecular structure during melting, resulting in easier processing and improved mechanical properties compared to isotropic polymers (Pavel, 2016). The minimal volume change of Vectra A950 during solidification further enhances its performance in FFF, producing high strength and stiffness that approach those of carbon-fiber reinforced polymers without degrading material properties (Gantenbein et al., 2018), as shown in the Ashby diagram in Figure 4. These attributes are especially relevant for structural components in space, where weight reduction and material resilience are paramount. However, the size of printed objects is constrained by the printer's dimensions (Hopkins et al., 2021), which presents limitations in scalability that need to be considered for space infrastructure projects.

2.2.2 Impact of FFF on Microstructure of LCP

During FFF, LCPs develop a core-shell structure due to the alignment of nematic domains in the melt, where the outer shell is highly aligned and solidifies rapidly, while the inner core remains less oriented (Gantenbein et al., 2018), schematic of this in Figure 5. This structure plays a crucial role in the mechanical performance of printed parts, as the alignment of the

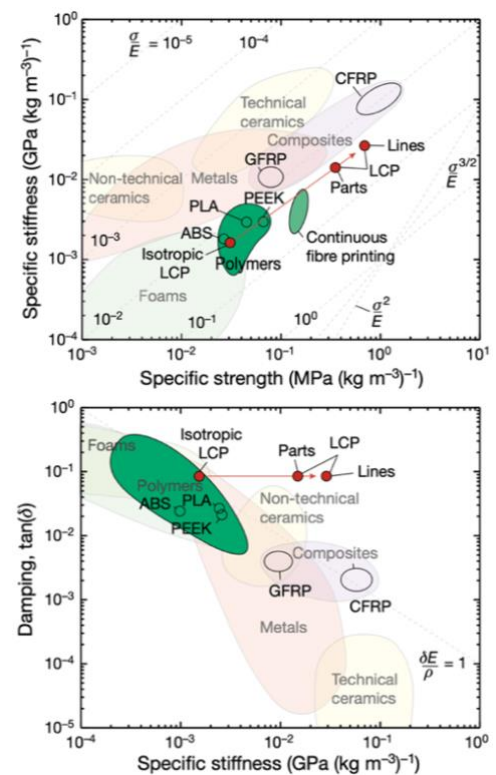


Figure 4: Ashby diagrams. Indicating the specific stiffness and specific strength (top) and damping (bottom) properties of LCP lines and parts compared to the isotropic counterpart and state-of-the-art polymers and reinforced composite materials. Extracted from (Gantenbein et al., 2018)

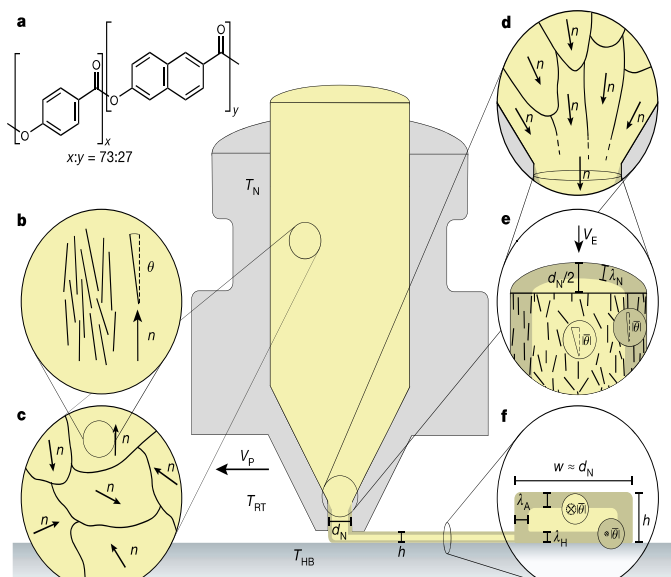


Figure 5: Fused Filament Fabrication (FFF) process for LCPs. Schematic of the FFF process for thermotropic LCPs, showing the formation of a core-shell structure with aligned outer layers and a less ordered core. Extracted from (Gantenbein et al., 2018)

nematic domains during extrusion ensures excellent strength retention. However, even slight variations in the processing conditions can drastically influence the quality of crystallinity and the overall microstructure (Venkatram et al., 2023). Understanding and controlling these variables is crucial, especially for high-performance applications such as space exploration, where the reliability of 3D-printed components is critical for mission success. Post-printing thermal annealing has been shown to enhance molecular weight and stress transfer between filaments, further improving mechanical properties (Johann et al., 2024). This process could be

especially beneficial for long-duration missions where in-situ repair and strengthening of parts may be required.

2.2.3 Influence of FFF on Material Properties of LCP

The alignment of polymer chains during FFF is critical for optimizing tensile strength and Young's modulus, especially when the filaments are printed parallel to the mechanical load direction (Gantenbein et al., 2018). The core-shell structure, with its highly aligned outer layer, significantly enhances material performance. The influence of processing conditions, such as temperature and extrusion speed, plays a substantial role in determining the final properties of the printed parts. Lower layer heights and slower extrusion speeds improve molecular orientation and reduce voids, enhancing overall strength (Johann et al., 2024). This is particularly relevant for space missions, where materials face extreme environmental stresses, and optimizing FFF parameters can significantly enhance the durability and performance of critical components.

Inter-layer adhesion remains a challenge, as the bonds between printed layers are typically weaker than the material itself. Post-printing thermal annealing can mitigate this issue by promoting crosslinking between printed lines, improving both strength and stiffness (Gantenbein et al., 2018). This is especially important for sustainability, as improving inter-filament bonding and overall material integrity through thermal treatment can extend the lifespan of printed parts in space applications, reducing the immediate need for recycling.

In conclusion, the manufacturing of LCPs through FFF presents numerous advantages for space exploration due to its ability to produce lightweight, strong, and recyclable components. However, understanding the critical influence of processing conditions on material properties is key, as even minor adjustments in the chemical composition or processing parameters can lead to significant differences in crystalline quality (Venkatram et al., 2023), emphasizing the importance of precision in manufacturing techniques for space-worthy materials.

2.3 Space Environment and its Effect on Polymers

The space environment presents extreme conditions that significantly impact material durability, including temperature fluctuations, radiation exposure, and atmospheric variations depending on the mission's location (LEO, GEO, the Moon, Mars, or deep space). In Low Earth Orbit (LEO), spacecraft face temperatures ranging from 120°C in sunlight to -160°C in shadow, while the Moon's atmosphere-free surface endures a range from 114°C to -178°C (Plis et al., 2019). Mars, with its thin CO₂ atmosphere, moderates temperatures between -80°C and -60°C. In the vacuum of space, the absence of atmosphere results in extreme temperature differences across an object's surfaces, one side may overheat in sunlight while the other remains freezing in shadow. Without air to conduct heat, these temperature extremes create unique thermal challenges, which are simulated in Thermal Vacuum Chambers (TVAC) to assess material performance under thermal cycling for space missions.

The space environment exposes materials to various types of radiation, including galactic cosmic rays (GCRs), solar proton events (SPEs), and radiation belts like the Van Allen belts. GCRs are high-energy particles from outside the solar system that can penetrate deeply and damage materials by displacing atoms and breaking molecular bonds (Waller, 2020). SPEs consist of high-energy protons released during solar flares, particularly impacting spacecraft in low Earth orbit (Waller, 2020). In Earth's radiation belts, energetic electrons and protons can damage spacecraft surfaces, with electrons ranging from 10 keV to 2 MeV and protons from 10⁻⁴ to 10 MeV (Plis et al., 2019). UV and X-ray radiation from the Sun also degrades polymers by breaking chemical bonds, particularly in LEO and GEO (Briskman et al., 1999).

2.3.1 Effect of Radiation on Polymers

Radiation affects polymers by causing chain scission and cross-linking, leading to changes in molecular weight, mechanical strength, thermal properties and viscosity (Waller et al., 2017; de Groh et al., 2018). Polymeric materials containing crystallinity, like Vectra®, can produce trapped electrons and radicals when irradiated, resulting in color changes and imperfections in their crystalline structure (Dawes et al., 2007). High radiation doses generally reduce tensile strength and make materials brittle (Plis et al., 2019).

Most polymers can be penetrated by electrons with energies below 3 MeV, but substantial radiation doses are needed to achieve significant polymer modifications (Oproiu et al., 2000). Radiation effects on polymers primarily involve cross-linking and degradation (main-chain scission), those that undergo cross-linking (often with chemical promoters) and those that degrade into lower molecular weight products, becoming hard and brittle with high radiation doses (Oproiu et al., 2000). One does not exclude the other from occurring, albeit to a lower degree (Clough, 2001). Irradiation effects typically increase with increasing temperature. Crosslinking is limited below the glass transition temperature (T_g) due to the rigidity of the glassy state and the formation of stable radicals. Above T_g , crosslinking generally increases, but so do scission processes (Clough, 2001). High radiation doses may initially increase tensile strength due to cross-linking but can later decrease it as excessive cross-linking leads to brittleness (Plis et al., 2019).

The irradiation environment influences polymer degradation. When oxygen is present, radicals may form peroxides, accelerating scission and degradation, while inert environments stabilize radicals, promoting cross-linking (Dawes et al., 2007). Electron beam irradiation in

air can significantly reduce the tensile strength and melting temperature of amorphous and semi-crystalline polymers, while irradiation in nitrogen shows minimal effects (El-Naggar et al., 1989).

Even for highly aromatic polymers, which are, relative to nonaromatic polymers, resistant to irradiation with electron beam or gamma-ray, radiating in vacuum or in the presence of oxygen can drastically influence the material. Aromatic polymers remain stable and exhibit no changes in physical properties when irradiated in a vacuum, even after high doses of radiation (Hanks & Hamman, 1971). However, in the presence of oxygen, aromatic polymers can undergo significant changes in their physical properties (Brown & O'Donnell, 1979; Dawes et al., 2007).

Aromatic polymers are inherently more resistant to radiation than aliphatic polymers due to their ability to absorb energy without bond rupture. The presence of aromatic rings significantly mitigates the effects of radiation, with higher aromatic content offering increased protection by minimizing both chain scission and cross-linking (Dawes et al., 2007). Vectra A950, a highly aromatic LCP, benefits from this characteristic, as its HBA moiety contains one benzene ring, and the HNA moiety features two fused benzene rings (naphthalene). This structure is expected to provide greater radiation resistance compared to polymers lacking aromatic content.

2.3.2 State of the Art Research on Irradiating Polymers

High radiation doses generally damage the crystalline structures of semi-crystalline polymers like PET, reducing their melting points and altering thermal properties through cross-linking and chain scission (Dawes et al., 2007). Gamma radiation increases the glass transition temperature (T_g) in polymers such as PEEK, indicating enhanced mechanical properties. Aromatic polymers like PET and PES experience less degradation from proton irradiation than electron irradiation due to their structure (Briskman, 2003). Vectra A950, with its high aromatic content, is expected to behave similarly, maintaining structural stability under high radiation doses.

NASA identified Vectran™ as a top performer for lunar regolith bags due to its exceptional strength and elongation under various radiation types, including electron beam and gamma radiation. Vectran™ demonstrated minimal degradation, with electron beam irradiation reducing strength by only a small margin (Smithers et al., 2007). This research supports the use of LCPs like Vectra® in space applications, where radiation resistance is critical for long-term durability.

In summary, Vectra A950's aromatic structure provides superior radiation resistance, making it a promising candidate for space applications where high radiation exposure is inevitable. Understanding the balance between cross-linking and chain scission is crucial to predicting the material's performance under these conditions, as observed in other polymers. Given the severe conditions imposed by the space environment, including extreme temperature fluctuations and intense radiation, thorough testing and analysis are essential to ensure the longevity and functionality of materials in space missions.

3 Research Definition

This chapter outlines the research focus and objectives for evaluating 3D-printed LCP's performance in space-like conditions. It also defines the key research questions and summarizes the hypothesis and study feasibility.

3.1 Problem Statement and Research Objective

As space exploration progresses toward returning to the moon and human ventures to Mars, the need for lightweight, reusable, and durable materials is growing. LCPs show potential due to their high crystallinity, flame retardancy, and thermotropic properties, but their response to space environments remain underexplored, requiring further research.

This research aims to evaluate the resistance of 3D-printed LCP under space conditions, with a focus on its performance when exposed to radiation and thermal vacuum environments. Key areas of investigation include mechanical robustness, thermal resilience, and recycling potential, including comparisons made across different stages of fused filament fabrication.

Understanding LCP's resistance to space conditions is essential for sustainable space missions, especially for resource utilization and habitat construction on Mars. This research supports the development of space-worthy materials by evaluating the effects of temperature and radiation on LCP, with a focus on missions between Earth, the Moon, and Mars.

3.2 Research Questions

The liquid crystal polymer Vectra A950 is used in this research to evaluate the space-worthiness of 3D-printed LCPs. In this context, space-worthiness refers to the material's ability to maintain its mechanical, thermal, and chemical integrity when exposed to simulated space conditions, including radiation, thermal cycling, and vacuum. Space-worthy materials should not only resist degradation in the harsh space environment but also promote sustainability by enabling recycling and reuse, which reduces the need for resupply missions. The core research question guiding this study is:

“What is the impact of exposure to electron beam radiation and TVAC on the material properties of 3D-printed LCP, and how does this influence its space-worthiness?”

To answer this, the research will analyze changes in mechanical properties, thermal stability, and recyclability after exposure to space-like conditions and FFF processing. Specifically, the following sub-questions are addressed:

- I. How do electron beam radiation and thermal vacuum cycling affect the **mechanical properties** of LCP?
- II. How do electron beam radiation and thermal vacuum cycling affect the **thermal resistance** of LCP?
- III. How do electron beam radiation, annealing and FFF processing affect the **recyclability** potential of LCP for space applications?

The first question evaluates the material's ability to retain strength, stiffness, and structural integrity under space-like conditions, which is critical for ensuring its long-term performance in spacecraft or habitat construction. The second question assesses thermal stability, crucial for understanding how the material responds to the extreme temperature fluctuations and radiation exposure typical in space environments. Finally, the third question focuses on recyclability, which is essential for sustainability in space missions by allowing the material to

be reused, minimizing waste, and reducing reliance on Earth-bound resupply. By addressing these questions, the study provides a comprehensive evaluation of the space-worthiness of LCP, determining not only its durability and performance under space conditions but also its potential for recycling, which is key for sustainable space exploration.

3.3 Research Design and Scope

The study examines how electron radiation and thermal vacuum affect material properties of LCP. It is experimental, with samples exposed to varying levels of electron radiation and thermal vacuum. Random assignment to different exposure groups minimizes printing anomalies and ensures result validity, although full randomization is limited by the availability of electron radiation equipment at TU Delft. The research focuses exclusively on Vectra A950 and does not cover all space environmental factors. Only one type of radiation will be used due to availability constraints. The study will assess tensile strength, flexural modulus, and thermal resistance to evaluate material degradation and changes in crystallinity before and after radiation exposure. Effects of recycling and reprinting will be examined at different FFF stages. Equipment from TU Delft will be used, along with TVAC and spectral absorptance resources provided through ESA in collaboration with PhD candidate Caroline Houriet.

3.4 Hypotheses

Based on previous research and the properties of LCPs, several hypotheses can be made about the performance of Vectra A950 under space-like conditions, contributing to assessing its suitability for space missions. Exposure to electron radiation is likely to alter the mechanical properties of LCP. Specifically, it is hypothesized that electron beam radiation will induce crosslinking within the polymer matrix, potentially increasing its tensile strength and stiffness while reducing ductility. However, excessive radiation could also lead to degradation, like chain scission, weakening the material's overall mechanical performance.

The thermal vacuum environment is likely to affect the thermal resistance of LCP Vectra A950. It is anticipated that exposure to thermal vacuum conditions will reveal changes in the polymer's thermal stability, with possible increases in glass transition temperature (T_g) due to polymer hardening. The interaction between high thermal stress and low pressure may also result in altered thermal conductivity and reduced thermal performance over time.

Additionally, it is hypothesized that repeated exposure to radiation and thermal vacuum may negatively impact the recycling potential of LCP Vectra A950. The structural changes caused by crosslinking and chain scission may reduce the polymer's ability to be remelted and reprocessed, complicating in-situ recycling for space applications. However, careful control of radiation dosage and annealing processes may help maintain or restore some level of recyclability, making LCP a viable candidate for sustainable long-term space missions.

3.5 Feasibility

The research on the effects of electron radiation and thermal vacuum on LCP Vectra A950 is feasible and relevant for advancing space materials science. The study is expected to fit within the timeframe of a master thesis (39 weeks), covering sample preparation, exposure, and analysis. Ethical considerations are minimal, focusing on safety protocols for radiation handling. Cooperation with TU Delft and ESA through PhD candidate Caroline Houriet is essential for access to equipment and expertise. Costs are managed due to the use of existing resources and collaborative support. All necessary tools and facilities are available, ensuring the research can be conducted effectively while addressing space material testing challenges.

4 Methodology

This chapter outlines the methodology used in this research. It begins with an explanation of how the material properties will be assessed, including the testing and the parameters selected for these tests. Next, the process for sample preparation and fabrication is detailed. Finally, the methods used to simulate the space environment are discussed.

4.1 Characterizing of the Material Properties

Mechanical properties will be evaluated under both static and dynamic loading conditions. Static load testing will include tensile testing to determine the modulus of elasticity (Young's modulus) and ultimate tensile strength. Dynamic load testing will be conducted using DMA with three-point bending to examine the influence of temperature on damping factor ($\tan \delta$), and storage and loss moduli.

Thermal properties will be analyzed using both DMA and DSC. The glass transition temperature (T_g) will be determined from DMA data, as DMA provides greater sensitivity to T_g by directly measuring mechanical and viscoelastic property changes with temperature. For semi-crystalline materials with low amorphous content, such as LCP Vectra A950, it is difficult to detect T_g with DSC. DMA will further reveal any changes in molecular relaxations or motions of LCP due to exposure, while DSC will provide insights into the effects of irradiation on melting temperatures and the enthalpy of fusion.

DSC will also assess the impact of Fused Filament Fabrication (FFF) on LCP, with the goal of exploring in-situ recycling options for planetary exploration. Additionally, FTIR will be used to detect molecular alterations and compositional changes caused by FFF, electron irradiation, and TVAC exposure.

4.1.1 Tensile Testing: Procedure and Equipment

The study will utilize the tensile benches in the TU Delft Aerospace aircraft hall, specifically the Zwick Universal Test Machine with a 10 kN load cell and hydraulic grips, under the supervision of Ing. Dave Ruijtenbeek. In addition to examining the effects of electron beam radiation and TVAC, the influence of different printing temperatures and orientations will also be investigated for samples exposed to TVAC. Unidirectional tensile specimens with a nominal width of 5 mm, length of 110 mm, and thickness of 2 mm were printed with filament orientation at 0° to the testing direction. Specimens with a 90° print-filament orientation were printed in a dogbone shape, 20 mm wide, 65 mm tall, and with a constant gauge length of 20x10x4 mm, shown in Figure 6.

To ensure proper grip and avoid slippage during testing, glass-fiber composite tabs were glued to the samples, with a 45-degree bevel to optimize load transfer, maintaining a gauge length of 65 mm. Specimens were tested at a displacement rate of 1 mm/min, with data collected for at least five samples. A custom MATLAB script, developed by Caroline Houriet, was used for data processing and analysis.

4.1.2 Dynamic Mechanical Analysis: Procedure and Equipment

Dynamic Mechanical Analysis (DMA) was performed using the TA Instruments RSA G2 DMA bench, available in the physics lab of the TU Delft Aerospace aircraft hall, under the supervision of Dr. Roy Awater. Three-point bending set up with a 25 mm span was selected

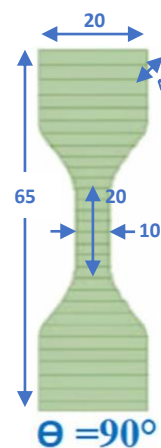


Figure 6: Tensile Testing Dogbone-shape Sample. Including dimensions in millimeters.

for DMA testing to provide the purest deformation mode b(DMA Basic Theory & Applications Training, n.d.)y & Applications Training, n.d.). The printed LCP samples were 2 mm thick, 5 mm wide and 30 mm long with a 0° orientation along the span. Additionally, samples were printed and tested with a 90° orientation, however the results did not differ much when comparing the influence of radiation, so the results of the UD90 samples will not be included in this report.

The analysis measured the influence of temperature on the storage modulus (E'), loss modulus (E''), and damping factor ($\tan \delta$). Material behavior with temperature can indicate molecular changes in the material. Testing was conducted at a frequency of 10 Hz and 0.1% strain, across temperature ranges of 22°C to 200°C and 22°C to 280°C using a forced convection oven (FCO) with a heating rate of 3°C/min. A static force of 1 N was applied, with an offset force to maintain contact between the sample and the probe, as three-point bending does not use clamps. A custom Python™ script was created to process and analyze the data.

4.1.3 Differential Scanning Calorimetry: Procedure and Equipment

Differential Scanning Calorimetry (DSC) was conducted on a TA Instruments Discovery DSC 250 in the TU Delft Aerospace aircraft hall, supervised by Dr. Roy Awater. DSC reveals thermal changes, structural modifications, and degradation due to radiation exposure or simulated recycling. DSC can simulate recycling by subjecting materials to thermal cycling, mimicking filament production, part printing, and repeated recycling cycles. It also assesses crystallinity shifts by detecting heat flow during phase transitions, providing insights into radiation-induced changes in crystalline structures, which is crucial for evaluating material integrity. DSC was performed on samples exposed to three levels of electron beam irradiation to determine if chain scission or crosslinking occurred, and on pellets and filament annealed in a vacuum oven at 240°C for 0-5 hours, with increments of one hour, to assess the impact of FFF and annealing on LCP recycling.

For LCP Vectra, hermetically sealed aluminum pans were used to securely contain the samples, preventing de-lamination from pushing open the lid and avoiding evaporation or loss of content, which could cause inaccurate measurements or damage to the instrument. Nitrogen was used as the gas type, and standard DSC calibration was performed with sapphire and an empty pan for temperature and enthalpy. The DSC procedure included five cycles: three heat cycles from 25°C to 320°C, and two cool cycles from 320°C to 25°C, with a constant heating rate of 10°C/min. The limit of 320°C was set to remain safely below the decomposition temperature. A custom MATLAB script was created to process and analyze the data. Data processing details are provided in Appendix B.

4.1.4 Fourier Transform Infrared Spectroscopy: Procedure and Equipment

Spectrometer analysis is used to detect structural or elemental changes by measuring light wavelengths. FTIR spectroscopy specifically measures infrared absorption to reveal molecular alterations and compositional changes. The resulting graphs display the energy absorbed by the sample at different wavelengths, where the peak locations, shapes, and heights correspond to specific chemical bonds in the material. FTIR testing is valuable for investigating modifications in polymeric materials due to environmental factors, such as radiation or TVAC exposure, and helps identify the root causes of these changes. Analyzing these spectra requires knowledge of degradation byproducts and their corresponding peak locations.

FTIR analysis was conducted using a Spectrum 100 FTIR Spectrophotometer (PerkinElmer) equipped with a universal ATR sampling accessory and a Diamond/ZnSe crystal. The spectra were recorded over a wavenumber range of 4000 cm^{-1} to 600 cm^{-1} , with a resolution of 2 cm^{-1} . Measurements taken in June (332 days post-exposure) were averaged over 32 scans, while those in December (139 days post-exposure) were averaged over 8 scans. Data analysis was performed using SpectraGryph v1.2.16.1. Variations in peak sizes were influenced by the method and order of normalizing and smoothing data sets, leading to differences in curve intensity and resulting in changes to which sample exposure showed the largest amplitudes. The following data processing steps were performed in the order shown:

1. Normalization by Peak: Each spectrum's highest peak within the visible range (4000-600 cm^{-1}) was set to a value of 1.
2. Baseline Correction: An adaptive baseline was applied with a coarseness of 15 and an offset of 0.
3. Smoothing: Data was smoothed using the built-in Savitzky-Golay algorithm with an interval of 10 and a polynomial order of 3.
4. Selective Baseline Smoothing: A baseline selective function was applied with a vertical gradient of 0.5 and a mapped y-axis range relative to 100% of the spectrum.

4.1.5 UV/VIS/NIR Spectroscopy: Procedure and Equipment

A Cary 5000A UV/VIS/NIR spectrophotometer (Agilent, USA) equipped with an internal integrating sphere was utilized to measure the total reflectance of the samples across a wavelength range of 2500 to 250 nm under ambient conditions. The reflectance data was calibrated using a Spectralon diffuse standard to ensure accuracy. Reflectance measurements were taken from the tensile testing samples before the mechanical tests were conducted.

4.2 Sample Preparation and Fabrication process

Vectra A950 filament and pellets were provided by NematX AG (Switzerland). Filament specification printed on the spool label are: [NematX NF-161 02.12.2021 1060gr Mean: 1.74 mm min: 1.72 mm max: 1.77 mm]. The samples were irradiated with an electron beam using a Van de Graaff accelerator, which provided a placement area of 300 mm by 80 mm, shown in Figure 7B, limiting the size and number of samples per radiation dose. The Thermal Vacuum Chamber (TVAC) had a table size of approximately 210x300 mm (roughly A4 dimensions), shown in Figure 7A, accommodating all unirradiated samples and three batches with varying irradiation fluences simultaneously during a single run. Tensile samples were designed with dimensions of 110 x 5 x 2 mm for UD0, and 65 x 20 x 4 mm for UD90 dogbone-shaped samples. DMA samples had similar dimensions to the UD0 tensile samples but were shorter, at 40 x 5 x 2 mm.

The decision to conduct DSC analysis was done after the samples were irradiated, as a result no dedicated design was made for these samples. Instead, DSC samples were 'punched' out of the DMA samples using a hammer and a circular die with a diameter of 3 mm. These samples were previously exposed to a temperature cycle from 22°C to -120°C, which is assumed not to affect crystallinity since crystallization typically occurs at temperatures around 40°C below the solid-to-nematic transition (Romo-Urbe et al., 2022). No evidence was found indicating that these temperature ranges can alter the crystallinity of LCP Vectra.

The pellets used for DSC are from a different, unidentified batch than the filament, which may affect the data. Ideally, pellets and filament from the same batch would minimize variability,

but such resources were unavailable. The filament and printed samples are from the same batch.

4.2.1 Specifications for Fused Filament Fabrication of LCP Samples

The Prusa slicer software was used to design and slice the print files, and the samples were printed using a Prusa i3 MK3S+ 3D printer with a layer height of 0.1 mm, a line width of 0.35 mm, and a deposition speed of 35 mm/s. All irradiated samples were printed with a bed temperature of 90°C and a nozzle temperature of 295°C. For pristine tensile samples and those exposed to TVAC, four different nozzle temperatures (295°C, 310°C, 325°C, and 340°C) were used. Adhesion was applied to ensure the samples remained in contact with the PEI printing bed, especially for tensile samples with a high length-to-width ratio, which tend to shrink and detach from the bed when printed in the length direction, potentially causing deformities.

4.2.2 Preparation of LCP Sample Cross-Sections for VR Microscopy

To investigate the cross-sections post-exposure, DMA samples, which had previously been subjected to a temperature range of -120°C to 25°C, were sawed in half before being embedded in resin. A Dremel tool with a diamond blade was used for sawing while the samples were clamped to prevent delamination. To remove any edge melting caused by sawing, over 1 mm of the sample length was sanded off. The samples were then embedded in resin. Once the resin coin had cured, the samples were polished using Struers Tegramin-20, an automatic polishing machine, following a program designed for fragile fibers.

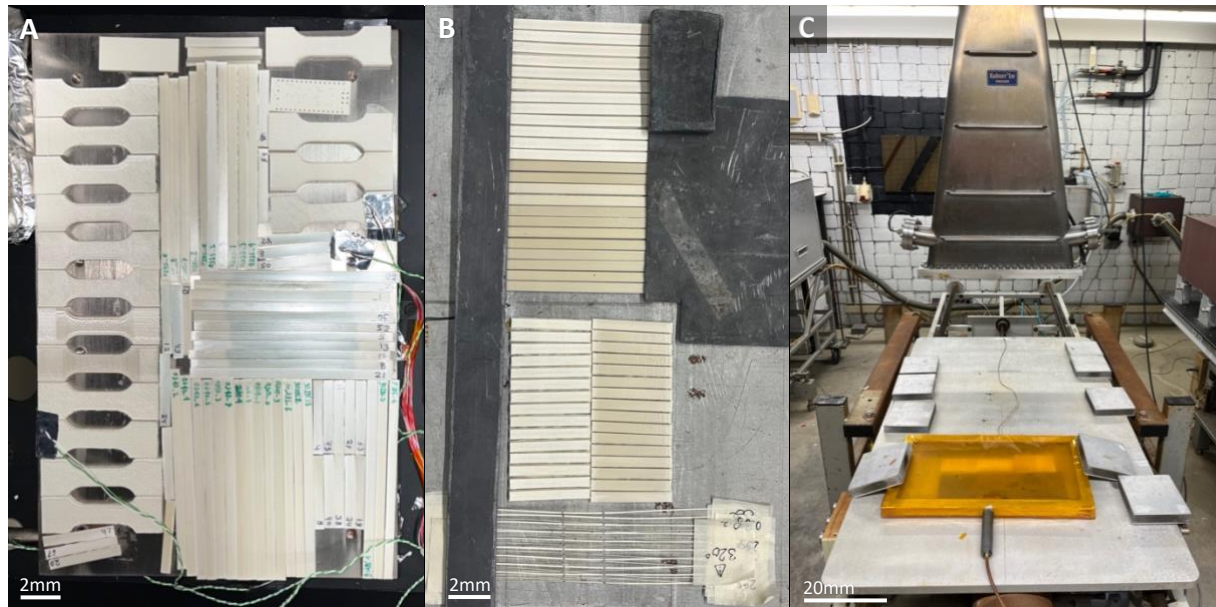


Figure 7: Exposure Set-up for TVAC and Electron Beam Irradiation. A. Sample placement on the 300x210mm table inside the thermal vacuum chamber (TVAC). **B.** Sample arrangement on the 300x80mm table for high-dose electron beam irradiation. **C.** Nitrogen gas flushing during irradiation to maintain controlled conditions, keeping the sample temperature below 22°C.

4.3 Exposure of LCP to Simulated Space Environment

To simulate space environment, LCP was exposed to TVAC and electron beam irradiation.

4.3.1 Thermal Vacuum Cycling of LCP

The thermal vacuum cycling (TVAC) test was conducted over 25 cycles, where the temperature ranged from -100°C to 100°C. The test maintained a vacuum level between 10^{-6}

mbar and 10^{-7} mbar throughout the process. Each cycle included a heating rate of 5°C per minute and a dwell time of 30 minutes at the temperature extremes. This test was carried out in a specialized chamber at the ESA ESTEC facility, shown in Figure 7A.

4.3.2 Electron Beam Irradiation of LCP Using Van de Graaff Accelerator

The samples were irradiated with high-energy electrons (1 MeV) using a Van de Graaff accelerator at the Radiation Institute of TU Delft, shown in Figure 7C, on July 28, 2023. Prior to exposure, the samples were cleaned, weighed, and labeled. They were divided into three groups with increasing fluence intensities: low fluence at $1 \times 10^{14} \text{ e}^{-}/\text{cm}^2$, mid fluence at $1 \times 10^{15} \text{ e}^{-}/\text{cm}^2$, and high fluence at $1 \times 10^{16} \text{ e}^{-}/\text{cm}^2$. In figures and graphs, scientific notation (i.e. 1E14, 1E15, and 1E16) will be used to indicate what is referred to in the text as low fluence, mid fluence, and high fluence. "Pristine" refers to samples that have not undergone any exposure, while "unirradiated" describes samples not exposed to electron radiation but subjected to TVAC or annealing, as specified. In scientific notation, the unit is omitted, but these notations specifically denote fluence with the unit e^{-}/cm^2 .

Table 2: Electron Beam Exposure Doses and Times, for a Nylon calibration sample and the three exposure intensities used in the experiment on LCP samples, with their beam current (I), fluence (D), calculated received dose in kGy and in Mrad, associated mission type and dose for direct exposure to space (Fruit et al., 2017), and a color code used to label the fluence levels. The dose was calculated with the formula: $\text{Dose} = \text{Fluence} \times \text{Dose}_{\text{calibration}} / \text{Fluence}_{\text{calibration}}$.

Sample ID's	I (μA)	D (e^{-}/cm^2)	Dose rate ($\text{e}^{-}/\text{cm}^2/\text{s}$)	Time (s)	Dose (kGy)	Dose (Mrad)	Space mission type & dose (Mrad)		Color code
Nylon (calibration)	62.24	1.20E+14	5.00E+11	240	35	3.5			1E0
Low: 1E14	64.8	1.00E+14	5.20E+11	193	29.2	2.92	LEO 1	1	1E14
Mid: 1E15	64.4	1.00E+15	5.17E+11	1935	292	29.2	LEO 2	18	1E15
High: 1E16	67.5	1.00E+16	5.42E+11	18461	2917	292	GEO	180	1E16

Table 1 provides details on the varying beam current, dose rates per fluence, exposure time, the corresponding doses received in kilograys (kGy) and megarads (Mrad), associated space mission types with their respective doses when directly exposed to space (Fruit et al., 2017), and the color codes used to label fluence intensities. The full radiation report can be found in Appendix A. Nylon samples were calibrated by exposing them to a dose rate of $5 \times 10^{11} \text{ e}^{-}/\text{cm}^2$ for 240 seconds, resulting in a dose of 35 kGy. A linear relationship is assumed between the beam current (I, in μA) and the dose rate ($\text{e}^{-}/\text{cm}^2/\text{s}$), as well as between fluence (e^{-}/cm^2) and dose (Gy) across different materials. The dose is calculated by interpolating from the calibration sample using Equation 1, followed by converting from kGy to Mrad, where $1 \text{ Gy} = 100 \text{ rad}$, and $1 \text{ kGy} = 0.1 \text{ Mrad}$.

$$\text{Dose} = \frac{\text{Fluence} \times \text{Dose}_{\text{calibrated}}}{\text{Fluence}_{\text{calibrated}}} \quad \text{Eq. (1)}$$

The samples were flushed with nitrogen, and the table temperature was carefully maintained below 22°C , well below the glass transition temperature. Each sample was positioned according to its original orientation on the print bed during the printing process. For tensile samples, only the central portion, approximately 65 mm in length, was exposed, while both edges, around 22.5 mm each, were shielded with lead to protect them from electron exposure; these shielded areas are where the tabs for tensile testing are attached. In contrast, DMA samples were fully exposed to the radiation.

5 Color Centers Formed in LCP due to Electron Beam Radiation

After electron beam irradiation, the samples changed from their original soft beige/yellow color to green/teal, with the darkest shade observed at the highest fluence. The original color remains visible at the outer edges of the tensile samples, where lead shielding prevented irradiation. Figure 8 shows that the green color completely fades over time for the low fluence samples within 20 days and for the mid fluence samples within 54 days. The green color in the high fluence samples does not fully disappear but fades over time, reaching a plateau around 20 days. Since this color change was unexpected, and the fading was noticed only after 20 days, no intermediate pictures were taken to document the progression.

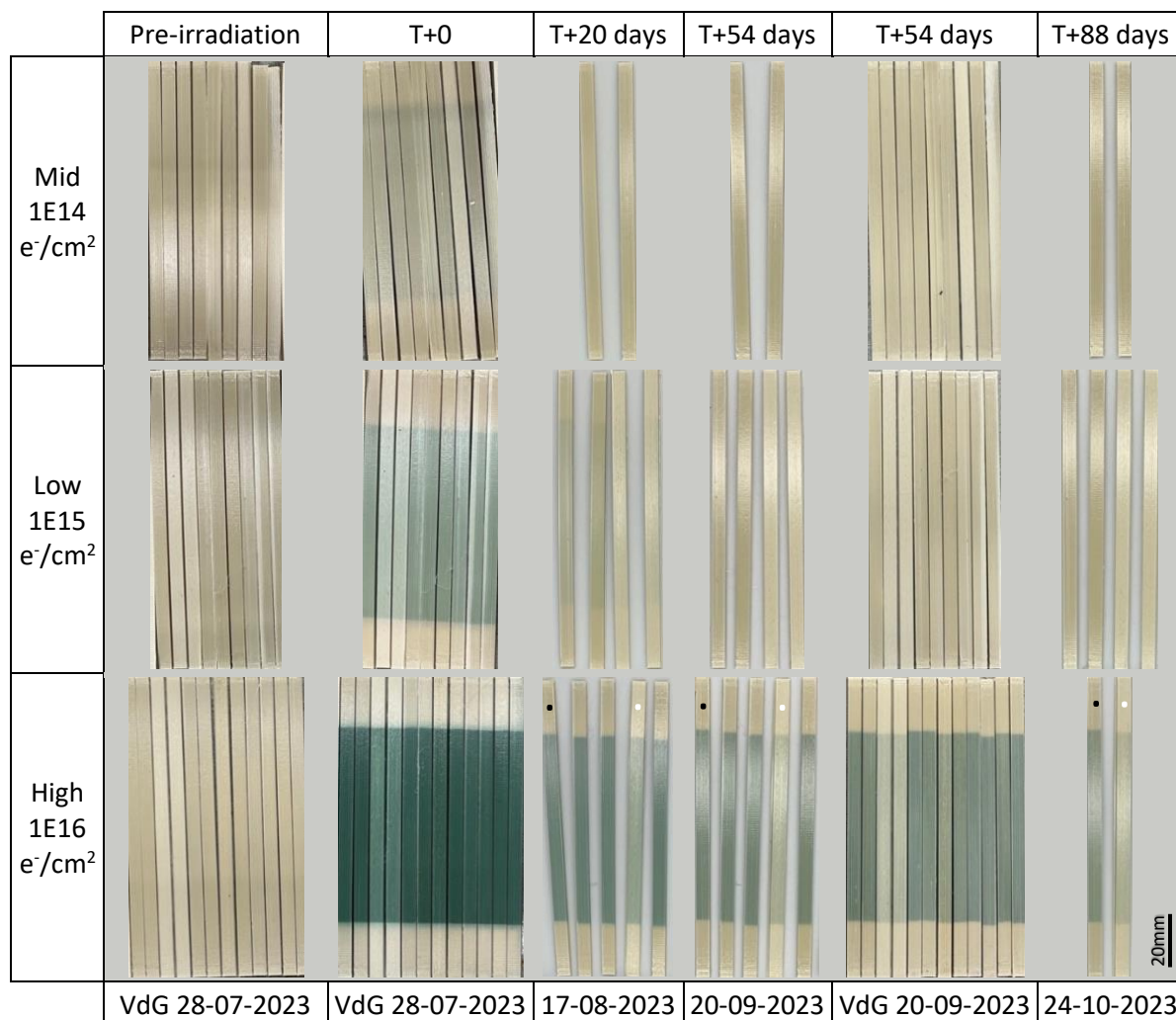


Figure 8: Color Centers after exposure to electron beam radiation in LCP and the disappearance over time. The original color remains visible at the outer edges of the tensile samples, where lead shielding was used to prevent irradiation. After 20 days, the surface coloration reached a plateau for the high fluence samples and completely disappeared for the low fluence samples. By 54 days, photos taken at the Van de Graaff accelerator showed that the color had completely faded for the mid fluence samples. Black and white dot indicate identical high fluence samples.

The color observed in polymers after electron beam irradiation can be attributed to trapped electrons within the polymer matrix, a phenomenon known as color centers. Color centers, in general, are imperfections within a material's crystal or polymer lattice where an electron or a missing electron alters the optical properties, leading to visible discoloration. There are two primary types of radiation-induced color centers reported in the literature: annealable and permanent (Clough et al., 1996; Hou et al., 2019; Wallace et al., 1993).

Annealable centers can be removed through thermal annealing, where trapped electrons are released, especially above the glass transition temperature. Over time, these centers may also fade through self-quenching and oxygen-quenching, where molecular motion or external oxygen neutralizes the radicals. Permanent color centers, on the other hand, persist and are unaffected by heat (Hou et al., 2019). Understanding these processes is crucial for assessing radiation effects on polymers, especially in space environments.

5.1 Radiation Induced Radicals and Color Centers

Radiation exposure can generate radicals in polymers, which can lead to the formation of annealable color centers. Free radicals are highly reactive due to their unpaired electrons, and they quickly react with other molecules or radicals to stabilize. Unstable radicals, the most common form, have short lifespans in environments with reactive species like oxygen, which leads to rapid quenching or neutralization (Von Sonntag, 2003). In oxygen-rich environments, chain scission occurs via oxyl radicals as intermediates, breaking the polymer chains. However, in vacuum or inert atmospheres, where oxygen is absent, self-quenching can occur. In this case, radicals interact with each other, resulting in either crosslinking or chain scission, depending on the polymer's structure (Ashfaq et al., 2020). Both oxygen quenching and self-quenching processes can be accelerated by heating, especially above the polymer's glass transition temperature, where increased molecular motion promotes radical interactions.

Trapped radicals form when reactive species become immobilized within the polymer matrix, often in crystalline regions or defects. In rigid polymers like LCPs, these radicals may remain stable for extended periods, especially in the absence of oxygen, as limited molecular movement prevents further reactions. In semi-crystalline polymers, trapped radicals are more likely to persist in crystalline regions, potentially causing long-term effects like color centers or minor changes in mechanical properties.

When LCPs are exposed to high-energy electron beams, such as a 1 MeV beam, both unstable and trapped radicals form. Unstable radicals are generated immediately, breaking molecular bonds and causing chain scission in more amorphous regions. Meanwhile, stable trapped radicals form in the crystalline regions, persisting and causing long-term effects like color changes or small structural shifts without significantly altering mechanical properties.

Annealable color centers, typically linked to free radicals such as cyclohexadienyl and benzyl radicals (Wallace et al., 1993), can be removed through thermal annealing. Heat increases molecular motion, allowing trapped electrons to escape, effectively reversing the discoloration. This process is significantly slower in vacuum conditions but accelerates with increasing temperature, taking months at room temperature but only days at elevated temperatures, such as 80°C. Permanent color centers, on the other hand, cannot be removed by heat and persist within the polymer matrix, contributing to lasting discoloration.

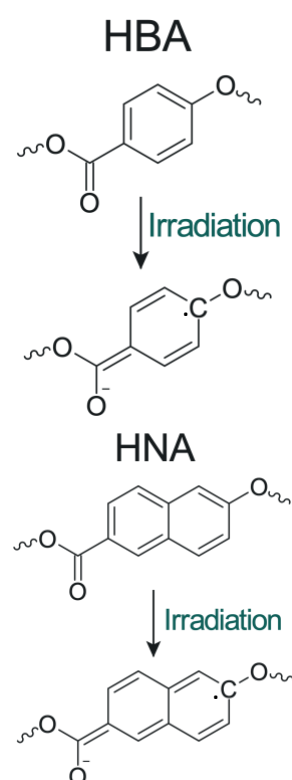


Figure 9: Schematic of HBA and HNA Monomers with Radicals. Illustrating potential quinone-type free radicals induced by irradiation in Hydroxybenzoic Acid (HBA) and Hydroxynaphthoic Acid (HNA) monomers.

Another class of radiation-induced radicals, quinone-type radicals, forms when aromatic structures in polymers undergo oxidation or modification due to radiation (Hou et al., 2019). These radicals, derived from quinones ($C_6H_4(CO)_2$), are highly reactive and often contribute to yellow or green discoloration in irradiated materials. The unpaired electrons in the quinone structure not only affect the material's color but may also influence its mechanical properties by creating or modifying chemical bonds. Figure 9 presents a schematic of HBA and HNA monomers, illustrating quinone-type free radicals.

To identify the types of radicals that form when LCP is irradiated with an electron beam, Electron Paramagnetic Resonance (EPR) spectroscopy could be used in future studies to detect and analyze the presence of specific radicals (Hou et al., 2019). EPR is particularly useful for studying materials with unpaired electrons, such as free radicals, by detecting changes in electron spins in a magnetic field, providing valuable insights into the identity of radicals, their electronic structure, and their interactions with neighboring atoms.

Interestingly, research by Clough et al. (1996) has shown that the extent of radiation-induced discoloration in polymers does not necessarily correlate with mechanical property changes or whether the polymer is aromatic or aliphatic in nature. This highlights the complexity of radiation's effects on polymers, where visible changes in color may not always reflect underlying mechanical alterations.

5.2 Annealing of Color Centers in Irradiated LCP

A pristine sample and a high fluence sample were annealed for one hour at 200°C in a vacuum oven 20 days after irradiation. The high fluence sample's color reverted to a slightly darker yellow tint, resembling a tanned appearance, compared to the pristine sample, which underwent the same annealing cycle, as shown in Figure 10A. This suggests that the color centers in the high fluence sample are annealable, supporting the idea that thermal treatment can reverse radiation-induced color changes.

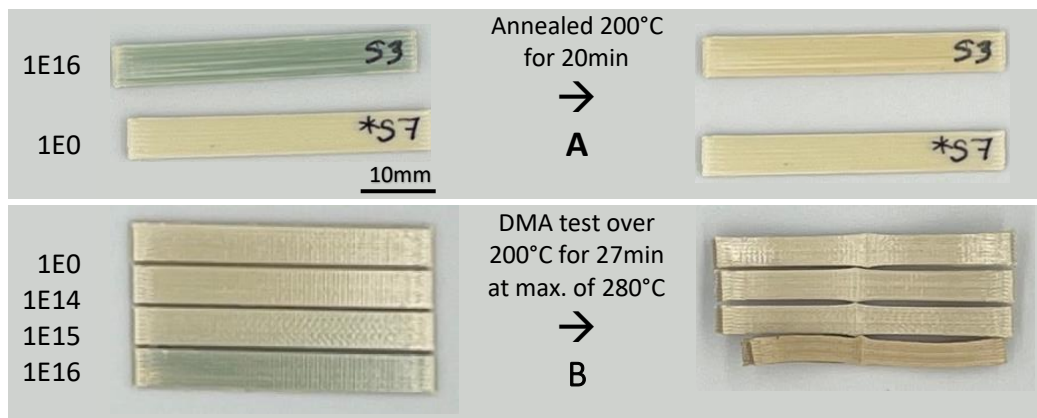


Figure 10: Annealing of Color Center in LCP Exposed to Electron Beam Irradiation. A. Pristine and high-fluence samples annealed at 200°C for 20 min 20 days after exposure; the green tint in high-fluence samples faded to a darker yellow. B. DMA-tested samples heated to 280°C, above 200°C for over 27 min, 156 days after exposure; high-fluence samples showing severe shrinkage and dark discoloration.

During DMA testing 156 days after irradiation with a temperature range of 25°C to 280°C, the high fluence samples exhibited significantly more shrinkage than the unirradiated, low, and mid fluence samples, as visible in Figure 10B. Additionally, a pronounced darker tan discoloration was observed in the high fluence samples post-DMA, indicating permanent radiation-induced color change. A study by Hou et al. (2019) identified two types of electron

radiation-induced color centers in translucent epoxy: one permanent, causing a dark yellow tint, and another annealable, producing a green hue. The researchers noted that irradiated samples gradually turned yellow over time, with higher fluence resulting in more pronounced yellowing after several months of ambient storage.

The discoloration of the high fluence samples after heating near their melting temperature suggests several potential causes, including permanent radiation-induced color centers or structural changes such as crosslinking or chain scission. Another possibility is that the higher fluence generated more radicals than the low and mid fluence samples, aligning with the more pronounced green hue and the only partial fading of the discoloration in high fluence samples, compared to the complete fading in the lower fluence samples. The subsequent annealing may have eradicated this high content of radicals, leading to significant crosslinking or chain scission, both of which can alter the polymer's optical properties. The pronounced effects were noticeable only when the polymer was heated near its melting point, indicating that thermal stress may amplify or reveal the impact of high radiation doses.

5.3 VR Microscopy on Cross-Section of Irradiated LCP

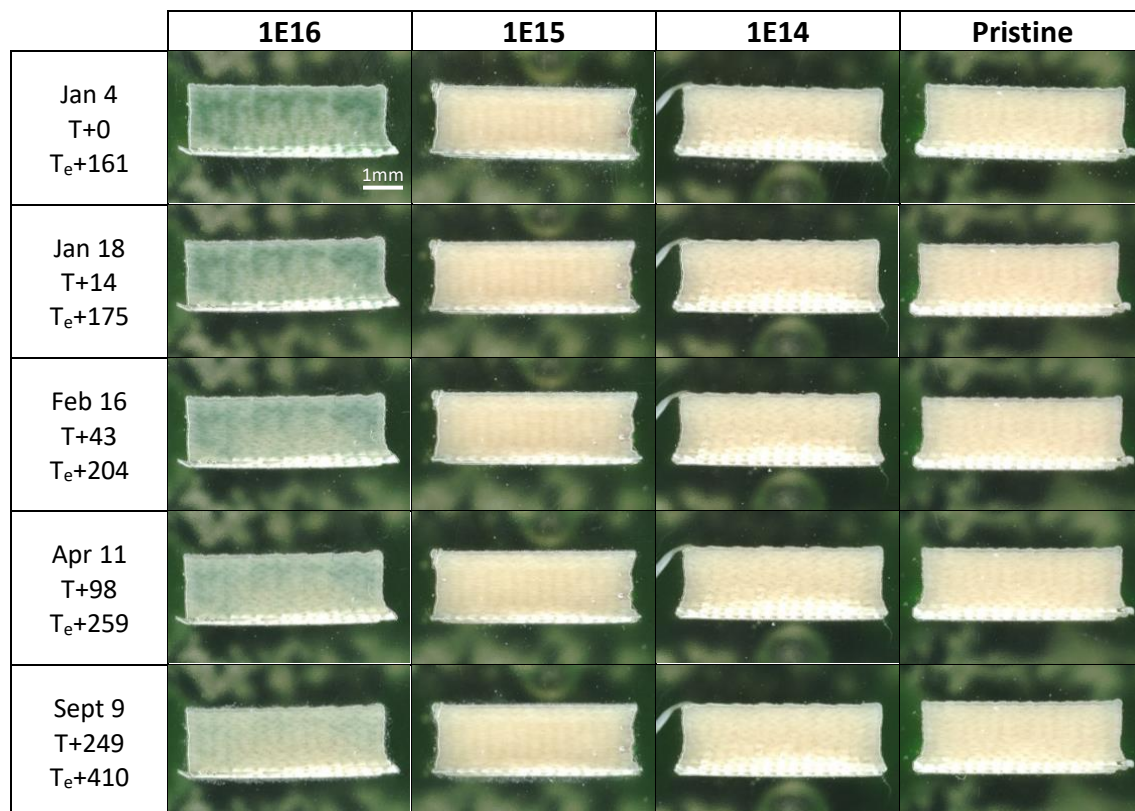


Figure 11: Cross-Section of LCP After Electron Beam Irradiation. The cross-section at the middle of the sample was exposed 5 months (161 days) after irradiation. The high fluence (1E16) sample retained a more intense green color in the core than on the surface, though less so than immediately after irradiation, while the low (1E14) and mid (1E15) fluence samples had fully returned to their original color. Color changes were tracked with a VR microscope over 8 months (249 days), revealing a gradual fading of the green hue in the core. The upper and outer sides of the samples exhibit a more intense green color than the bottom middle of the cross-section.

Following the fracture of a high fluence LCP sample during tensile testing, which exposed the green core (visible in Figure 14 in the next chapter), a resin coin was prepared to examine the cross-section. While the surface color had faded to a dim green, the core retained a darker, more noticeable green hue even 110 days after irradiation. The cross-sections of the UD0

samples, including all three fluences and a pristine sample, were exposed five months (161 days) post-irradiation and embedded in resin.

No visible color centers were observed in the cores of the low- and mid-fluence samples, consistent with the complete disappearance of color on their surfaces. In contrast, the high fluence sample still exhibited color centers, with the core remaining noticeably darker than the surface. Color changes were monitored with a VR microscope over eight months (249 days), revealing a gradual fading of the green hue in the core, as shown in Figure 11. Additional tracking dates, not included in Figure 11, are detailed in Appendix C. The presence of color centers throughout the core of the samples confirms full electron penetration of the polymer, potentially altering the polymeric network and impacting the material's mechanical properties, as discussed in the subsequent chapters.

The upper and outer sides of the samples display a more intense green color than the bottom middle of the cross-section, suggesting that the electrons did not uniformly penetrate the entire thickness of the sample. This is despite the deliberate use of high-energy electrons, intended to penetrate the full 2 mm thickness. The choice was based on the penetration depth of 1 MeV electrons from the Van de Graaff accelerator in water shown in Figure 12, which reaches a maximum dose at 1.5 mm depth, 147% of the surface dose, and returns to 100% at 2.5 mm, decreasing almost linearly to 20% at 3.25 mm, shown in **Error! Reference source not found.** If the color center intensity correlates with penetration depth, it appears that, for the LCP samples, the maximum electron penetration remained within the upper half, at less than 0.8 mm from the surface. However, since the entire cross-section showed green coloration, it confirms that the samples were fully penetrated by the electrons.

Using a derivation of the Bethe-Bloch theory, penetration depth can be correlated with material density, allowing for an approximation of both the electron beam's penetration depth and the dose it delivers (Tan et al., 2004; Tanabashi et al., 2018), shown in Equation 2.

$$\text{Penetration Depth } (R) \propto \frac{\text{Electron energy } (E)}{\text{Material density } (\rho)} \quad \text{Eq. (2)}$$

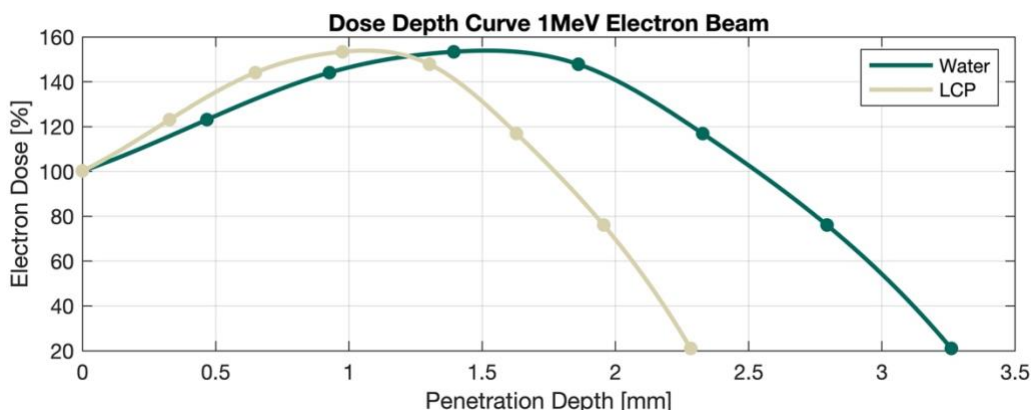


Figure 12: Electron Beam Radiation Dose Penetration Depth. Penetration depth of a 1 MeV electron beam measured in water ($\rho = 0.98 \text{ g/cm}^3$), converted based on the density of additively manufactured LCP Vectra A950 ($\rho = 1.4 \text{ g/cm}^3$).

Using the density of LCP Vectra A950, approximately 1.4 g/cm^3 (Jaffe et al., 2018; Romo-Uribe et al., 2022), and that of water, approximately 0.98 g/cm^3 , the penetration depth of 1 MeV electron beam in LCP was calculated, shown in Figure 12. From this, we can conclude that the LCP samples were penetrated to at least 70% of the surface dose throughout their entire depth, with full surface dose penetration up to approximately 1.786 mm, while the remaining

0.214 mm received a reduced dose. This uneven dose distribution is evident in the color intensity gradient seen in the cross-section. However, the area with the most intense coloration in the upper part of the sample does not precisely align with the maximum dose, which occurs near the center at approximately 1.071 mm. Although it is evident that the samples were not uniformly penetrated, it remains unclear whether this uneven dose distribution significantly affects the extent of radiation impact across various regions of the polymer.

5.4 UV-Vis-NIR Reflectance Spectra of Irradiated LCP Exposed to TVAC

When comparing UV-Vis-NIR reflectance spectra for pristine and irradiated samples before and after TVAC exposure, a noticeable change occurs around ± 600 nm, differentiating unirradiated from irradiated samples. This wavelength corresponds to the teal-green color observed after irradiation, likely caused by color centers formed due to free radicals. The spectra also show a discrepancy around 1400 nm, where the irradiated samples have lower reflectance from approximately 1400 nm to 1500 nm compared to unirradiated ones, both before and after TVAC exposure. However, TVAC appears to reduce this discrepancy, potentially due to the temperature increase or time-related self-quenching of the material, as oxygen quenching is unlikely in a vacuum environment. Hou et al. (2019) identified additional peaks around 350-450 nm, which were associated with permanent yellow discoloration in irradiated epoxy. However, unlike the translucent epoxy samples in that study, LCP Vectra inherently has a beige-yellow color, making it difficult to detect new permanent color centers through reflectance spectra. The wavelengths in this region are likely to correspond with Vectra's original color, rather than clearly indicating the formation of radiation-induced yellow permanent color centers.

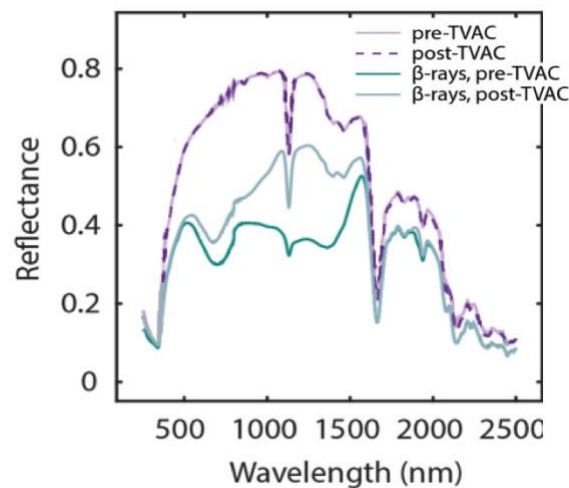


Figure 13: Reflectance Spectrum Comparison of Irradiated LCP Exposed to TVAC. Reflectance spectra of pristine and high-fluence irradiated 3D-printed LCP samples before and after 25 thermal cycles in vacuum (-100°C to $+100^{\circ}\text{C}$, $5^{\circ}\text{C}/\text{min}$), showing an inverse peak around 600 nm in irradiated samples.

6 Impact of Space Environment and FFF on Tensile Properties of LCP

This chapter examines the impact of electron beam exposure at three different intensities and 25 cycles of thermal vacuum cycling, spanning temperatures from -100°C to +100°C with a heating rate of 5°C/min, on the static mechanical properties of Liquid Crystal Polymers (LCP). The primary focus is on assessing the tensile properties of LCP samples by measuring Young's modulus (E) and ultimate tensile strength (UTS). The chapter first addresses the tensile properties of LCP samples exposed to radiation and TVAC, which were printed at 295°C. Following this, the chapter will explore LCP samples printed at four different temperatures, comparing those that were left unexposed to those subjected to thermal vacuum cycling only.

Tensile testing can be used to determine if crosslinking or chain scission occurred after radiation or TVAC exposure. Crosslinking typically increases tensile strength and stiffness but reduces ductility. Chain scission leads to reduced tensile strength, stiffness, and overall mechanical performance. High radiation doses may initially increase tensile strength due to cross-linking but can later decrease it as excessive cross-linking leads to brittleness (Plis et al., 2019).

6.1 Influence of Electron Beam and TVAC on Tensile Properties

No significant differences in Young's modulus (E) and ultimate tensile strength (UTS) were observed for samples exposed to increasing fluence, as shown in Figure 14A. The varying intensity of coloration with fluence did not correlate with changes in E or UTS. Similarly, exposure to the highest fluence and subsequent thermal vacuum cycling (TVAC) did not significantly alter static mechanical properties.

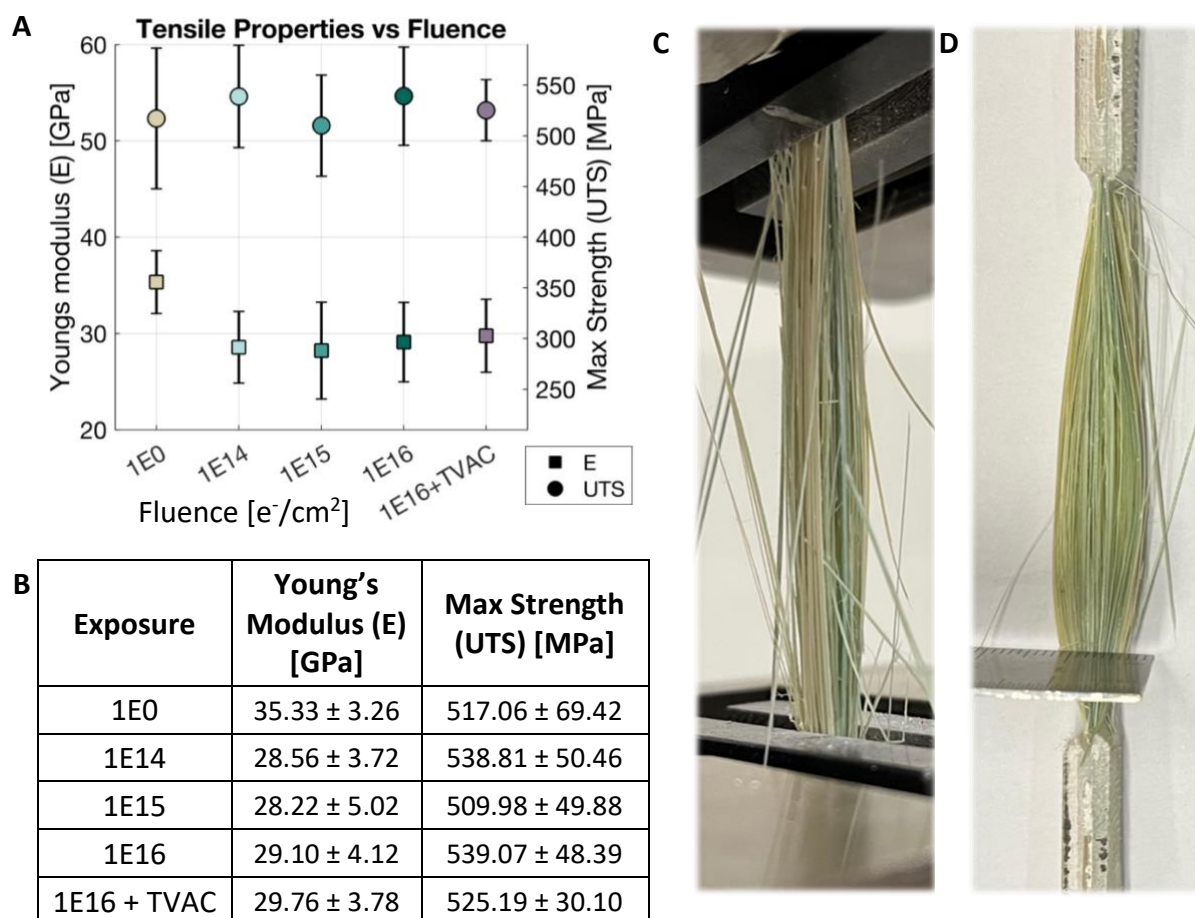


Figure 14: Impact of Exposure to Electron Beam on Tensile Properties of LCP. No significant difference in Young's modulus and UTS after exposure with increasing fluence and 25 cycles of thermal cycling under vacuum with a temperature range of -100°C to +100°C and a heating rate of 5°C/min. **A.** Bar plot of tensile test with measured Young's modulus and UTS for all three fluences, with error bars representing standard deviation. **B.** Table showing the numerical values corresponding to the bar plot for comparison. **C.** Fracture of a tensile sample from the highest fluence (1E16) while still clamped and **D.** the same sample on a desk under applied force, revealing intense coloration in the core.

The pristine samples, printed at 295°C in a different batch, show a slightly higher Young's modulus and slightly lower UTS compared to the irradiated samples, except for mid fluence. These differences are minor and likely due to batch variations, despite consistent printing parameters. For a detailed comparison, numerical data can be found in the table accompanying the bar plot in Figure 14B.

Figure 14C depicts typical catastrophic failure in UDO composite samples with strong anisotropy, the extruded fibers tend to pop out rather than break, indicating layer adhesion fails first. Figure 14D, with applied pressure to improve visibility, reveals that the core of high fluence samples exhibit a more intense green color due to electron radiation penetration. In contrast, the surface color intensity has significantly faded, but a green hue persists in the core even after 110 days post-exposure.

In summary, no significant changes in Young's modulus or UTS were observed with increasing radiation fluence, nor with the highest fluence and subsequent thermal vacuum cycling. There is no evidence to suggest that radiation or TVAC exposure induced crosslinking or chain scission. Minor differences in mechanical properties between pristine and exposed samples are likely due to batch variations.

6.2 Influence of TVAC and Printing Temperatures on Tensile Properties

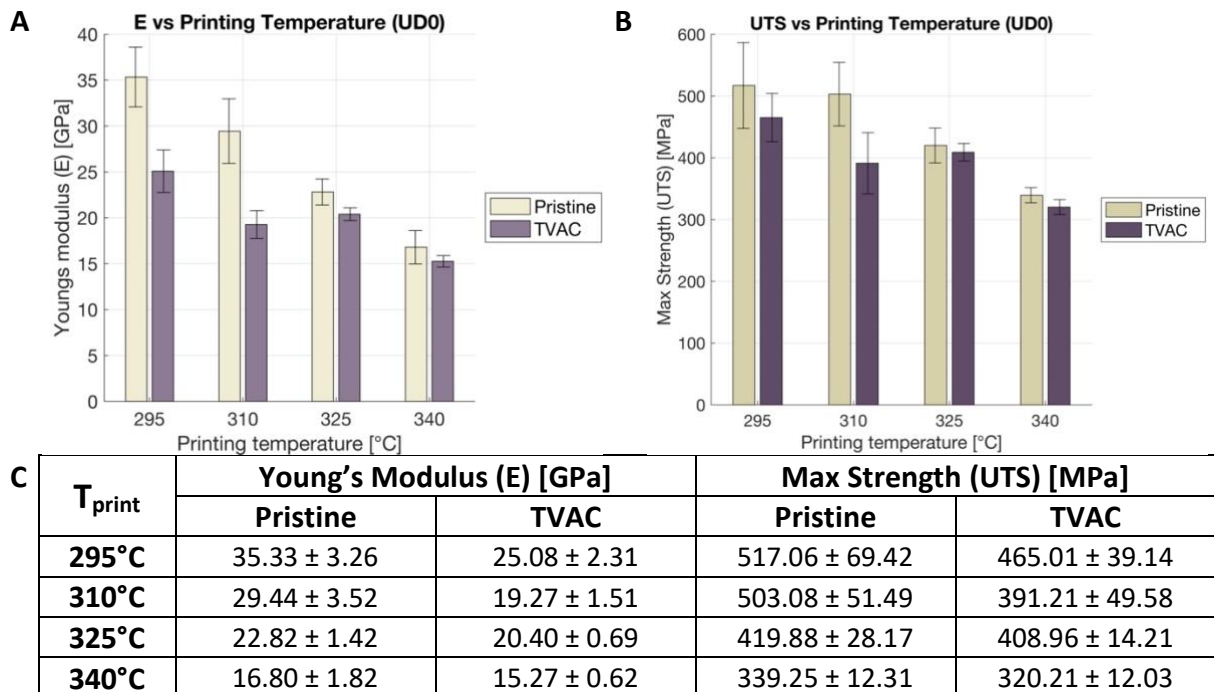


Figure 15: Impact of Exposure to TVAC and Printing Temperature on Tensile Properties of LCP for UDO. For UDO samples loaded along the printing direction, higher printing temperatures result in lower Young's modulus and UTS. Exposure to 25 cycles of thermal cycling under vacuum with a temperature range of -100°C to +100°C and a heating rate of 5°C/min shows a more pronounced decrease in tensile properties for samples printed at lower printing temperatures (295°C and 310°C) compared to higher printing temperatures (325°C and 340°C). Bar plot of tensile test with measured Young's modulus (**A**)

and UTS (B) for different printing temperatures, with and without exposure to TVAC, with error bars representing standard deviation. C. Table containing the numerical values of the bar plot.

Printing temperature significantly affects both Young's modulus and ultimate tensile strength (UTS) for UD0 samples loaded along the printing direction. These results align with the findings of Gantenbein et al. (2021), as discussed in the literature review of this thesis. Higher printing temperatures extend the time required to reach the solidification point, allowing nematic domains more time to relax into a less ordered state. This increased disorder in the molecular structure results in reduced mechanical properties along the printing direction. UD0 samples loaded in the printing direction exposed to TVAC exhibit similar trends, though the effect is less pronounced. Young's modulus is more sensitive to changes in printing temperature than UTS. Additionally, Young's modulus is also more significantly affected by TVAC exposure compared to UTS.

Figure 15A shows that for UD0 samples, exposure to TVAC notably reduces Young's modulus, especially at lower printing temperatures of 295°C and 310°C, with a reduction of ± 10 GPa. Higher printing temperatures of 325°C and 340°C also show a decrease, but it is less statistically significant, ± 2 GPa. Figure 15B shows that UTS is only slightly affected by TVAC, with a significant decrease observed only at a printing temperature of 310°C. For higher printing temperatures, the decrease in UTS is negligible. The table in Figure 15C gives the numerical values of the bar plot for a more detailed comparison.

For UD90 dogbone-shaped samples loaded perpendicular to the printing direction, shown in Figure 16A, increasing the printing temperature from 295°C to 325°C had little effect on Young's modulus. A slight decrease was only observed at the highest temperature of 340°C, indicating that the material's stiffness remains relatively stable across the tested temperature range, with minor degradation at the upper limit. In contrast, Figure 16B shows that UTS displayed a positive correlation with increasing printing temperature, suggesting that higher temperatures improve the material's load-bearing capacity, likely due to enhanced interlayer bonding during printing (Gantenbein et al., 2021).

After exposure to TVAC, most samples showed a slight decrease in both Young's modulus and UTS, visible in Figure 16, indicating minor mechanical degradation from repeated thermal stress, potentially due to microstructural changes within the polymer matrix, such as crosslinking or chain scission. Notably, samples printed at 340°C showed an increase in both tensile properties after thermal cycling. This may suggest that higher printing temperatures lead to a more resilient molecular structure, better withstanding thermal cycling or benefiting from enhanced layer fusion or crosslinking. The table in Figure 16C gives the numerical values of the bar plot for a more detailed comparison.

For both UD0 and UD90 samples, the weak point is layer adhesion. As shown by the failure mode for UD0 samples in Figure 14C, the extruded fibers tend to pop out rather than break. This suggests that the bonding between layers is the limiting factor in these samples, rather than the strength of the extruded fibers themselves. UD90 samples rely heavily on layer adhesion for both Young's modulus and UTS. Loaded perpendicular to the print layers, their performance depends on interlayer bond strength, leading to failure under much lower loads compared to UD0 samples, where extruded fibers bear more of the load.

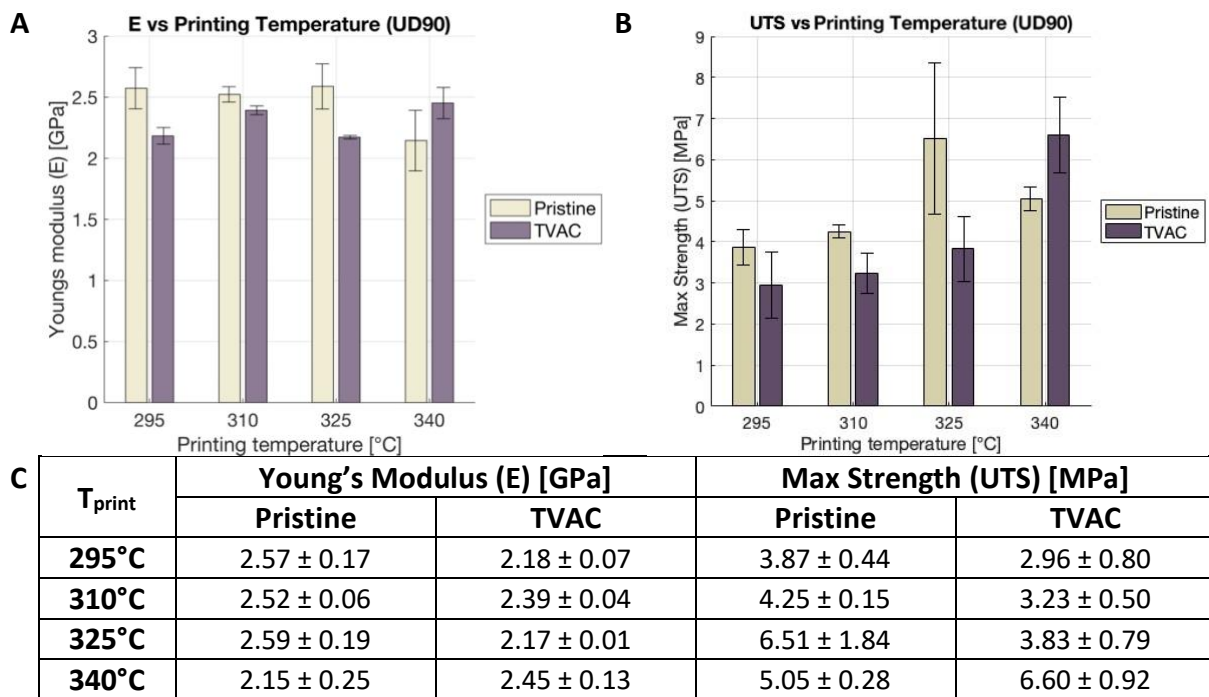


Figure 16: Impact of Exposure to TVAC and Printing Temperature on Tensile Properties of LCP for UD90. For UD90 samples loaded perpendicular to the printing direction, increasing the printing temperature has minimal impact on Young's modulus, with only a slight decrease observed at 340°C. However, Ultimate Tensile Strength (UTS) improves with higher printing temperatures. After 25 cycles of thermal cycling in vacuum, ranging from -100°C to +100°C with a heating rate of 5°C/min, both Young's modulus and UTS show a slight decrease for most printing temperatures, except for 340°C, where an increase in tensile properties is noted. Bar plot of tensile test with measured Young's modulus (A) and UTS (B) for different printing temperatures, with and without exposure to TVAC, with error bars representing standard deviation. C. Table containing the numerical values of the bar plot.

It should be noted that the pristine samples and those exposed to thermal vacuum cycling (TVAC) were not printed simultaneously, which could introduce variations due to differences in manufacturing. Therefore, any observed differences between these samples should be considered in this context. While exposure to TVAC influences both Young's modulus and UTS to some extent, further study is needed to accurately assess these effects. Future research should ensure that samples are printed simultaneously under identical conditions, using a larger batch, and randomly distributed between pristine and exposed samples to minimize the influence of manufacturing variability on tensile properties.

In summary, printing temperature significantly affects the mechanical properties of UD0 samples loaded in printing direction, with higher temperatures leading to reduced Young's modulus and UTS due to increased molecular disorder. In contrast, for UD90 samples, printing temperature had little effect on Young's modulus but improved UTS, likely due to enhanced interlayer adhesion. TVAC exposure further reduced Young's modulus for UD0 samples, especially at lower printing temperatures, while UTS remained mostly unaffected, particularly at higher temperatures. For UD90 samples, both Young's modulus and UTS slightly decreased after TVAC exposure, except at 340°C, where both properties improved. The observed changes in tensile properties were not pronounced enough to definitively determine whether crosslinking or chain scission occurred. Variability due to non-simultaneous printing may have influenced the comparison between pristine and TVAC-exposed samples.

7 Impact of Space Environment on Dynamic Mechanical Properties of LCP

This chapter investigates the effects of electron beam exposure at three different intensities, 25 cycles of TVAC ranging from -100°C to +100°C with a heating rate of 5°C/min, and annealing of electron beam radiation-induced color centers in a vacuum oven at 200°C for 20 minutes on the dynamic mechanical properties of LCP. The focus is on evaluating the dynamic mechanical properties of LCP samples by measuring the storage modulus (E') and loss modulus (E'') to determine the damping factor, $\tan \delta = E''/E'$. Additionally, thermal resistance is assessed through molecular relaxations to obtain the glass transition temperature. The analysis involves a temperature sweep from 22°C to 200°C at a constant frequency of 10 Hz and a strain of 0.1%. Although the loss modulus is included in the figures, a dedicated plot for detailed examination is available in Appendix D, where the corresponding DMA numerical data is also provided, including a comparison of all experiments.

By comparing glass transition temperatures (T_g) and E' , it is possible to determine whether crosslinking or chain scission occurred after irradiation. Crosslinking typically raises T_g by restricting the mobility of polymer chains and increases E' , as the material becomes stiffer and more elastic. In contrast, chain scission lowers T_g , E' , and E'' , as the shorter polymer chains move more freely, and their reduced molecular weight weakens the polymer structure. An increase in $\tan \delta$ implies a rise in the loss modulus (E'') rather than the storage modulus. This suggests that electron radiation made the material more viscous, supporting the hypothesis of (increased) chain crosslinking hypothesis (Plis et al., 2019).

7.1 Influence of Electron Beam on Dynamic Mechanical Properties

Pristine samples and those exposed to low fluence exhibit similar storage and loss moduli, while samples exposed to mid and high fluence show a decrease, as shown in Figure 17A, with the reduction more pronounced in storage modulus. This trend is reflected in the damping factor, $\tan \delta$, which increases with higher radiation doses. This suggests that the material has undergone modifications or degradation, possibly due to physical or chemical changes such as chain scission.

Figure 17B shows the $\tan \delta$ amplitudes of the β -peak and α -peak, along with the temperatures at which they occur. The first relaxation, associated with the motion of the HNA moiety and referred to as the β -peak, exhibits an increase in amplitude and a slight rise in temperature with higher exposure doses. The average temperature of the β -peak is 54.9°C across all samples, with unirradiated samples averaging 48.4°C and irradiated samples averaging 57.1°C. In contrast, no significant changes in temperature were observed for the second relaxation, the α -peak, which is related to the glass transition temperature and the simultaneous motion of HNA and HBA moieties. The average glass transition temperature remains around 101.9°C for all samples, regardless of exposure intensity. However, the amplitude of the α -peak increases with increasing fluence, which correlates with the decrease in storage modulus observed with higher fluence.

Literature on dynamic mechanical measurements of extruded LCP reported that the $\tan \delta$ amplitude of the β -peak was higher than that of the α -peak for both pristine and annealed samples, even after up to five hours of annealing. However, after five hours of annealing, this trend reversed, with the α -peak amplitude surpassing that of the β -peak (Romo-Urbe et al., 2022). In contrast, 3D-printed samples do not exhibit this behavior, either before or after exposure. Pristine printed samples display comparable $\tan \delta$ amplitudes for both peaks, while

irradiated samples display a lower $\tan \delta$ amplitude for the β -peak compared to the α -peak. This discrepancy may be attributed to the FFF processing, which involves thermal treatment twice, once during filament production and once during printing. Figure 17C illustrates that with increasing exposure doses, the $\tan \delta$ amplitude of the α -peak rises relative to the β -peak, while the temperature difference between the peaks diminishes. Consequently, the β -peak shifts closer to the α -peak.

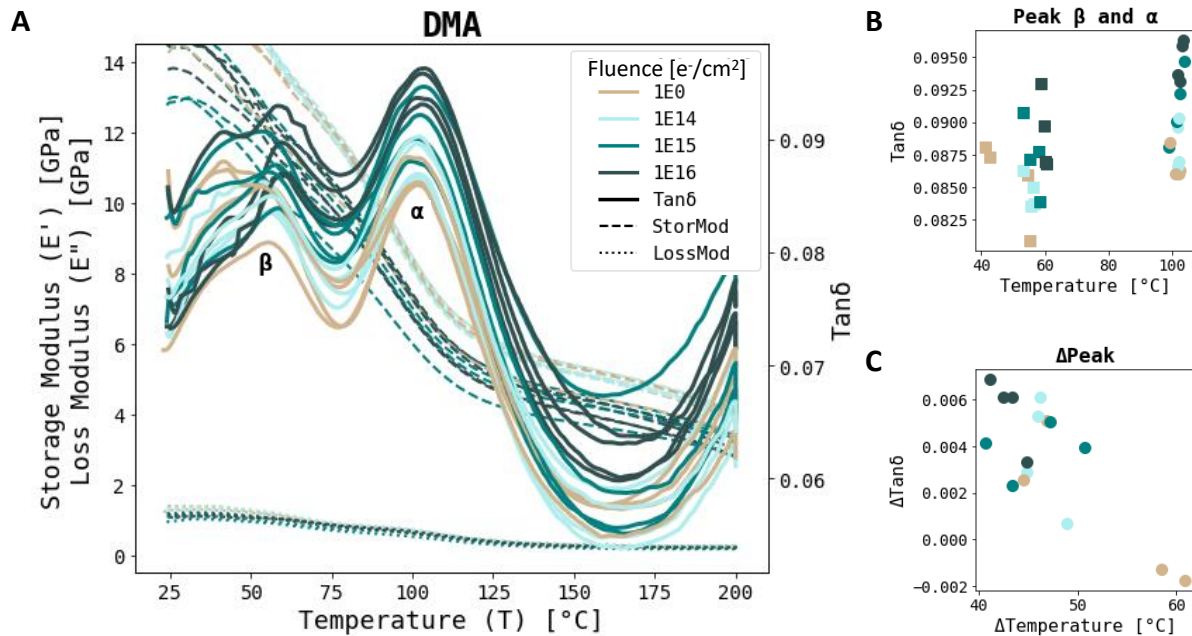


Figure 17: Impact of Exposure to Electron Beam of LCP on Storage Modulus E' , Loss Modulus E'' and Damping Factor $\tan \delta$ as a Function of Temperature. Three-point bending dynamic mechanical analysis was performed at a frequency of 10 Hz and 0.1% strain on samples subjected to all three fluences, as well as on unirradiated samples. A slight increase in the damping factor and a decrease in the storage modulus were observed with increasing fluence. **A.** The first peak, termed β , corresponds to the relaxation of the HNA moiety. The second peak, termed α , is attributed to the simultaneous motion of both HNA and HBA moieties, akin to the glass transition temperature. The α -peaks exhibit a noticeably larger $\tan \delta$ amplitude compared to the β -peak for exposed samples. **B.** The β -peak occurs on average around 48°C for unirradiated samples and around $57 \pm 2^{\circ}\text{C}$ for the irradiated samples, it shifts to slightly higher temperatures with increasing fluence. The $\tan \delta$ of the β -peak increases with increasing fluence. The α -peak occurs at $102 \pm 3^{\circ}\text{C}$, with $\tan \delta$ also increasing with increasing fluence. **C.** The difference between the β - and α -peaks in $\tan \delta$ amplitude and temperature, which increases and decreases with increasing fluence, respectively.

In summary, exposure to electron beam radiation induces a modest but noticeable change with increasing fluence, suggesting chain scission occurred. This includes a decrease in E' and E'' , an increase in the damping factor $\tan \delta$, and a shift in the motion of the HNA moiety, while the glass transition temperature remains unchanged.

7.2 Influence of Electron Beam and TVAC on Dynamic Mechanical Properties

The unirradiated samples exposed solely to TVAC exhibit lower storage (E') and loss modulus (E'') compared to those subjected to both TVAC and radiation, as shown in Figure 18. The combined increase in E' and E'' for irradiated samples suggests that more crosslinking occurred when electron radiation and TVAC were combined. Additionally, these unirradiated samples display a higher $\tan \delta$ amplitude for the β -peak compared to the α -peak, a trend that is also consistent for samples exposed to low and mid fluence. This observation contrasts with findings in the literature for extruded LCP tapes, where the β -peak amplitude was larger only after a minimum of five hours of annealing (Romo-Urbe et al., 2022). The discrepancy may stem from differences between extrusion and FFF methods, though TVAC exposure might

align the nematic domains of the printed samples more alike those of extruded samples. For high fluence samples, the α -peak amplitude remains greater than that of the β -peak, resulting in the largest positive difference in $\tan \delta$ amplitude after TVAC, as depicted in Figure 18C. This pattern is similar to that observed in solely irradiated samples discussed earlier.

An increase in the glass transition temperature is noted to an average of 106.6°C, with minimal variation across different exposure intensities, as shown in Figure 18B. This represents a nearly 5°C increase after TVAC compared to solely irradiated samples, suggesting crosslinking occurred. In contrast, the β -peak relaxation temperature slightly decreases after TVAC exposure, averaging 50.8°C, with minimal fluctuation among different exposure intensities.

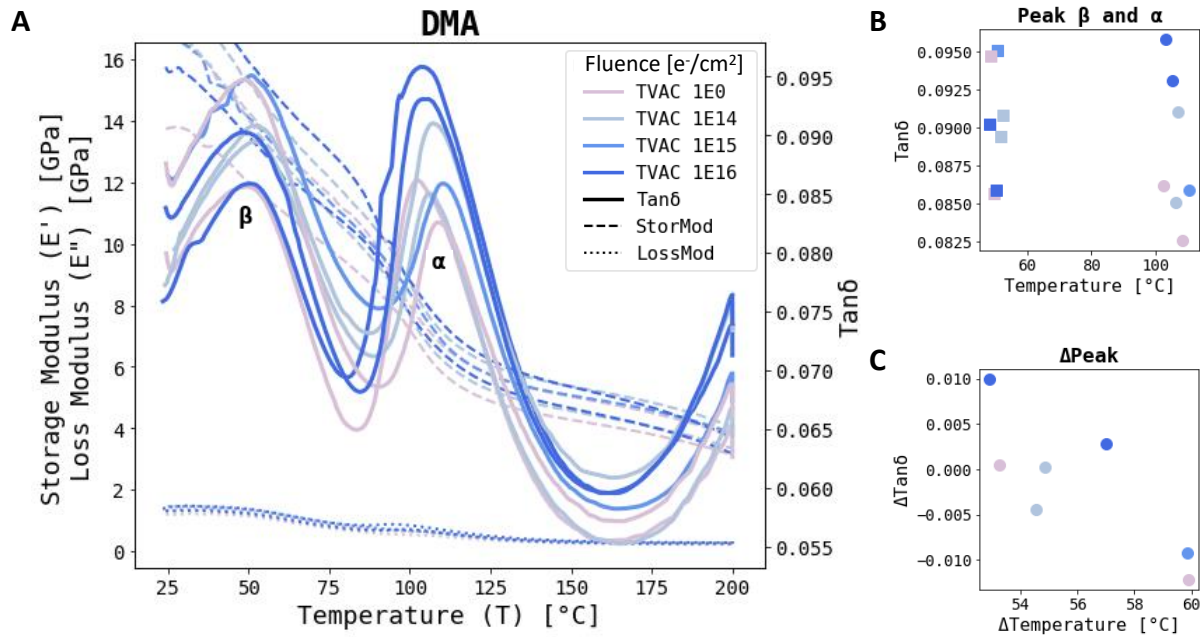


Figure 18: Impact of Exposure to Electron Beam and TVAC of LCP on Storage Modulus E' , Loss Modulus E'' and Damping Factor $\tan \delta$ as a Function of Temperature. Three-point bending dynamic mechanical analysis was performed at a frequency of 10 Hz and 0.1% strain on samples subjected to all three fluences, as well as on unirradiated samples, followed by 25 cycles of thermal cycling under vacuum with a temperature range of $-100^{\circ}C$ to $+100^{\circ}C$ and a heating rate of $5^{\circ}C/min$. **A.** The first peak, termed β , corresponds to the relaxation of the HNA moiety. The second peak, termed α , is attributed to the simultaneous motion of both HNA and HBA moieties, akin to the glass transition temperature. **B.** The β -peak occurs at $51 \pm 2^{\circ}C$ after TVAC for all exposure intensities. Exposure to TVAC has increased the glass transition temperature of LCP, the α -peak occurs around $107 \pm 3^{\circ}C$, with $\tan \delta$ increasing with increasing fluence. **C.** After TVAC, unirradiated samples and those exposed to low and mid fluence show a larger $\tan \delta$ amplitude for the α -peak compared to the β -peak.

In summary, the β -peak amplitude exceeds the α -peak for all samples exposed to TVAC, except at high fluence. Additionally, the glass transition temperature increases by nearly 5°C after TVAC, possibly indicating crosslinking, while the β -peak relaxation temperature decreases slightly, with minimal variation across exposure intensities. TVAC likely induced crosslinking, particularly in irradiated samples, as evidenced by the increased E' and E'' . However, it is important to exercise caution regarding the repeatability of this DMA data. Only two samples were used per sample type, more samples should be tested in future studies to confirm the findings and reduce the influence of sample variability.

7.3 Influence of Electron Beam and Annealing on Dynamic Mechanical Properties

Unirradiated and irradiated samples were subjected to step-annealing in a vacuum oven at $100^{\circ}C$ for 35 minutes followed by $200^{\circ}C$ for 20 minutes to remove color centers and evaluate

potential reversals in changes witnessed after exposure to electron beam radiation. This temperature was selected to avoid influencing crystallinity or causing crosslinking, as it is well below the glass transition temperature.

After annealing, the storage modulus remains higher for unirradiated and low fluence irradiated samples, while $\tan \delta$ continues to increase with higher exposure intensities, as shown in Figure 19A. Notably, all samples now exhibit a larger $\tan \delta$ amplitude for the β -peak compared to the α -peak, aligning with findings for annealed extruded LCP (Romo-Urbe et al., 2022). This change suggests that annealing had a significant impact beyond just removing color centers, despite the relatively low temperatures and brief duration chosen for this step-annealing.

Post-annealing, the average β -peak temperature decreased to 46.8°C , as depicted in Figure 19B, approaching values seen in pristine samples. The glass transition temperature averaged 101.9°C , showing minimal change compared to pre-annealing values and little variation among unirradiated, low, and mid-fluence samples. However, high fluence samples exhibited an increase in T_g to 106.0°C , suggesting that annealing enhanced crosslinking in those exposed to high fluence. Figure 19C shows no significant trends in $\tan \delta$ amplitude and temperature differences between DMA peaks for various fluences after annealing.

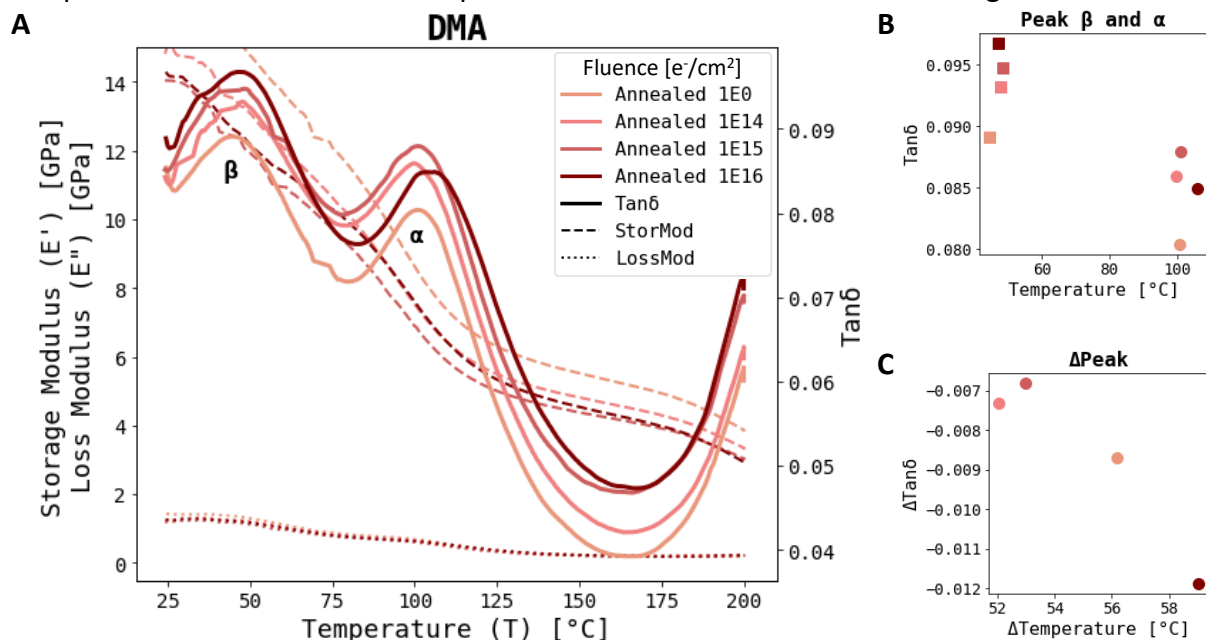


Figure 19: Impact of Exposure to Electron Beam and Annealing of LCP on Storage Modulus E' , Loss Modulus E'' and Damping Factor $\tan \delta$ as a Function of Temperature. Three-point bending dynamic mechanical analysis was performed at a frequency of 10 Hz and 0.1% strain on samples subjected to all three fluences, as well as on unirradiated samples, followed by step-annealing in vacuum for 35min at 100°C and subsequently 20min at 200°C . A slight increase in the damping factor and a decrease in the storage modulus were observed with increasing fluence. **A.** The first peak, termed β , corresponds to the relaxation of the HNA moiety. The second peak, termed α , is attributed to the simultaneous motion of both HNA and HBA moieties, akin to the glass transition temperature. **B.** The β -peak occurs at $47 \pm 2^\circ\text{C}$ after annealing for all exposure intensities. The $\tan \delta$ of the β -peak increases with increasing fluence. The α -peak occurs around $102 \pm 2^\circ\text{C}$, with $\tan \delta$ also increasing with increasing fluence, except for the highest fluence. **C.** After annealing, the difference between the β - and α -peaks in $\tan \delta$ amplitude and temperature shows that the $\tan \delta$ amplitude of the β -peak has grown larger compared to the α -peaks.

In summary, post-annealing, the storage modulus remains higher for unirradiated and low fluence samples, $\tan \delta$ increases with exposure intensity, and the β -peak temperature decreases while the glass transition temperature increased only for high fluence. Additionally, all samples show a larger β -peak $\tan \delta$ amplitude, suggesting that annealing had a notable impact beyond color center removal.

8 Impact of Space Environment and FFF on Thermal Properties of LCP

This chapter examines the impact of electron beam exposure at three different intensities and annealing of different stages of Fused Filament Fabrication in a vacuum oven at 240°C for up to five hours on the thermal properties of Liquid Crystal Polymers (LCP), as measured by Differential Scanning Calorimetry (DSC). The study analyzes melting and solidification temperatures (T_m and T_{mc}), melting and solidification peak temperatures (T_p and T_{pc}), and enthalpy of fusion (ΔH), as shown in Figures 9, 10, and 12. Glass transition temperature (T_g) and heat capacity (C_p) data for each cycle and sample are available in Appendix E. The DSC analysis consisted of five cycles, three heating and two cooling, from 25°C to 360°C at a constant heating rate of 10°C/min.

The difference between melting and solidification temperatures indicates the stability of the crystalline regions per sample, $\Delta T_m = T_m - T_{mc}$. A smaller difference implies more stable crystalline structures, while a larger difference suggests imperfect or less stable crystals. By comparing melting temperatures, crosslinking or chain scission can be identified. Crosslinking generally raises the melting temperature, while chain scission lowers it, as shorter polymer chains are less capable of forming stable crystals.

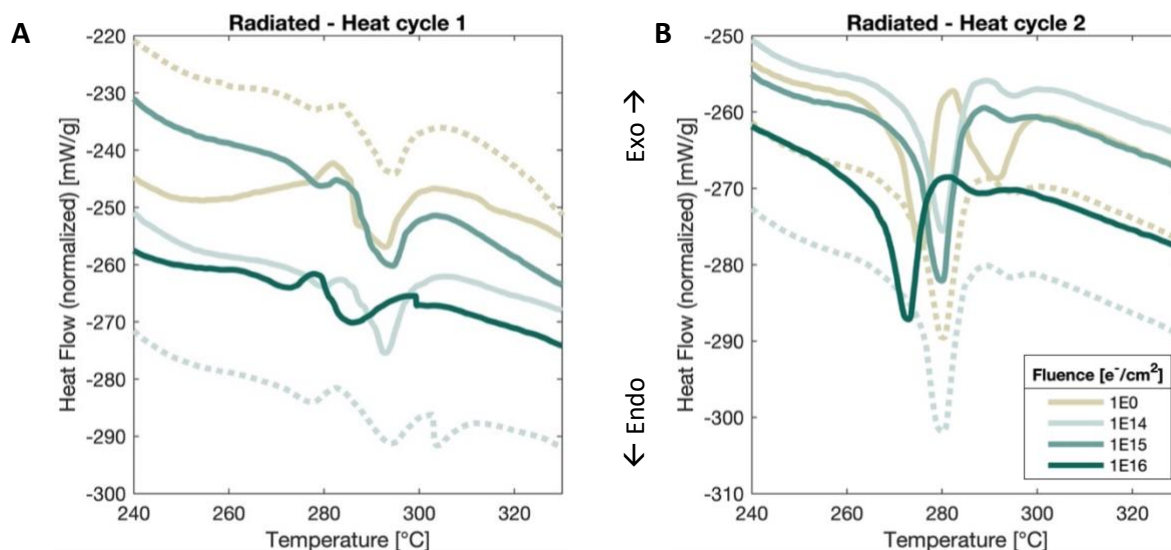


Figure 20: Heat flow as a function of temperature for irradiated LCP measured by DSC. Heat flow (ΔQ) traces of the endothermic peaks for the first heat cycle (A) and the second heat cycle (B) for irradiated samples are shown. The first heat cycle exhibits noisy data, complicating the accurate determination of melting (peak) temperatures. In contrast, the second heat cycle, along with the nearly identical third heat cycle (not shown), provides smoother data with well-defined melting regions. Solid and dotted lines differentiate between two runs with identical parameters.

In the first heating cycle, multiple overlapping endothermic and exothermic peaks complicate peak determination, likely due to imperfect thermal contact between the sample and the hermetic pan. However, from the second cycle onwards, consistent peaks emerge, suggesting the contact issues have been resolved. This variability, seen as noisy data, likely stems from imperfect contact between the sample and hermetic pan, especially in irradiated and printed samples punched from 3D-printed materials. The punching process can cause delamination, reducing thermal contact. Once the sample melts in later cycles, these issues are minimized. Literature suggests that LCP samples in direct contact with aluminum pans may shrink and curl during heating, affecting thermal data (Wiberg & Gedde, 1998). Immersion in silicone oil

or embedding with Kapton film is recommended to mitigate this issue, but no data quality issues were observed beyond the first cycle in this experiment.

8.1 Influence of Electron Beam on Thermal Properties of LCP

Glass transition temperature (T_g) typically resets to $95\pm 1^\circ\text{C}$ after the first melting cycle due to the erasure of thermo-mechanical history. T_g data for irradiated samples, however, showed incomplete resetting in the second cycle but approached 95°C by the third cycle. Due to the inherent unreliability of DSC T_g measurements for crystalline materials, this data will not be compared the effects of radiation in this study.

Figure 20 displays normalized heat flow traces for the first heating cycle in Figure 20A and the second heating cycle in Figure 20B. The first heating cycle exhibits noisy data, likely due to thermal contact issues, which complicates accurate determination of melting temperatures. In contrast, the second and third heating cycles, which show smooth data with sharp, well-defined peaks, allow for more precise measurements. Neither irradiated nor unirradiated samples exhibit multiple peaks in the first cycle, and this consistency is also observed for irradiated samples in the second and third cycles.

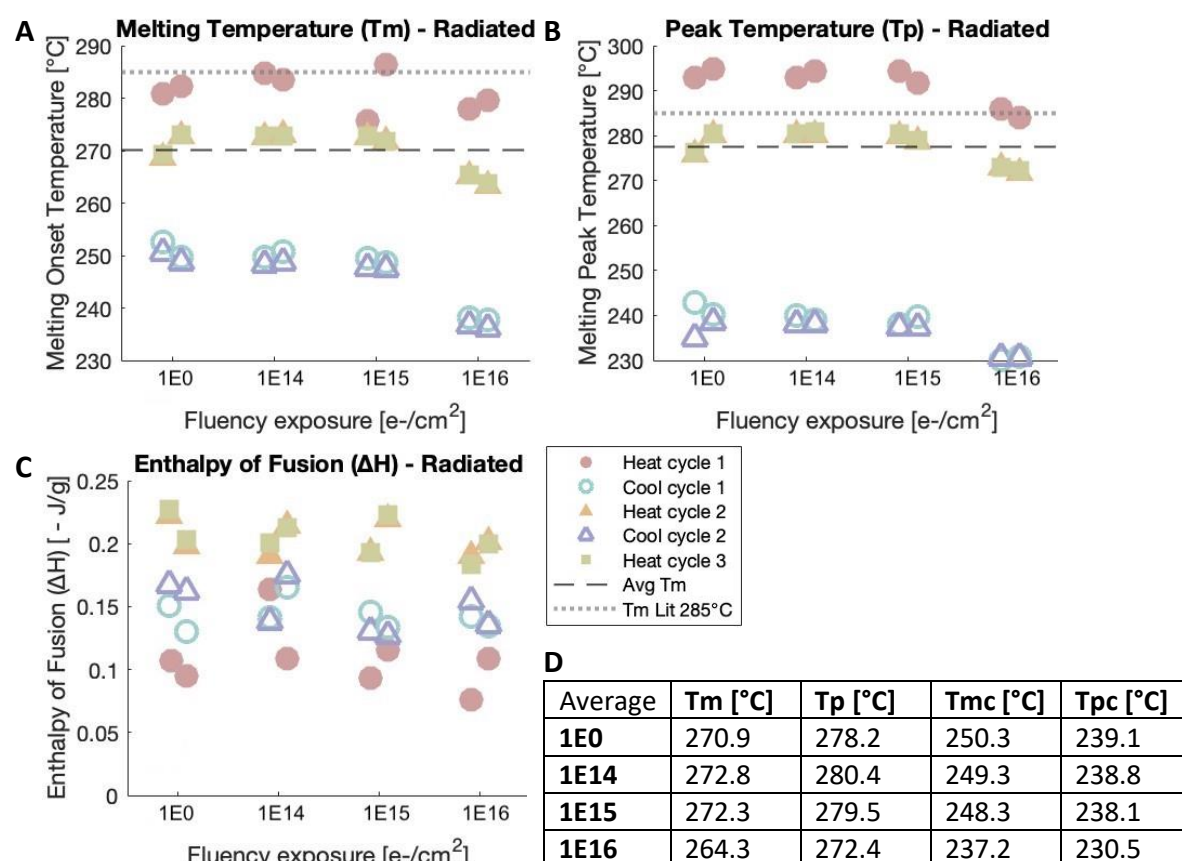


Figure 21: Melting Temperatures and Enthalpy of Fusion of Irradiated LCP Measured with DSC. Five cycles were run on DSC: three heating cycles and two cooling cycles, over a temperature range of 25°C to 360°C , with a constant heating rate of $10^\circ\text{C}/\text{min}$. LCP samples irradiated at the highest fluence show significantly lower melting temperatures across all cycles. Literature often reports a melting temperature reset to 285°C (...) for the second and third heat cycles of LCP. Unirradiated, low and mid fluence samples approach this value with their melting peak temperature. **A.** The average melting temperature of the second and third heat cycle is 270.1°C (---). **B.** The average melting peak temperature of the second and third heat cycle is 277.6°C (---). **C.** Enthalpy of fusion does not show a significant change per fluence. **D.** Table showing average temperatures, excluding data from the first heating cycle.

Figure 21A and B illustrate that there is minimal change in T_m and T_p for low and mid fluences of radiation compared to pristine samples, with both heat cycles returning to approximately 272.0°C and 279.4°C, respectively, rather than the 285°C reported by Romo-Urbe (2021) but consistent with the 279–281°C range reported by Johann et al. (2024). In contrast, samples exposed to high fluence exhibit lower T_m and T_p , reflecting a decrease of more than 7°C, suggesting chain scission. Chain scission reduces T_m and crystallinity by shortening polymer chains, indicating that electron beam radiation has a lasting, non-reversible effect on LCP.

Literature reports a solidification peak (T_{pc}) of 237.5°C, which all samples approached, except high fluence samples, which showed a 10°C offset, reaching 230°C. The difference between melting and solidification temperatures ΔT_m can be used to assess changes in crystallinity in a sample, but no significant change was observed for any of the samples.

No trends indicate a change in ΔH across fluences in Figure 21C. Heat capacity (C_p) data from the first heating cycle is unreliable due to poor thermal contact, but the second and third cycles show smoother, consistent results, indicating radiation had little impact on crystallinity. Notably, high-fluence samples showed a substantial increase in C_p during cooling cycles, though ΔH and peak shapes remained unchanged, suggesting no significant change in crystallinity.

In summary, after exposure to different fluence levels of electron beam radiation, there are minimal changes in melting temperatures (T_m and T_p) for low and mid-fluence samples compared to pristine samples. The high-fluence samples exhibit a significant decrease in T_m and T_p , suggesting chain scission. However, the data indicates that across all fluence levels, thermal resetting still takes place. By the second and third heating cycles, the melting temperatures converge, indicating that thermal history is erased after these cycles, even in high-fluence samples. Additionally, no substantial changes in crystallinity are detected, despite variations in heat capacity (C_p), suggesting that electron beam radiation at high fluencies has a lasting impact on LCP but does not drastically alter its crystallinity.

8.2 Influence of FFF on Thermal Properties of Pristine LCP

When comparing pristine sample types, outliers in T_m and T_p from the first heating cycle for pellet samples are disregarded due to noisy data caused by thermal contact loss, preventing definitive conclusions. Consistency is seen across all sample types, with printed samples showing the largest offset in the second and third cycles, a 4°C difference. This may result from sample delamination or variations in punching location, affecting the material's thickness. Delamination expanded the sample's thickness, preventing all layers from fitting into the pan, though it's unclear whether the removed layers were consistently from the top or bottom. Differences in cooling rates may also have influenced molecular alignment. Samples punched from ends, more exposed to ambient temperatures, could cool faster, impacting their properties.

Thermal resetting is observed as T_m and T_p align closely in the second and third cycles as visible in Figure 22A and B. The table in Figure 22D shows that T_m values range from 269°C to 278°C and T_p from 275°C to 285°C, averaging a 4°C decrease per processing step from pellets to printed samples. This reduction may result from processing effects or material batch differences. Higher T_m generally reflects higher crystallinity, as more energy is required to melt crystalline regions. Pellet samples show a larger difference between T_m and T_{mc} , indicating less stable crystalline structures. Literature reports a T_{pc} of 237.5°C, which is

approached by all samples' exotherms. The second cooling cycle shows higher exothermic peaks, with T_{mc} values consistently lower for pellets compared to filament and printed samples. Pellets also exhibit a more significant difference between the first and second cooling cycles in terms of C_p and T_{mc} , whereas filament and printed samples show negligible differences. Comparing ΔH values, visible in Figure 22C, filament and printed samples are similar, while pellets exhibit higher ΔH for the second and third cycles, indicating higher crystallinity. A higher ΔH suggests greater crystallinity, as more energy is needed to melt the crystalline regions.

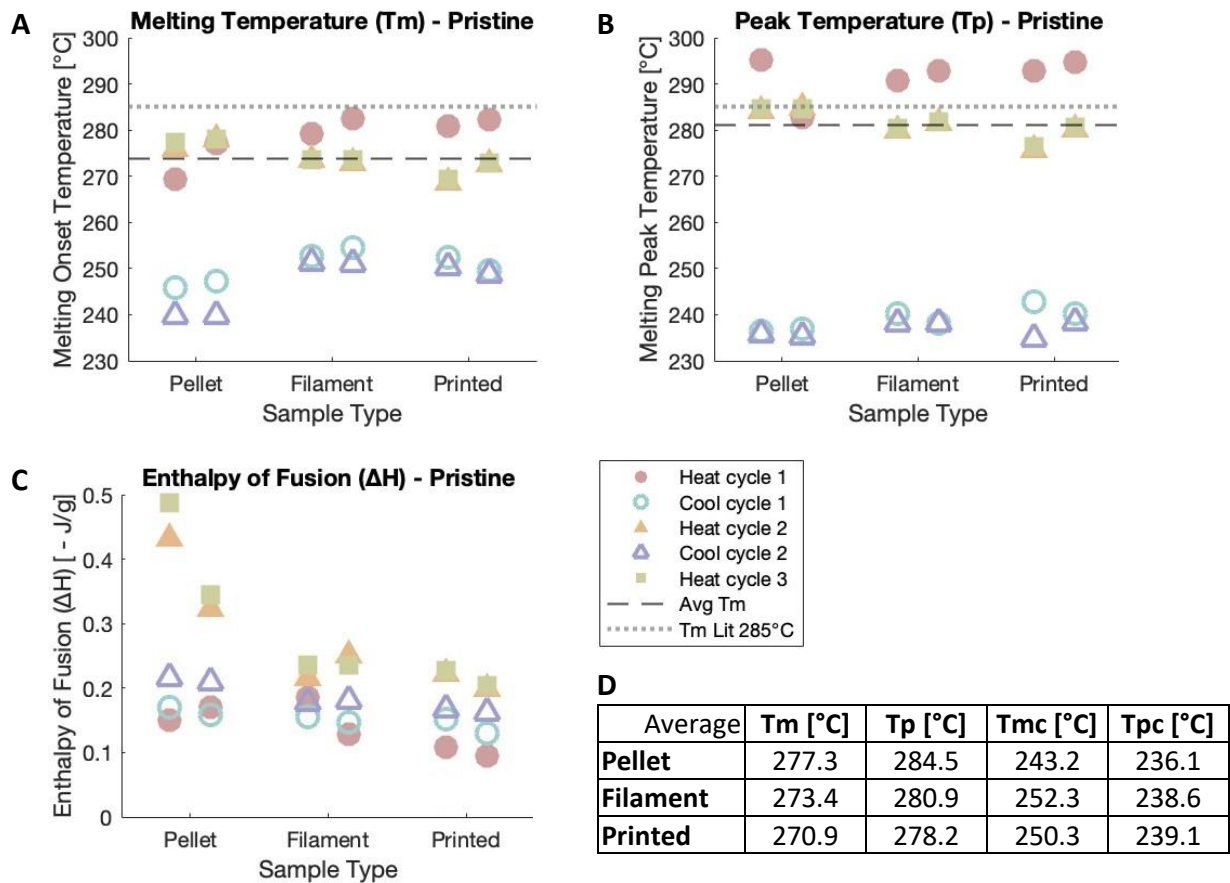


Figure 22: Melting Temperatures and Enthalpy of Fusion for Different FFF Stages of Pristine LCP Measured with DSC. Five cycles were run on DSC: three heating cycles and two cooling cycles, over a temperature range of 25°C to 360°C, with a constant heating rate of 10°C/min. The melting temperatures and enthalpy of fusion of pristine pellets, filament, and printed LCP samples were compared to assess different stages of Fused Filament Fabrication. Filament and printed samples show similar results, while pellets deviate slightly in melting (peak) temperatures and exhibit significantly larger values for enthalpy of fusion. Literature often reports a melting temperature reset to 285°C (...) for the second and third heat cycles of LCP. All samples approach this value with their melting peak temperature. **A.** The average melting temperature of the second and third heat cycle is 273.9°C (---). **B.** The average melting peak temperature of the second and third heat cycle is 281.2°C (---). **C.** Pellet samples exhibit twice the magnitude of enthalpy of fusion compared to filament and printed samples for the second and third heat cycles. **D.** Table showing average temperatures, excluding data from the first heating cycle.

To summarize, a gradual decrease in T_m and T_p by approximately 4°C per processing step suggests processing effects or batch differences. Pellets display a greater difference between solidification T_{mc} and melting temperatures, indicating less stable crystalline structures, and higher crystallinity is reflected by elevated ΔH values in pellets compared to filament and printed samples. FTIR analysis in the next chapter will investigate potential chemical modifications influencing these variations.

8.3 Influence of Annealing LCP on Thermal Properties

Two stages of Fused Filament Fabrication, pellet and filament samples, were annealed in a vacuum oven at 240°C for up to five hours to assess how annealing and FFF processing affect LCP's thermal properties. The first heat cycle for filament and pellet samples showed smoother data compared to the printed samples, making it easier to identify T_m and T_p . As shown in Figure 23A, annealed samples displayed multiple smaller endothermic peaks around 265°C, absent in pristine samples, with a second peak around 290°C, consistent with findings from Johann et al. (2024). Johann et al. (2024) found that unannealed extruded LCP had a second peak around 295°C, while annealed samples showed this peak at 280°C for up to three hours of annealing. After four to five hours, no second peak was observed. Lin & Winter (1988) reported two distinct endothermic peaks in annealed samples: one around 280°C and another 20-30°C above the annealing temperature of 290°C. As annealing time increased, the first peak diminished, while the second peak became more prominent, shifting from 305°C to 315°C. This confirms that annealing temperature significantly affects the melting temperature, with higher annealing temperatures leading to an increase in T_m .

The increase in T_m with higher annealing temperatures is directly related to crystallinity. Annealing allows polymer chains to rearrange into more ordered crystalline structures, strengthening intermolecular forces. As crystallinity rises, more thermal energy is needed to break these forces, raising T_m . In semi-crystalline polymers like LCPs, annealing promotes molecular alignment, increasing crystallinity and thermal stability. Higher T_m reflects the greater heat required to disrupt these stable, ordered regions, while lower crystallinity leads to a lower melting temperature. In this experiment, with the annealing temperature set at 240°C, an endothermic peak was observed around 265°C, approximately 25°C above the annealing temperature, aligning with the findings of Lin & Winter (1988).

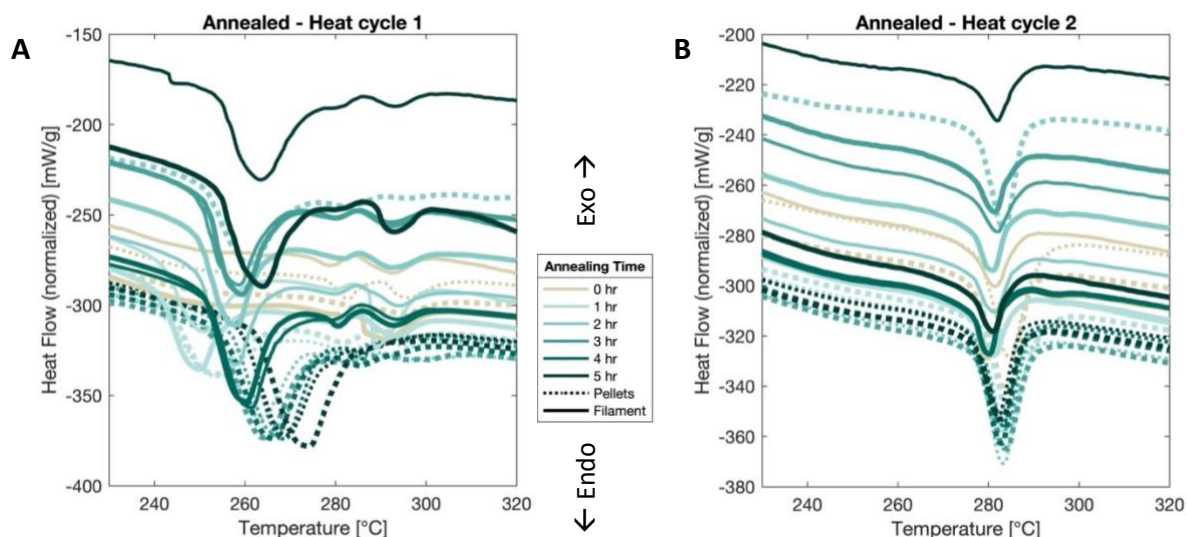


Figure 23: Heat flow as a function of temperature for annealed LCP measured by DSC. Heat flow (ΔQ) traces for the first and second heat cycles of samples annealed at 240°C in vacuum. **(A)** The first cycle shows a prominent peak around $265 \pm 10^\circ\text{C}$, with smaller peaks, including one at 290°C matching unannealed samples. **(B)** The second cycle presents a single, well-defined peak, indicating a thermal reset, consistent across all samples after one cycle. Line thickness distinguishes two identical runs.

The first heating cycle for unannealed filament and printed samples in Figure 24A showed a higher T_m , initially thought to result from unintended annealing during production but likely due to enhanced molecular alignment during extrusion and printing. After one hour of

annealing, T_m and T_p , shown in Figure 24B, dropped but gradually increased with longer annealing, aligning with Romo-Urbe et al. (2022), where longer annealing led to higher T_m and T_p . Contrary to that study, by the fourth and fifth hours of annealing, T_m and T_p did not surpass those of unannealed samples. The second and third heating cycles showed consistent T_m and T_p , indicating thermal resetting, unaffected by longer annealing times. Filament samples show slightly lower T_m and T_p than pellets, likely due to material or processing differences, while their cooling cycles exhibit higher solidification temperatures.

Pellets exhibited a larger difference between T_m and T_{mc} compared to filament, suggesting less stable crystalline structures. Literature reports T_{pc} at 237.5°C, and all samples approaches this value. Figure 24C shows ΔH increased with annealing for the first heat cycle, consistent with literature (Romo-Urbe et al., 2022), indicating greater crystallinity and molecular alignment, with filament samples reaching a stable crystallinity after the first heating cycle. In contrast, pellets showed greater structural changes, requiring more energy to melt during subsequent cycles. This reflects increased crystallinity during cooling.

In summary, the annealing process significantly impact the T_m and T_p of LCP samples, enhancing molecular alignment and crystallinity. However, thermal resetting occurs consistently by the second and third heating cycles across all samples, where T_m and T_p converge to stable values, regardless of prior exposure or processing conditions. This suggests that after the second heat cycle, the material undergoes a "reset," erasing the thermal history from prior exposure, which could potentially aid in future recycling efforts. By eliminating the effects of prior thermal events, this resetting makes the material more amenable to consistent performance in repeated cycles. Filament samples show stable thermal properties, while pellets undergo more significant changes, as evidenced by higher ΔH , aligning with literature findings on annealing's role in enhancing crystallinity.

In conclusion, the thermal resetting observed in the DSC data demonstrates that LCP materials can be effectively recycled, as their thermal properties stabilize after the initial heating cycles. This indicates the material retains its key properties for future use, regardless of prior thermal or processing history. The consistent thermal resetting across different conditions confirms LCP's potential for recycling, which is advantageous for reuse in space missions and other applications. Further studies should explore whether this property can be optimized to enhance recyclability or maintain specific material properties post-exposure.

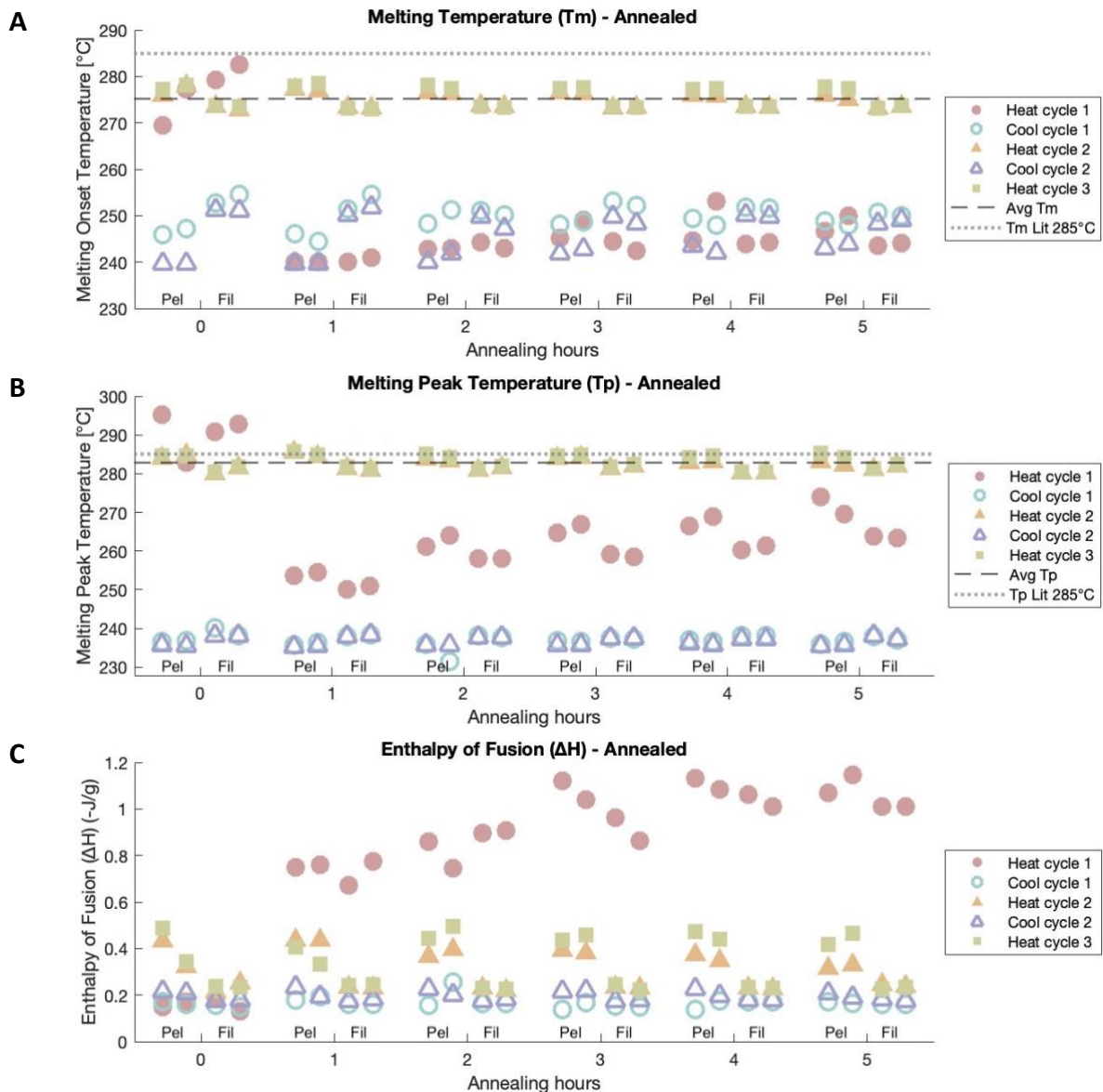


Figure 24: Melting Temperatures and Enthalpy of Fusion of Annealed LCP Measured with DSC. Five cycles were run on DSC: three heating cycles and two cooling cycles, over a temperature range of 25°C to 360°C, with a constant heating rate of 10°C/min. Pellets and filament, representing two stages of FFF, were used to compare the effect of annealing on the melting temperatures and enthalpy of fusion of LCP. The samples were annealed at 240°C for 0 to 5 hours. After an initial steep decrease a gradual increase in melting (peak) temperatures is measured with increasing annealing time. Literature often reports a melting temperature reset to 285°C (...) for the second and third heat cycles of LCP. Pellet samples approach this value more closely than filament samples. **A.** The average melting temperature of the second and third heat cycles is significantly different between sample types; 277.0°C for pellets and 273.4°C for filament, with an average of 275.2°C (---). **B.** The average melting peak temperature of the second and third heat cycle differs slightly between sample types; 284.2°C for pellets and 281.3°C for filament, with an average of 282.7°C (---). **C.** After an initial steep increase, gradual increase in values for enthalpy of fusion is measured with increasing annealing time. Pellet samples exhibit almost twice the magnitude of enthalpy of fusion compared to filament samples for the second and third heat cycles.

9 FTIR Analysis of Space Environment and FFF Effects on LCP

This chapter investigates the effects of electron beam exposure at three different intensities, thermal vacuum cycling (TVAC), and annealing on Liquid Crystal Polymers (LCP) by assessing FTIR spectra. Additionally, the impact of various stages of Fused Filament Fabrication on LCP will be evaluated by comparing pellets, filament, and printed samples. FTIR spectra will be analyzed across the wavelength range of 4000 cm^{-1} to 600 cm^{-1} to identify shifts in absorption peaks, which reveal changes in molecular structure and chemical composition.

Characteristic peaks in the FTIR spectrum correspond to specific vibrational modes or transitions within a molecule. A comprehensive table listing the wavelengths and attributions of these peaks based on literature for various polymers can be found in Appendix F. Table in Figure 25C highlights wavelength regions and their attributions relevant to the chemical structure of LCP Vectra A950, which consists of HBA and HNA monomers in a 73:27 ratio, shown in Figure 25A as separate monomers and in Figure 25B after polymerization forming a polymeric chain.

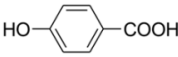
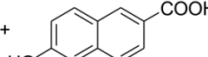
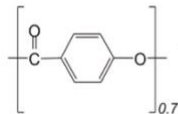
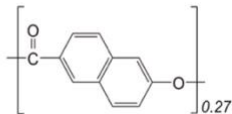
A		C	
		Functional Group	Wavelength Range (cm^{-1})
A		O-H stretching	3200–3600
		Aromatic C-H stretching	3024
		C-H stretching	2990–2840
		=C-H stretching	2917, 2849
		Aromatic ring stretching	1600-1400, 900
		C=O stretching	1770–1710, 1634, 1223
		C=C stretching	1600, 1150
		C-O stretching	1240–1020
B			
			

Figure 25: Chemical Structure and Key Characteristic Peaks in the FTIR Spectra of LCP Vectra A950. A. The chemical structure of the HBA and HNA monomers that comprise LCP Vectra A950 (Padias & Hall, 2011). B. The chemical backbone of LCP Vectra A950 after polymerization (Romo-Urbe et al., 2022). C. Wavelengths and attributes of characteristic peaks in the FTIR Spectra relevant of LCP Vectra A950 (Veerasingam et al., 2021).

FTIR can detect chain scission by identifying changes in the intensity and position of specific absorption peaks related to functional groups in the polymer's backbone. Decreased intensity or shifts in these peaks indicate the breaking of chemical bonds and changes in the polymer structure.

FTIR can detect crosslinking, by looking for disappearance or changes in peak intensities, positions and shapes. Crosslinking often involves the reaction of functional groups such hydroxyl or carbonyl groups. Additionally, the formation of new peaks or changes in the position of existing peaks can signal the creation of new bonds. Peaks attributed to C-O stretches could indicate the formation of new ether or ester bonds.

9.1 Influence of Electron Beam on FTIR Spectra of LCP

FTIR spectra of pristine and electron beam-exposed 3D-printed LCP samples at three different fluences were recorded in December (139 days post-exposure) and in June (332 days post-exposure). Both sets of spectra are shown in Figure 26. Although identical specimens could not be used for both measurements, all samples are from the same printing batch and were irradiated during the same cycle.

In the FTIR spectra recorded in December, prominent peaks around 2923 and 2853 cm^{-1} are observed for irradiated samples, likely corresponding to C-H stretching, visible in Figure 26A.

A minor peak at these wavelengths is noted for the unirradiated sample. These peaks are absent in the June spectra for all samples, and their disappearance is not fully understood. Since these spectra were collected from a single location on each sample, it is advisable to perform FTIR measurements at multiple sites on each sample. Ideally, at least ten different locations should be analyzed to account for potential variability and ensure a comprehensive analysis.

For lower wavelengths, peaks remain consistent across different fluences and between December and June, as depicted in Figure 26B. This figure illustrates wavelengths associated with aromatic ring stretching, C=C stretching, and C=O stretching. A change in peaks attributed to C=C stretching was not anticipated, as it would have been indicated by a significant alteration in the tensile properties of irradiated samples. Additionally, C-O bonds are more likely to be affected than C=C bonds. Peaks related to C-O stretching, occurring at even lower wavelengths and not shown in Figure 26B, also exhibited no changes.

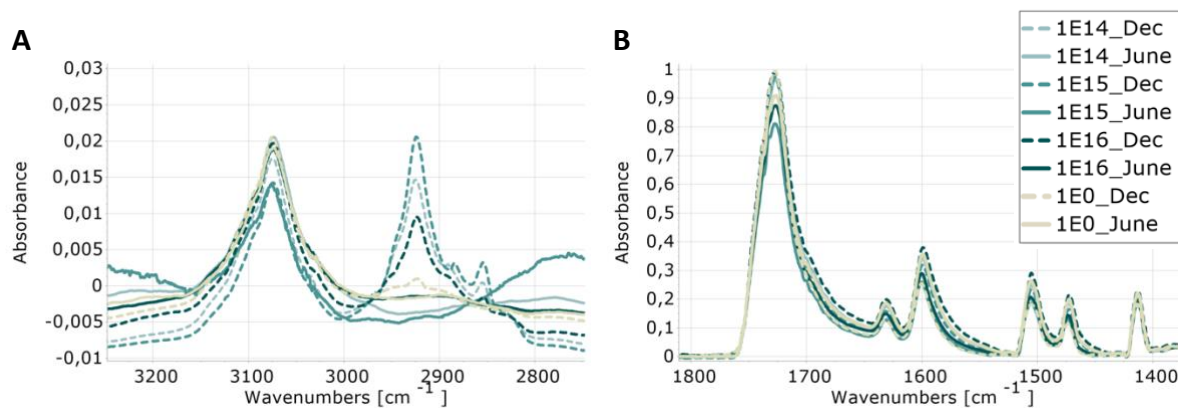


Figure 26: FTIR Absorption Spectra of LCP Exposed to Electron Beam. Electron beam irradiation was applied at three intensities in July 2023, with FTIR measurements conducted in December 2023 and June 2024 on unirradiated and irradiated samples. **(A)** FTIR spectra from December 2023 reveal peaks around 2923 cm^{-1} and 2853 cm^{-1} , indicating C-H stretching. These peaks are prominent in the irradiated samples from December but are absent in the June 2024 spectra. **(B)** No significant differences are observed in the spectra at low wavenumbers, where changes associated with aromatic ring, C=C, and C=O stretching would appear.

In summary, FTIR spectra of 3D-printed LCP samples show consistent peaks, except for fluctuations in C-H stretching, which were present in December but absent in June. This variability suggests the need for measurements at multiple locations.

9.2 Influence of TVAC and Electron Beam on FTIR Spectra of LCP

Pristine and electron beam-irradiated samples were subjected to 25 cycles of thermal vacuum cycling (TVAC) between -100°C and $+100^{\circ}\text{C}$, with a heating rate of $5^{\circ}\text{C}/\text{min}$. The FTIR spectra of the unirradiated sample exposed only to TVAC showed no peaks between 3050 and 3100 cm^{-1} , shown in Figure 27A, which are typically attributed to aromatic C-H stretching. A peak attributed to O-H stretching between 3160 and 3220 cm^{-1} was observed for high fluence and unirradiated samples, but was absent for low and mid fluence samples. Peaks at 2923 and 2853 cm^{-1} , associated with C-H stretching, were present in all samples. The most prominent C-H stretching peaks were observed in both unirradiated and high fluence irradiated samples. Variations in peak sizes may have resulted from differences in normalization and smoothing methods applied to the data, though all samples exhibited C-H stretching peaks regardless of the method. At lower wavenumbers, visible in Figure 27B, around 1720 cm^{-1} , unirradiated

samples showed a less prominent peak compared to irradiated samples. This peak likely associated with C=O stretching.

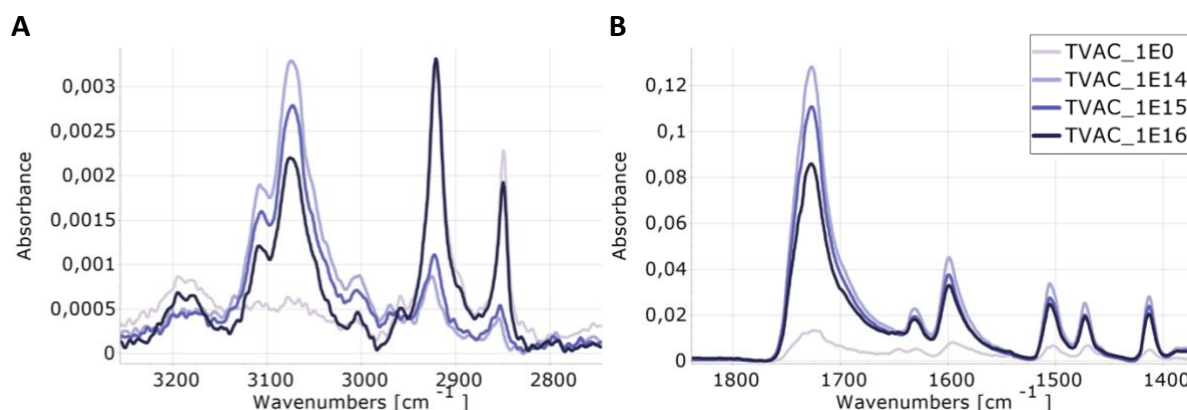


Figure 27: FTIR Absorption Spectra of LCP Exposed to Electron Beam and TVAC. Previously irradiated and unirradiated samples were subjected to 25 thermal cycles under vacuum, with a temperature range of -100°C to $+100^{\circ}\text{C}$ and a heating rate of $5^{\circ}\text{C}/\text{min}$, FTIR measurements conducted in December 2023. **(A)** FTIR spectra reveal peaks around 2923 cm^{-1} and 2853 cm^{-1} , indicating C-H stretching, for all samples. These peaks are most prominent in the unirradiated samples and those irradiated at the highest fluence. A peak around 3080 cm^{-1} , indicative of aromatic C-H stretching, is observed in all irradiated samples, while it is absent in the unirradiated sample only exposed to TVAC. **(B)** At low wavenumbers, unirradiated samples show a less prominent peak around 1720 cm^{-1} , indicating C=O stretching, compared to the irradiated samples showing more prominent peaks.

In summary, FTIR analysis revealed that high fluence samples exhibited an O-H stretching peak absent in lower fluence samples, while unirradiated samples showed no aromatic C-H stretching peak. The C-H stretching peaks were most prominent in unirradiated and high fluence samples. A less prominent C=O stretching peak around 1720 cm^{-1} was observed in unirradiated samples compared to irradiated ones.

9.3 Influence of Annealing on FTIR Spectra of LCP

A pristine sample and a sample exposed to high fluence electron beam radiation were annealed for one hour at 200°C in a vacuum oven. Figure 28A shows that the C-H stretching peaks at 2923 and 2853 cm^{-1} reappeared only in the high fluence irradiated sample after annealing, not in the unirradiated sample. Additionally, annealing a pristine sample at 240°C in vacuum for 4 hours did not result in the appearance of C-H stretching peaks. No fluctuations in peaks were observed at low wavelengths, as shown in Figure 28B.

The precise cause of the disappearance of C-H stretching peaks between December and June, followed by their reappearance after annealing, remains unclear. The samples were meticulously cleaned with isopropanol between scans and handled exclusively with gloves to minimize contamination. This phenomenon may be linked to the generation of free radicals due to electron beam irradiation, as discussed in Chapter 5. Free radicals are unstable and tend to revert to a stable state through self-quenching. It is possible that the annealing process reactivated some of the electrons still trapped in the material, leading to the formation of new radicals and the subsequent reappearance of the C-H stretching peaks.

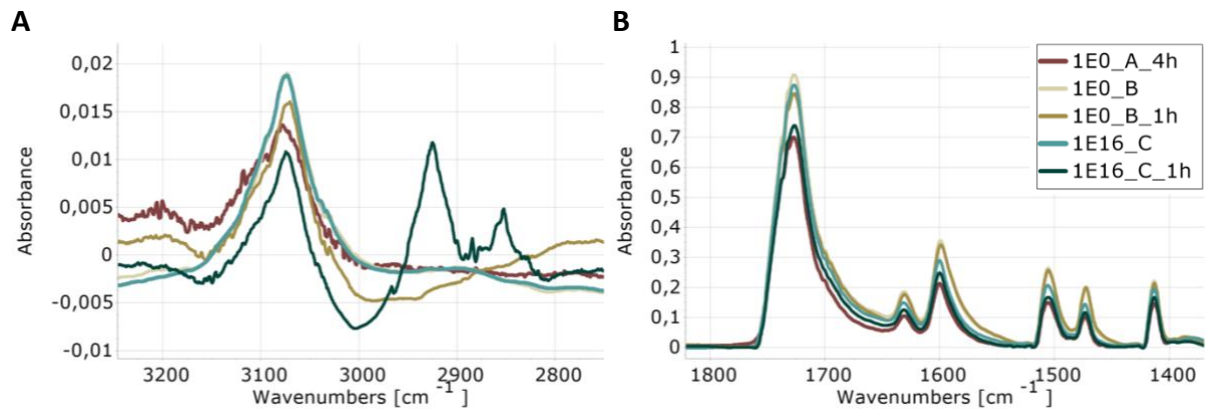


Figure 28: FTIR Absorption Spectra of Annealed LCP. Comparison of unirradiated [1E0_B] and irradiated at high fluence [1E16_C] samples, before and after annealing for 1 hour at 200°C, as well as an unirradiated sample annealed for 4 hours [1E0_A], FTIR measurements were conducted in June 2024. **(A)** FTIR spectra reveal peaks around 2923 cm^{-1} and 2853 cm^{-1} , indicating C-H stretching, only in the high fluence sample after annealing. **(B)** No significant differences are observed in the spectra at low wavenumbers, where changes associated with aromatic ring, C=C, and C=O stretching would appear.

In summary, C-H stretching peaks reappeared only in the high fluence irradiated sample after annealing, while no peaks were observed in the unirradiated sample after annealing, suggesting that the reappearance may be linked to the reactivation of free radicals.

9.4 Influence of FFF on FTIR Spectra of Pristine LCP

To evaluate the impact of Fused Filament Fabrication (FFF) on LCP, comparisons were made among pellets, filament, and printed samples. Figure 29 reveals that there is no discernible difference in the chemical backbone across the different stages of FFF as measured by FTIR. Pellets, filament, and printed parts exhibit similar peaks across all wavelengths, indicating no variation in chemical bonds.

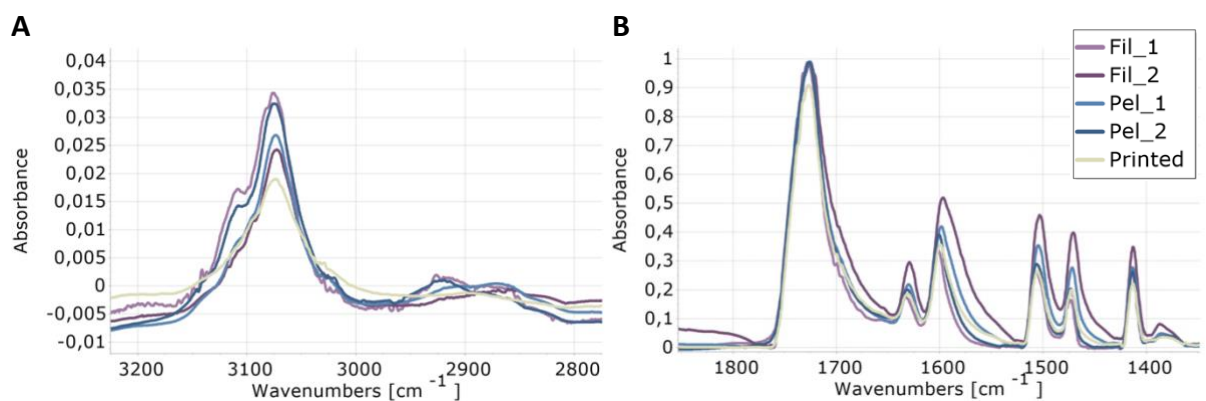


Figure 29: FTIR Absorption Spectra for Different FFF Stages of Pristine LCP. FTIR measurements of pellets, filament, and 3D-printed samples, conducted in June 2024. **(A)** No significant differences are observed at high wavenumbers, where C-H stretching can be detected. **(B)** No significant differences are observed at low wavenumbers, where changes related to aromatic ring, C=C, and C=O stretching would appear.

10 Discussion

This chapter addresses the three sub-questions that guide the main research question, each considered separately. The first section examines the impact of electron beam radiation and thermal vacuum on the mechanical properties of LCP. The second section evaluates their effect on LCP's thermal resistance, while the third explores how annealing and Fused Filament Fabrication (FFF) processing influence LCP's recyclability for space applications.

10.1 Influence of Space Environment on Mechanical Properties of LCP

Exposure to electron beam radiation and thermal vacuum cycling affects the mechanical properties of LCP. Electron irradiation induced annealable color centers, resulting in a green hue that intensified with increasing radiation dose. However, increase in color intensity did not correlate with tensile properties, as no significant changes in Young's modulus or UTS were observed with increasing radiation fluence or after thermal vacuum cycling of high fluence samples. Additionally, TVAC exposure further decreases Young's modulus, with a decrease of 30-35% noticed at lower printing temperatures, and merely 10% at high printing temperatures. Contrary, TVAC exposure has minimal impact on UTS, decrease of 10-20% at low printing temperatures, and negligible 2-6% at higher temperatures. For UD90 samples, printing temperatures had minimal impact on Young's Modulus, but UTS improved slightly, by $\pm 14\%$ per increase of 15°C with higher temperatures, likely due to better interlayer bonding. For UD0 samples, increasing printing temperatures result in a reduction of both Young's modulus and UTS by approximately 22% and 13%, respectively, for every 15°C rise. This reduction is attributed to increased molecular disorder, as longer solidification times at higher temperatures allow nematic domains to relax into less ordered configurations. Additionally, TVAC exposure further reduces Young's modulus, with a more pronounced decrease of 30-35% at lower printing temperatures and only about 10% at higher temperatures. In contrast, TVAC has minimal impact on UTS, causing a 10-20% reduction at low temperatures, but only 2-6% at higher temperatures. For UD90 samples, printing temperatures have little effect on Young's modulus, but UTS improves slightly by about 14% per 15°C increase, likely due to enhanced interlayer bonding. Exposure to TVAC slightly reduced Young's Modulus and UTS, except for samples printed at 340°C , which showed increased resilience, potentially from enhanced layer fusion or crosslinking.

Comparing pristine samples to irradiated and TVAC-exposed samples requires caution, as the pristine samples were printed later, potentially introducing variability from non-simultaneous printing. To reduce this variability, future studies should print samples simultaneously under identical conditions and use a larger batch randomly distributed among pristine and exposed groups. Non-invasive methods like X-ray diffraction could assess molecular alignment before and after exposure to detect any anomalies.

DMA samples were printed simultaneously and randomly distributed across the pristine, three exposure intensities, TVAC, and annealing batches. Electron beam radiation caused a decrease in storage and loss modulus, insinuating a loss of stiffness, and an increase in the damping factor ($\tan \delta$) with increasing fluence, all suggesting chain scission occurred. After TVAC exposure, high-fluence samples retained a higher $\tan \delta$ amplitude for the α -peak than the β -peak, while the other samples showed a larger β -peak amplitude. Post-annealing, the storage modulus remained higher for unirradiated and low-fluence samples, with $\tan \delta$ increasing with exposure intensity. All annealed samples exhibited a larger β -peak $\tan \delta$

amplitude, suggesting that annealing enhanced the polymer's chain mobility and flexibility, likely through relaxation of internal stresses, in addition to removing color centers.

FTIR analysis showed no apparent change in C=C bonds for any samples, consistent with the tensile results, as such changes would significantly reduce tensile properties. All irradiated samples exposed to TVAC exhibited prominent C=O and aromatic C-H stretching compared to unirradiated samples. FTIR also detected C-H stretching in irradiated and TVAC-exposed samples, likely due to the unstable free radicals in the material, as these signals were absent in pristine samples, faded over time, and reappeared after annealing in the irradiated samples.

In conclusion, exposure to electron beam radiation and thermal vacuum do have an impact on the mechanical properties of LCP. The presence of annealable color centers suggests that electron radiation did not cause significant changes to the backbone of LCP, as evidenced by the lack of substantial changes in tensile properties both after irradiation and subsequent TVAC exposure. However, unirradiated samples exposed to TVAC showed a decrease in tensile properties. DMA results indicated a lower storage modulus for samples irradiated with mid and high fluence, while FTIR revealed slight alterations in chemical bonds. These changes support the hypothesis that high radiation exposure rates lead to degradation and potential chain modifications, such as chain scission, in addition to the formation of unstable free radicals. LCP demonstrated less susceptibility to the space environment compared to other 3D-printed polymers discussed in the literature review of this thesis, those polymers showed equal or greater degradation when exposed to similar space conditions (Briskman, 2003; Dawes et al., 2007). LCP surpasses the material properties of these polymers (Cicala et al., 2018; Gantenbein et al., 2018) and is recognized as the only polymer approaching the performance of top metal choices for aerospace structures, particularly for weight reduction and rapid demise during atmospheric re-entry (Slejko et al., 2021).

10.2 Influence of Space Environment on Thermal Resistance of LCP

Exposure to electron beam radiation and thermal vacuum cycling impacts the thermal resistance of LCP. Electron beam radiation causes modest changes in DMA measurements with increasing fluence, including a shift in the HNA moiety's (β -peak) temperature, while the glass transition temperature (T_g) remains unchanged. After TVAC exposure T_g rises by nearly 5°C, indicating increased crosslinking. Following annealing of irradiated samples, the β -peak temperature decreases, and T_g increases only for the high-fluence sample, possibly due to enhanced crosslinking, though caution is advised as this result is based on a single sample.

Color centers fade over time or disappear after annealing, but samples irradiated with high fluence show an irreversible decrease in melting temperature of over 7°C. Additionally, these samples exhibited significant shrinkage and dark discoloration when exposed to high temperatures, effects not observed in the other samples. This indicates permanent polymer modifications, such as chain scission, possibly due to the eradication of unstable free radicals during heating above the glass transition temperature, as the samples were heated above their melting temperature during the first DSC heat cycle.

In conclusion, low doses of electron beam radiation, comparable to LEO, do not significantly affect LCP, while high doses cause a permanent decrease in melting temperature, possibly due to chain scission. Irradiation does not affect T_g , whereas TVAC exposure increases it, suggesting that TVAC promotes crosslinking. The radiation doses in this study were selected

to be comparable to direct space exposure in LEO and GEO. However, with the use of shielding, coatings, or applying LCP on the interior of the spacecraft, the exposure doses can be significantly reduced.

10.3 Influence of Electron Beam, Annealing and FFF Processing on Recyclability of LCP

Electron beam radiation, annealing, and FFF processing all influence the thermal and mechanical properties of LCP, suggesting affecting recyclability. However, the degree of these changes and whether they are reversible varies depending on the process and exposure intensity. Exposure to electron beam radiation induces modest but noticeable changes in material properties of LCP. While samples exposed to low and mid fluence showed minimal changes, those subjected to high fluence exhibited permanent structural damage, reflected by a significant decrease in melting temperatures, indicating that chain scission weakened the polymer structure. This implies that recyclability may be reduced at higher radiation doses, potentially limiting its ability to undergo further processing without degrading its properties. Annealing and FFF processing both impact the recyclability of LCP, but these effects may be thermoreversible. Higher printing temperatures during FFF tend to reduce Young's modulus and UTS due to increased molecular disorder, which affects the material's mechanical stability. The recyclability of samples printed at varying temperatures, was not within the scope of this research, further research should be done to assess the thermoreversibility of these mechanical property changes after recycling.

DSC data suggest that annealing time and temperature significantly impact the melting temperature (T_m) and peak temperature (T_p), with longer annealing increasing molecular alignment and crystallinity. However, in subsequent heating cycles, T_m and T_p converge to similar values, indicating a thermal reset of the melting temperatures that is unaffected by extended annealing. This indicates that, in terms of thermal behavior, annealing is likely reversible, and the material may retain its recyclability potential. Filament samples exhibit stable thermal properties over multiple cycles, while pellets show greater structural reorganization, requiring more energy to melt. These differences likely result from the additional processing involved in filament production, which may not be thermoreversible.

FTIR analysis shows no major changes in the chemical backbone between the different stages of FFF, suggesting that the FFF process does not chemically alter the polymer, further supporting its recyclability potential. However, fluctuations in C-H stretching observed in FTIR measurements for irradiated samples suggest the need for more localized analysis to ensure consistency in the polymer's properties across different regions.

Electron beam radiation, especially at high fluence, has a lasting effect on LCP that could reduce its recyclability potential due to chain scission, which weakens the polymer's mechanical properties. However, annealing and FFF processing appear to have thermoreversible effects, particularly on crystallinity, suggesting that these processes may not significantly hinder recyclability. Further research is needed to better understand the long-term impacts of FFF on mechanical properties and whether repeated recycling processes will affect the material's integrity, particularly in the context of in-situ recycling during planetary exploration.

11 Conclusion

Below is a bullet-point summary of this research addressing the research question:

“What is the impact of exposure to electron beam radiation and TVAC on the material properties of 3D-printed LCP, and how does this influence its space-worthiness?”

Mechanical properties:

- Exposure to electron beam radiation and TVAC had minor effects on LCP's mechanical properties.
- Electron irradiation caused annealable color centers, with no significant impact on tensile properties (Young's modulus or UTS).
- TVAC slightly reduced Young's modulus, especially at lower printing temperatures, but had minimal effect on UTS.
- DMA showed decreased storage modulus with increasing fluence, indicating reduced stiffness.
- FTIR detected chemical bond alterations from unstable free radicals, but overall mechanical integrity remained intact.

Thermal properties:

- Electron radiation modestly shifted the β -peak temperature but did not alter T_g .
- TVAC increased T_g by approximately 5°C, possibly due to crosslinking.
- High fluence caused a permanent decrease in melting temperature by over 7°C, suggesting chain scission and irreversible polymer structure changes.
- Lower fluence levels had minimal thermal impact, indicating thermal stability under moderate radiation.

Recyclability:

- ◆ Electron radiation, annealing, and FFF processing influenced LCP's properties, with changes potentially being thermoreversible.
- ◆ Higher printing temperatures reduced mechanical stability.
- ◆ Annealing increased crystallinity, but thermal reset of melting temperatures suggests minimal recyclability impact.
- ◆ FTIR confirmed FFF processing did not chemically alter the polymer, supporting recyclability.

The findings indicate that LCP is a promising material for space applications, similar to its melt-spun counterpart Vectran™, which is already utilized in space. LCP largely retains its mechanical and thermal properties under moderate exposure to electron beam radiation and thermal vacuum. Although high fluence levels induce some irreversible changes, the material's stability at moderate exposure levels, along with its recyclability potential, makes it a viable candidate for long-term use in the challenging conditions of space. To minimize degradation at higher doses, the application of shielding or protective coatings could be employed to safeguard LCP from direct exposure. While LCP was not more susceptible to space environments than other 3D-printed polymers, it outperforms them in terms of material properties, nearing those of top metal choices for aerospace applications. Further research is recommended to investigate the impact of various printing conditions and recycling methods to enhance its performance and sustainability in space environments.

12 Recommendations for Future Research

This study provided new insights into the behavior of 3D-printed LCP under space-like conditions, but several areas of improvement and further exploration are recommended for future work to deepen the understanding of LCP's performance in space applications. The electron particles used in this study did not cause significant damage to LCP, likely due to their relatively small particle size and mass compared to other types of space radiation, such as galactic cosmic rays or solar proton events. To gain a more comprehensive understanding of LCP's resilience, future studies should subject the material to a broader spectrum of radiation types under vacuum conditions, as suggested by previous research, to better simulate real space environments. Additionally, investigating the combined effects of multiple exposure types would provide insight into potential synergistic damage. UV and ATOX have been shown to cause superficial harm to LCP, potentially enabling other radiation types to amplify this damage. To further investigate these effects, LCP is scheduled for space exposure aboard SpaceX's SpX-31 mission, with a tentative launch date no earlier than October 30, 2024.

The unexpected color change in irradiated LCP samples, which faded after 20 days, should be better documented in future studies. Intermediate photographic evidence over time could provide insight into the progression of color fading and the role of annealable color centers. Exposure to thermal vacuum conditions resulted in decreased Young's modulus and UTS in LCP, but more precise re-evaluation is required. Future tensile testing should aim to minimize variability in material properties by printing larger batches of samples simultaneously under identical conditions. Randomizing the assignment of samples to pristine and exposed groups would reduce manufacturing variability. Additionally, non-invasive techniques such as XRD should be used to quantify molecular alignment before and after thermal cycling to detect anomalies or variations.

To improve the accuracy of DSC results, LCP samples should be printed to fit exactly in the pan, ensuring optimal thermal contact. Immersing samples in silicone oil or embedding them in Kapton film would allow for free expansion and contraction, reducing thermal noise. It is also recommended to print samples at different temperatures and assess the influence of varying print temperatures on recyclability. Further testing could include analyzing high fluence samples in DSC after DMA testing, investigating whether they melt differently, and conducting FTIR analysis to detect any irreversible changes.

The extreme shrinkage and discoloration of high fluence samples exposed to elevated temperatures warrant further investigation. Identifying what caused these changes in optical and material properties—whether through crosslinking, chain scission, or radical interaction—could provide deeper insights. Additional testing, such as FTIR or EPR spectroscopy, could help determine the nature of these changes, particularly in distinguishing between permanent and annealable effects.

An additional avenue for future research is investigating whether Vectran™ (woven fiber form) can be recycled into Vectra® (3D-printable form) and vice versa. Establishing this recycling loop would contribute to resource sustainability, particularly for long-duration space missions.

By addressing these recommendations, future research could provide a more comprehensive evaluation of LCP's space-worthiness and recyclability, critical for advancing sustainable space exploration.

Works Cited

- Andrienko, D. (2018). Introduction to liquid crystals. *Journal of Molecular Liquids*, 267, 520–541. <https://doi.org/10.1016/j.molliq.2018.01.175>
- Ashfaq, A., Clochard, M.-C., Coqueret, X., Dispenza, C., Driscoll, M. S., Ulański, P., & Al-Sheikhly, M. (2020). Ashfaq 2020 - Polymerization Reactions and Modifications of Polymers by Ionizing Radiation. *Polymers (Basel)*, 12, 67. <https://doi.org/https://doi.org/10.3390%2Fpolym12122877>
- Blackwell, J., & Biswas, A. (1987). STRUCTURE AND PROPERTIES OF THERMOTROPIC LIQUID CRYSTALLINE COPOLYESTERS. In I. M. Ward (Ed.), *DEVELOPMENTS IN ORIENTED POLYMERS* (Vol. 2, pp. 153–197). ELSEVIER APPLIED SCIENCE.
- Briskman, B. A. (2003). RADIATION EFFECTS OF PROTON COLLISIONS IN POLYMERS. *Proceedings of the 9th International Symposium on Materials in a Space Environment Noordwijk, The Netherlands, 16-20 June 2003*, 649–654.
- Briskman, B., Klinshpont, E., & Tupikov, V. (1999). *Space environment simulation at radiation test of nonmetallic materials: Vol. ESA*. www.elsevier.nl/locate/nimb
- Brown, J. R., & O'Donnell, J. H. (1979). Effects of gamma radiation on two aromatic polysulfones. II. A comparison of irradiation at various temperatures in air-vacuum environments. *Journal of Applied Polymer Science*, 23(9), 2763–2775. <https://doi.org/10.1002/app.1979.070230921>
- Cadogan, D., Sandy, C., & Grahne, M. (2002). DEVELOPMENT AND EVALUATION OF THE MARS PATHFINDER INFLATABLE AIRBAG LANDING SYSTEM. In *Acta Astronautica* (Vol. 50, Issue 10). www.elsevier.com/locate/actaastro
- Celanese. (2013). *LCP-027_VectraLCPDesignGuideTG_AM_0613*.
- Cheng, S. Z. D. (1988). Kinetics of Mesophase Transitions in Thermotropic Copolyesters. 1. Calorimetric Study. In *Macromolecules* (Vol. 21). <https://pubs.acs.org/sharingguidelines>
- Chung, T. S., Cheng, M., Goh, S. H., Jaffe, M., & Calundann, G. W. (1999). Revisit the crystallization mechanism of vectra, a liquid crystal polymer. *Journal of Applied Polymer Science*, 72(9), 1139–1150. [https://doi.org/10.1002/\(SICI\)1097-4628\(19990531\)72:9<1139::AID-APP4>3.0.CO;2-O](https://doi.org/10.1002/(SICI)1097-4628(19990531)72:9<1139::AID-APP4>3.0.CO;2-O)
- Cicala, G., Ognibene, G., Portuesi, S., Blanco, I., Rapisarda, M., Pergolizzi, E., & Recca, G. (2018). Comparison of Ultem 9085 used in fused deposition modelling (FDM) with polytherimide blends. *Materials*, 11(2). <https://doi.org/10.3390/ma11020285>
- Clough, R. L. (2001). *High-energy radiation and polymers: A review of commercial processes and emerging applications*. www.elsevier.com/locate/nimb
- Clough, R. L., Gillen, K. T., Malone, G. M., & Wallace, J. S. (1996). ~) Pergamon COLOR FORMATION IN IRRADIATED POLYMERS. In *Radiat. Phys. Chem* (Vol. 48, Issue 5).
- Collyer, A. A. (1996). Introduction to liquid crystal polymers. In D. Acierno & A. A. Collyer (Eds.), *Introduction to liquid crystal polymers* (pp. 1–29). Chapman & Hall.
- Cowie, J. M. G., & Arrighi, V. (2007). *Polymers: Chemistry and Physics of Modern Materials* (Third Edition). CRC Press.

- Dawes, K., Glover, L. C., & Vroom, D. A. (2007). *The Effects of Electron Beam and g-Irradiation on Polymeric Materials* (pp. 867–887).
- de Groh, K. K., Banks, B. A., Miller, S. K. R., & Dever, J. A. (2018). Degradation of spacecraft materials. In *Handbook of Environmental Degradation Of Materials: Third Edition* (pp. 601–645). Elsevier Inc. <https://doi.org/10.1016/B978-0-323-52472-8.00029-0>
- Dierking, I. (2010). Recent developments in polymer stabilised liquid crystals. *Polymer Chemistry*, 1(8), 1153. <https://doi.org/10.1039/c0py00087f>
- El-Naggar, A. M., Kim, H. C., López, L. C., & Wilkes, G. L. (1989). Electron beam effects on polymers. III. Mechanical and thermal properties of electron beam-irradiated poly(phenylene sulfide). *Journal of Applied Polymer Science*, 37(6), 1655–1668. <https://doi.org/10.1002/app.1989.070370618>
- Exner, G., Pérez, E., & Krasteva, M. (2015). Structure and Phase Transitions of Polymer Liquid Crystals, Revealed by Means of Differential Scanning Calorimetry, Real-Time Synchrotron WAXD, MAXS and SAXS and Microscopy. In *Liquid Crystalline Polymers: Volume 1- Structure and Chemistry* (pp. 19–52). Springer International Publishing. https://doi.org/10.1007/978-3-319-22894-5_2
- Fruit, M., Berghmans, F., Ulbrich, G., Gussarov, A., & Doyle, D. (2017). *Radiation impact on the characteristics of optical glasses test results on a selected set of materials*. 56. <https://doi.org/10.1117/12.2307918>
- Gantenbein, S., Masania, K., Woigk, W., Sesseg, J. P. W., Tervoort, T. A., & Studart, A. R. (2018). Three-dimensional printing of hierarchical liquid-crystal-polymer structures. *Nature*, 561(7722), 226–230. <https://doi.org/10.1038/s41586-018-0474-7>
- Gantenbein, S., Mascolo, C., Houriet, C., Zboray, R., Neels, A., Masania, K., & Studart, A. R. (2021). Spin-Printing of Liquid Crystal Polymer into Recyclable and Strong All-Fiber Materials. *Advanced Functional Materials*, 31(52). <https://doi.org/10.1002/adfm.202104574>
- Hamley, I. W., Garnett, S., Luckhurst, G. R., Roskilly, S. J., Skov Pedersen, J., Richardson, R. M., & Seddon, J. M. (1996). Orientational ordering in the nematic phase of a thermotropic liquid crystal: A small angle neutron scattering study. *Journal of Chemical Physics*, 104(24), 10046–10054. <https://doi.org/10.1063/1.471759>
- Hanks, C. L., & Hamman, D. J. (1971). *RADIATION EFFECTS DESIGN HANDBOOK Section 3. Electrical Insulating Materials and Capacitors*.
- Hopkins, N., Jiang, L., & Brooks, H. (2021). Energy consumption of common desktop additive manufacturing technologies. *Cleaner Engineering and Technology*, 2. <https://doi.org/10.1016/j.clet.2021.100068>
- Hou, L., Wu, Y., Xiao, J., Guo, B., & Zong, Y. (2019). Colored effects and mechanism in DDM-cured epoxy after 170 keV vacuum electron irradiation. *Nuclear Instruments and Methods in Physics Research, Section B: Beam Interactions with Materials and Atoms*, 439, 1–6. <https://doi.org/10.1016/j.nimb.2018.11.002>
- Islam, M. T., Kamal, T., Shin, T., Seong, B., & Park, S. Y. (2014). Self-assembly of a liquid crystal ABA triblock copolymer in a nematic liquid crystal solvent. *Polymer*, 55(16), 3995–4002. <https://doi.org/10.1016/j.polymer.2014.06.009>

- Jaffe, M., Cheng, S., Chung, T., Freidzon, Y., & East, A. J. (2018). Thermotropic Liquid Crystalline Polymers. In *Encyclopedia of Polymer Science and Technology* (pp. 1–24). Wiley. <https://doi.org/10.1002/0471440264.pst180.pub2>
- Johann, K. S., Wolf, A., & Bonten, C. (2024). Mechanical Properties of 3D-Printed Liquid Crystalline Polymers with Low and High Melting Temperatures. *Materials*, *17*(1). <https://doi.org/10.3390/ma17010152>
- Kalfon-Cohen, E., Marom, G., Wachtel, E., & Pegoretti, A. (2009). Characterization of drawn monofilaments of liquid crystalline polymer/carbon nanoparticle composites correlated to nematic order. *Polymer*, *50*(7), 1797–1804. <https://doi.org/10.1016/j.polymer.2009.02.002>
- Kim, Y. C., & Economy, J. (1999). Degradation process observed during step annealing of 73/27 HBA/HNA copolyester. *Macromolecules*, *32*(9), 2855–2860. <https://doi.org/10.1021/ma981552t>
- Kong, Y., & Hay, J. N. (2002). *The measurement of the crystallinity of polymers by DSC*. www.elsevier.com/locate/polymer
- Limeneh, D. Y., & Yilma, K. T. (2021). Article Review on Vectran-Super Fiber from Thermotropic Crystals of Rigid-Rod Polymer. In *Journal of Engineering (United Kingdom)* (Vol. 2021). Hindawi Limited. <https://doi.org/10.1155/2021/6646148>
- Lin, Y. G., & Winter, H. H. (1988). Macro-molecules. In *Berlman, I. B. Energy Transfer Parameters of Aromatic Compounds* (Vol. 21, Issue 16). Academic. <https://pubs.acs.org/sharingguidelines>
- Litteken, D. (2019). *Passive Wireless Sensor Technology (PWST) Workshop Session S6-A*.
- Mulligan, D. R., Imrie, C. T., & Larcey, P. (1996). Characterization: of side-chain liquid crystal polymers using dynamic mechanical thermal analysis and dielectric thermal analysis. In *JOURNAL OF MATERIALS SCIENCE* (Vol. 31).
- NASA. (2020, July 28). *NASA's Perseverance Rover Will Carry First Spacesuit Materials to Mars*. NASA Jet Propulsion Laboratory - California Institute of Technology - <https://www.jpl.nasa.gov/news/nasas-perseverance-rover-will-carry-first-spacesuit-materials-to-mars>.
- Nayak, G. C., & Das, C. K. (2015). LCP Based Polymer Blend Nanocomposites. In *Liquid Crystalline Polymers: Volume 1-Structure and Chemistry* (pp. 251–272). Springer International Publishing. https://doi.org/10.1007/978-3-319-22894-5_8
- Noel, C. (1992). Characterization of Mesophases. In A. A. Collyer (Ed.), *Liquid Crystal Polymers: From Structures to Applications* (pp. 31–101). Elsevier Science Publishers Ltd and The Society of Materials Science.
- Oproiu, C., Martin, D., Toma, M., Marghitu, S., & Jianu, A. (2000). Transitory and permanent effects of electron beam irradiation on insulating materials. *Nuclear Instruments and Methods in Physics Research B*, 669–675. www.elsevier.nl/locate/nimb
- Padias, A. B., & Hall, H. K. (2011). Mechanism studies of LCP synthesis. *Polymers*, *3*(2), 833–845. <https://doi.org/10.3390/polym3020833>

- Pavel, D. (2016). Introduction to Liquid Crystalline Polymers. In V. K. Thakur & M. R. Kessler (Eds.), *Liquid Crystalline Polymers* (Vol. 1, pp. 477–500). Springer International Publishing.
- Plis, E. A., Engelhart, D. P., Cooper, R., Johnston, W. R., Ferguson, D., & Hoffmann, R. (2019). Review of radiation-induced effects in polyimide. In *Applied Sciences (Switzerland)* (Vol. 9, Issue 10). MDPI AG. <https://doi.org/10.3390/app9101999>
- Radiation Institute, TU Delft. (n.d.). Retrieved October 10, 2024, from <https://www.tudelft.nl/en/faculty-of-applied-sciences/about-faculty/departments/chemical-engineering/principal-investigators/laurens-siebbeles/laurens-siebbeles-group/experimental-facilities/pulsed-high-energy-electron-accelerator-facilities>
- Reyes-Mayer, A., Alvarado-Tenorio, B., Romo-Uribe, A., & Jaffe, M. (2013). SALS, WAXS and mechanical properties of heat-treated thermotropic polymers. *Polymers for Advanced Technologies*, 24(12), 1029–1039. <https://doi.org/10.1002/pat.3177>
- Romo-Uribe, A. (2021). Shear-induced textures and viscoelasticity in the nematic and isotropic phase of semiflexible thermotropic polymers. A rheo-optical study. *Polymers for Advanced Technologies*, 32(2), 651–662. <https://doi.org/10.1002/pat.5118>
- Romo-Uribe, A., Reyes-Mayer, A., Calixto Rodriguez, M., & Sarmiento-Bustos, E. (2022). On the influence of thermal annealing on molecular relaxations and structure in thermotropic liquid crystalline polymer. *Polymer*, 240. <https://doi.org/10.1016/j.polymer.2021.124506>
- Slejko, E. A., Gregorio, A., & Lughì, V. (2021). Material selection for a CubeSat structural bus complying with debris mitigation. *Advances in Space Research*, 67(5), 1468–1476. <https://doi.org/10.1016/j.asr.2020.11.037>
- Smithers, G. A., Nehls, M. K., Hovater, M. A., Evans, S. W., Miller, J. S., Broughton, R. M., Beale, D., Kilinc-Balci, F., & Marshall, G. C. (2007). *A One-Piece Lunar Regolith Bag Garage Prototype*. <http://www.sti.nasa.gov>
- Stephen, M. J., & Straley, J. P. (1974). Physics of liquid crystals. *Reviews of Modern Physics*, 46(4), 618–701.
- TA Instruments. (n.d.). *Dynamic Mechanical Analysis - Basic Theory & Applications Training*.
- Tan, Z., Xia, Y., Zhao, M., Liu, X., Li, F., Huang, B., & Ji, Y. (2004). Electron stopping power and mean free path in organic compounds over the energy range of 20–10,000 eV. *Nuclear Instruments and Methods in Physics Research, Section B: Beam Interactions with Materials and Atoms*, 222(1–2), 27–43. <https://doi.org/10.1016/j.nimb.2004.02.017>
- Tanabashi, M., Hagiwara, K., Hikasa, K., Nakamura, K., Sumino, Y., Takahashi, F., Tanaka, J., Agashe, K., Aielli, G., Amsler, C., Antonelli, M., Asner, D. M., Baer, H., Banerjee, S., Barnett, R. M., Basaglia, T., Bauer, C. W., Beatty, J. J., Belousov, V. I., ... Schaffner, P. (2018). Review of Particle Physics. In *Physical Review D* (Vol. 98, Issue 3). American Physical Society. <https://doi.org/10.1103/PhysRevD.98.030001>
- Veerasingam, S., Ranjani, M., Venkatachalapathy, R., Bagaev, A., Mukhanov, V., Litvinyuk, D., Mugilarasan, M., Gurumoorthi, K., Guganathan, L., Aboobacker, V. M., & Vethamony, P. (2021). Contributions of Fourier transform infrared spectroscopy in microplastic

- pollution research: A review. *Critical Reviews in Environmental Science and Technology*, 51(22), 2681–2743. <https://doi.org/10.1080/10643389.2020.1807450>
- Venkatram, S., McCollum, J., Stingelin, N., & Brettmann, B. (2023). A close look at polymer degree of crystallinity versus polymer crystalline quality. *Polymer International*, 72(10), 855–860. <https://doi.org/10.1002/pi.6508>
- Von Sonntag, C. (2003). Free-radical-induced chain scission and cross-linking of polymers in aqueous solution—an overview. *Radiation Physics and Chemistry*, 67(3–4), 353–359. [https://doi.org/10.1016/S0969-806X\(03\)00066-5](https://doi.org/10.1016/S0969-806X(03)00066-5)
- Wallace, J. S., Sinclair, M., Gillen, K. T., & Clough, R. L. (1993). COLOR CENTER ANNEALING IN γ -IRRADIATED POLYSTYRENE, UNDER VACUUM AND AIR ATMOSPHERES. In *Radiat. Phys. Chm* (Vol. 41, Issue 2).
- Waller, J. M. (2020). *Simulated Galactic Cosmic Ray and Solar Particle Event Radiation Effects on Inflatable Habitat, Composite Habitat, Space Suit and Space Hatch Cover Materials*. <http://www.sti.nasa.gov>
- Waller, J., Peters, B., Rojdev, K., Nichols, C., & Hussain, S. (2017, July). Effect of Simulated Galactic Cosmic Ray (GCR) and Solar Particle Event (SPE) Radiation on Spectra[®] Restraint Fabric. *47th International Conference on Environmental Systems 16-20 July 2017*. <http://physics.nist.gov/PhysRefData/Star/Text/PSTAR.html>,
- Wiberg, G., & Gedde, U. W. (1998). Melting and recrystallization of a thermotropic liquid crystalline copolyester. *Thermochimica Acta*, 319, 123–129.
- Wissbrun, K. F., & Yoon, H. N. (1989). Similarity of dynamic mechanical transitions of thermotropic polyesters in extension and torsion. *POLYMER*, 2193–2197.
- Yuan, S. J., Peng, Z. Q., Rong, M. Z., & Zhang, M. Q. (2022). Increasing strengths of liquid crystalline polymers while minimizing anisotropy via topological rearrangement assisted bi-directional stretching of reversibly interlocked macromolecular networks. *Applied Materials Today*, 29. <https://doi.org/10.1016/j.apmt.2022.101643>

Appendices

Appendix A - Irradiation Report Van de Graaff Electron Accelerator



ELECTRON BEAM IRRADIATION

test date: 28-07-2023

report no: EB2309

order date: 30-5-2023
 ordered by: Caroline Houriet, Aerospace, Delft

purchase order: -

executed by: Lennart van den Hengel, Ferdinand Grozema, Faculty of Applied Sciences, Opto-electronic Materials, Mekelweg 15, 2629JB Delft.

purpose: 1 MeV irradiation of a series of tensile samples.

accelerator settings:

accel voltage	U = 1 MV	anode	350
scan setting	S = 300 mm	focus	300
scan width	Sw = 195 mm	bias	150
current	$I_e = 69 \mu\text{A}$	e.m. focus	0.54 A
table to scanner-		X-axis	-0.2 mm
distance	H = 30 cm	Y-axis	-0.8 mm

Dosimetry small samples: Irradiation with a beam current of 67.4 μA beam current resulted in an average dose of 37.9 kGy/cm^2 in 240 seconds.

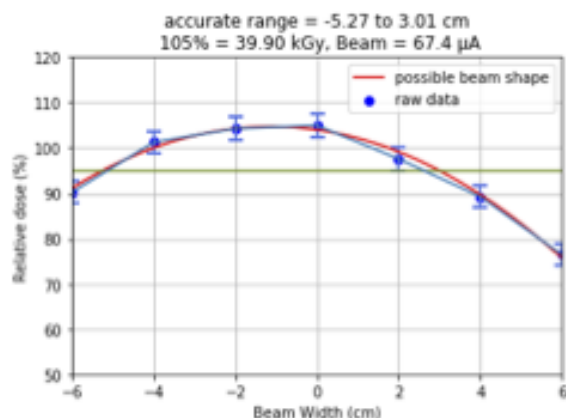


Figure 1. Dose distribution (beam shifted to align with middle of the samples afterwards)

It is known that 35 kGy in 240 seconds in these films is related to a fluency of $5e+11 \text{ e-/s}$, for small variations the relation between fluency and beam current is linear.

Thus, in order to reach this fluency a beam current of $(67.40 [\mu\text{A}] / 37.90 [\text{kGy}] * 35 [\text{kGy}]) = 62.24 \mu\text{A}$ is required.

date	time	sample ID's	I (μA)	D(needed) ($\text{e-}/\text{cm}^2$)	dose rate ($\text{e-}/\text{cm}^2/\text{s}$)	t_needed (s)	time set	exact dose ($\text{e-}/\text{cm}^2$)
28-7-2023	10:28	1e14 samples	64.8	$1.00E+14$	$5.20E+11$	192.30	193	$1.00E+14$
28-7-2023	10:48	1e15 samples	64.4	$1.00E+15$	$5.17E+11$	1934.97	1935	$1.00E+15$
28-7-2023	11:02	1e16 samples	67.5	$1.00E+16$	$5.42E+11$	18461.03	18461	$1.00E+16$

conditions: samples were handled by customer only, table temperature was monitored not to have exceeded 22 $^{\circ}\text{C}$.

also see: see irradiation procedure IRI 3.2, M.L. Hom, date 24/07/97

Appendix B - DSC Data Processing

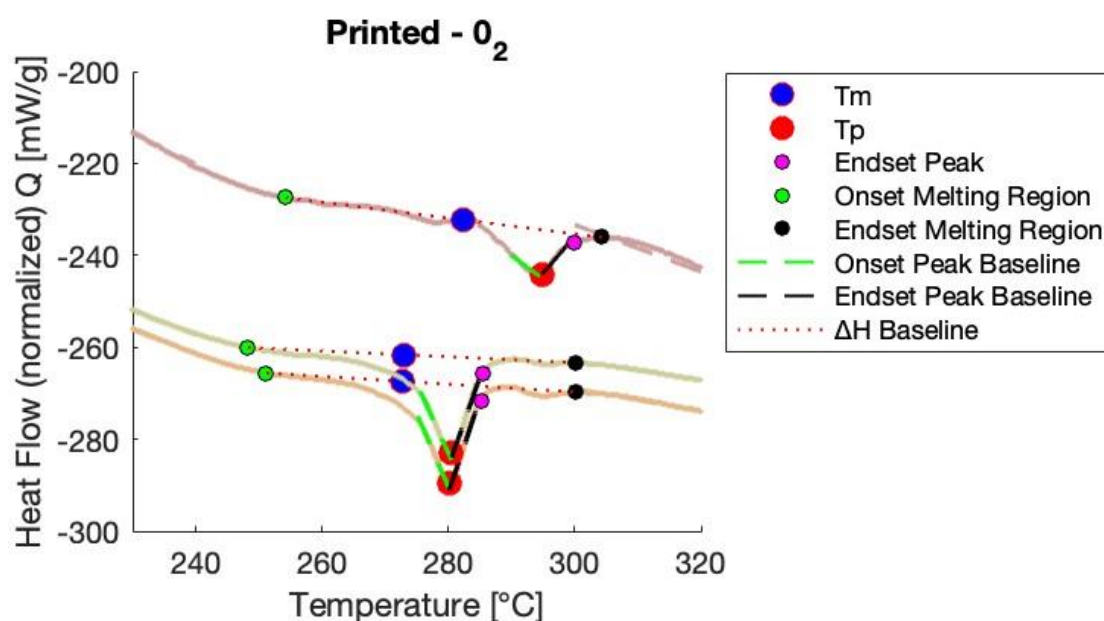
Endotherm down and Exotherm up, unless otherwise specified. Biggest peak taken, alternatively to the method for multiple peaks that look like it should have been 1 peak with an 'indent', it could be 'outdented' to take that out folded peak as the melting peak.

To find the start of a thermal transition, we look for the 'onset' point, which where the data first diverges by a set amount from the linear trend. To ensure the linear trend is not influence by other thermal transitions the region is chosen to be after the glass transition before the melting transition. The end of a thermal transition, or 'offset', is found using the same method in reverse.

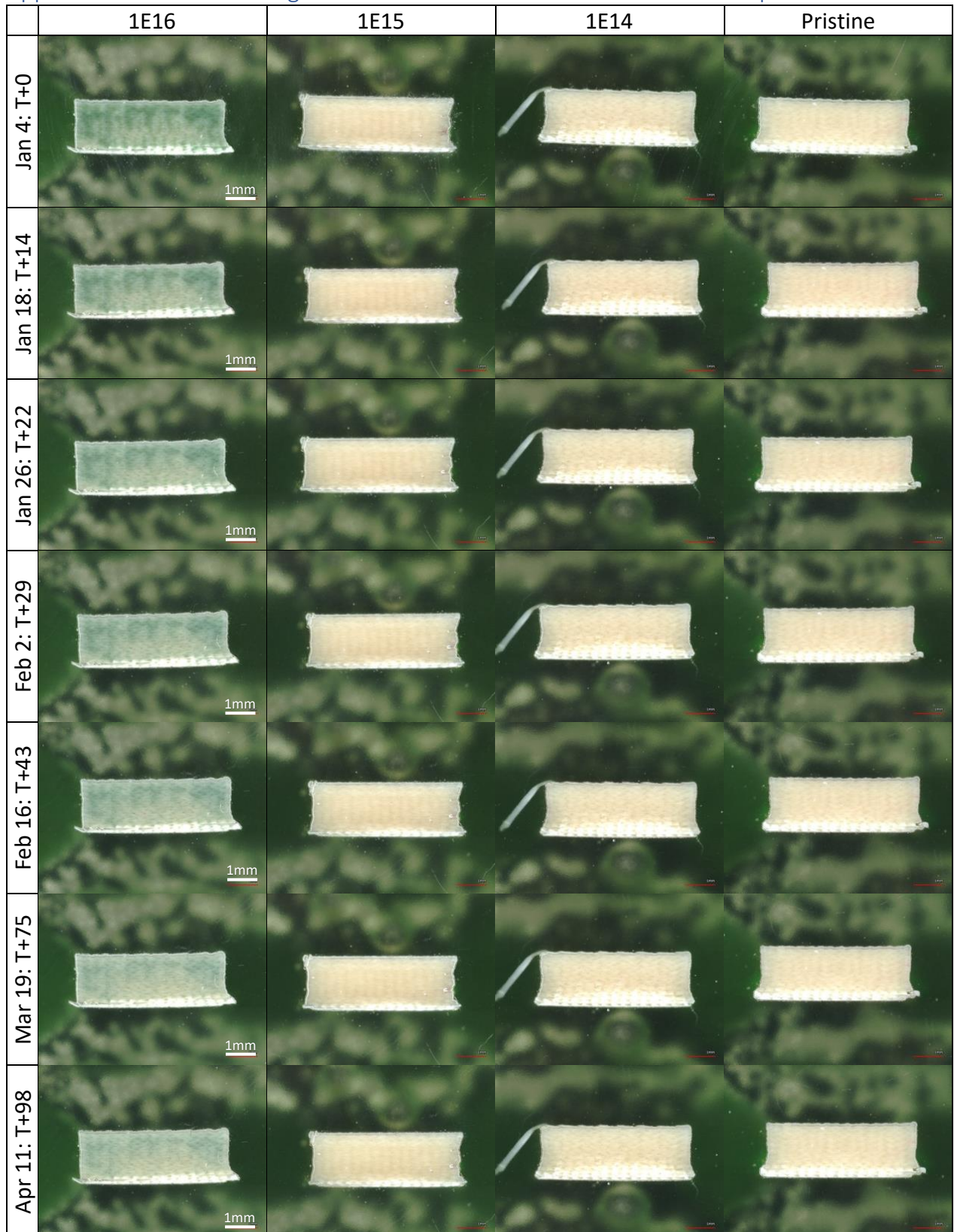
For heat cycles, the method of retrieving T_m by looking at where the on-set slope intersects the baseline between onset and off-set. Due to over-all not well-defined endotherms of the first heat cycle this method was chosen. For the well-defined and smooth cool cycles exotherms the onset point was taken to be the T_m , or solidification temperature.

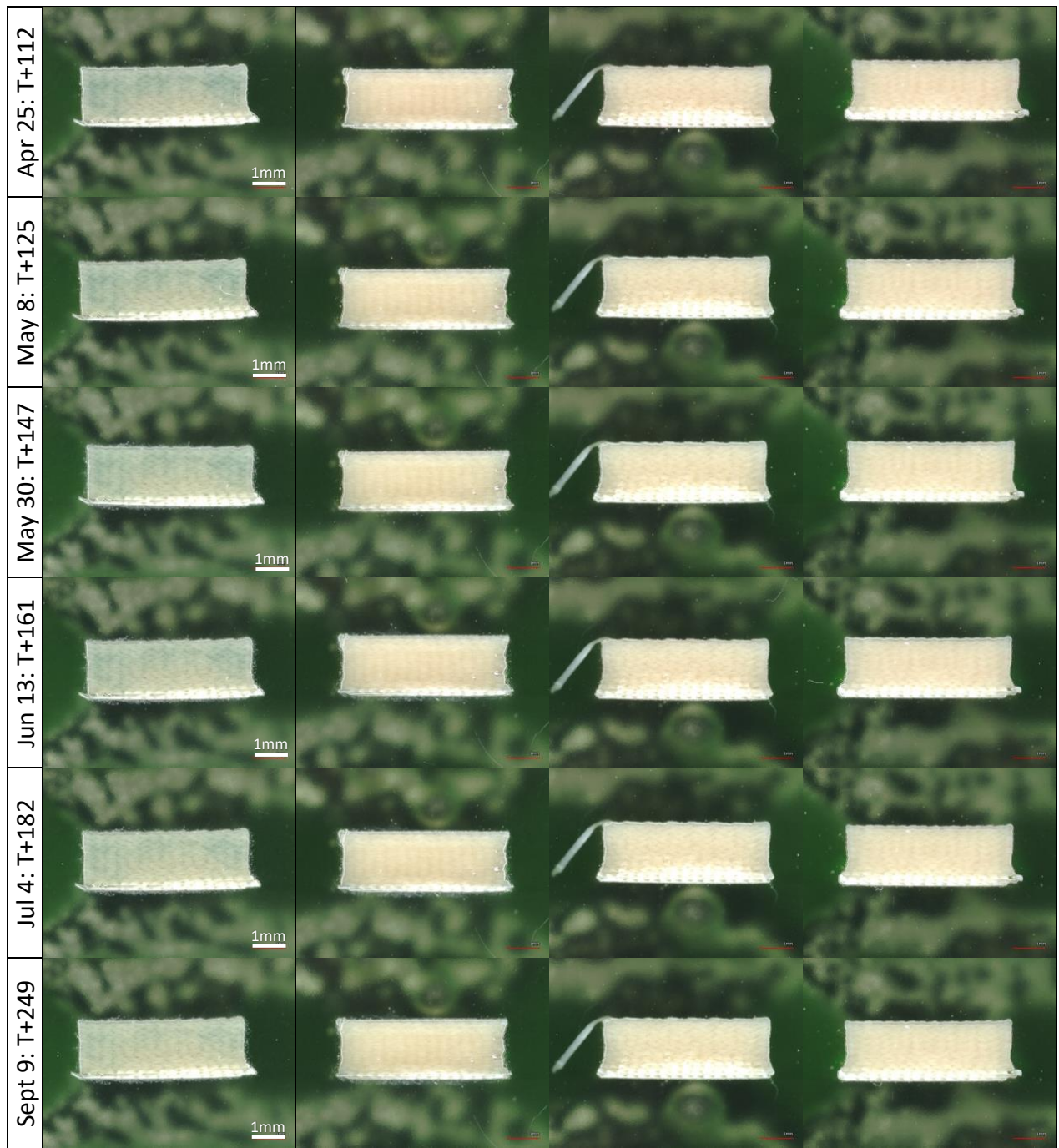
C_p is the onset slope endo/exotherm. Slope of line found in $[mW/g^{\circ}C] = [mJ/sg^{\circ}C] \rightarrow$ divide by heating rate in $[^{\circ}C/min]$ converted to $[^{\circ}C/sec]$ to get $[mJ/g^{\circ}C] \rightarrow$ divide by 1000, to get desired $[J/g^{\circ}C]$.

Trapezoidal rule was used to find the enthalpy of fusion. The Y value of the on-set is deducted from the Y value of the curve for the x-range of on-set to off-set of the endo/exotherm.



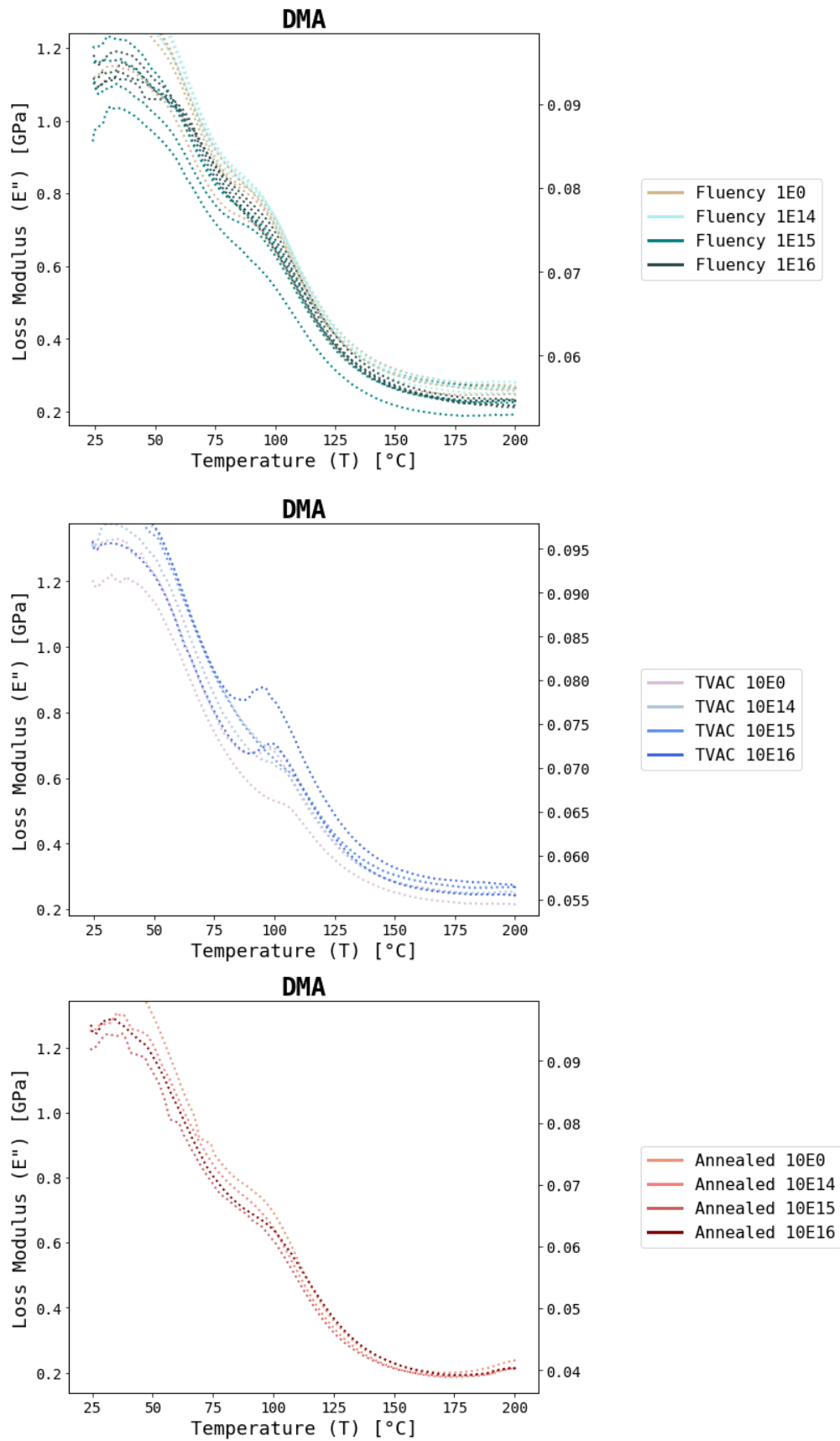
Appendix C – Color Tracking of FFF LCP Cross-Sections with VR Microscope





Appendix D - DMA

D.1 – DMA Loss Modulus Graphs

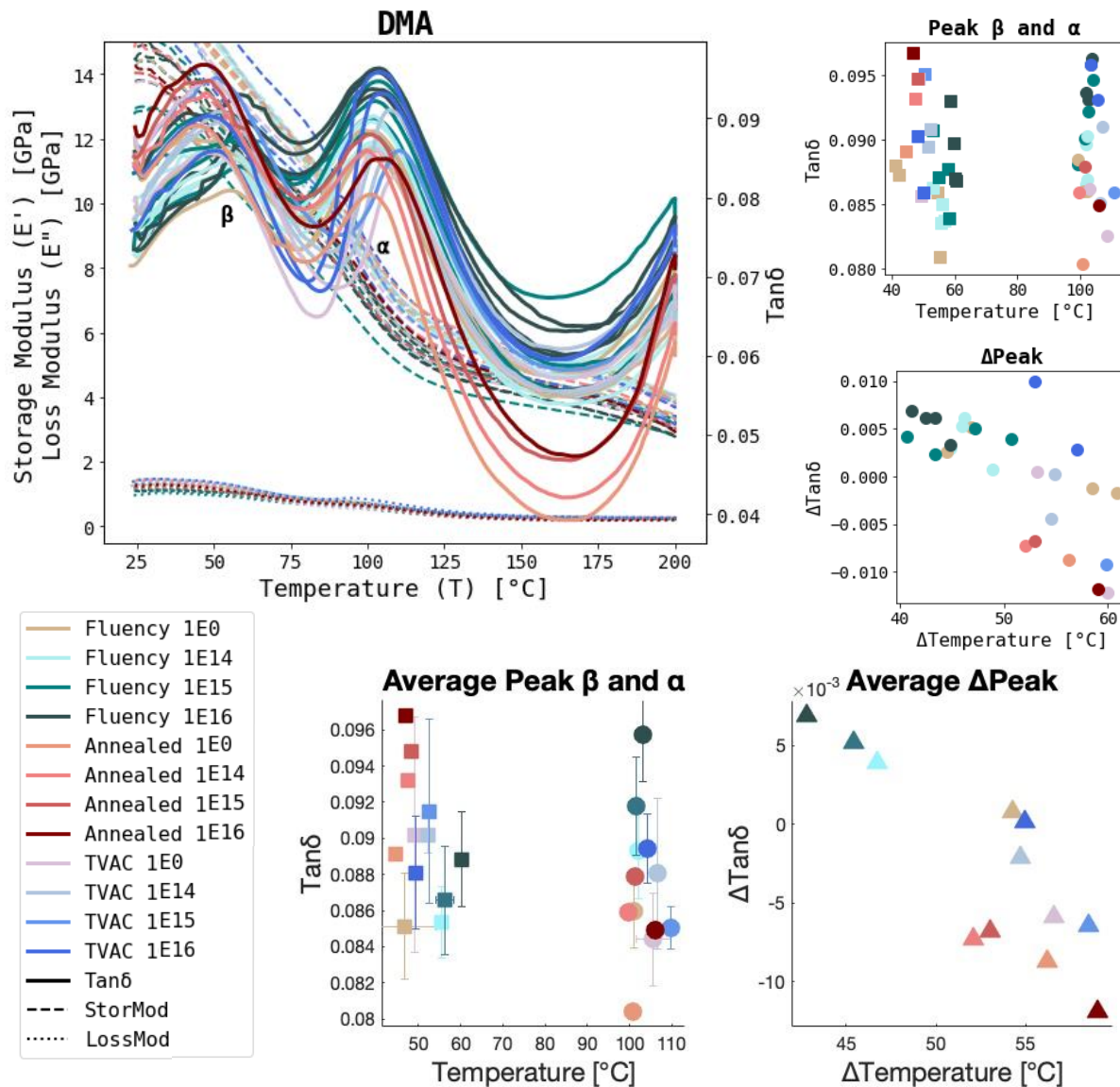


D.2 – Numerical Data DMA

Test	Fluence	Peak β		Peak α		Higher Peak	ΔT (°C)	$\Delta \text{Tan}\delta$
		Temp (°C)	Tan δ	Temp (°C)	Tan δ			
A1	pris	41.39	0.0881	102.26	0.0863	β	60.87	-0.0017
	low	55.56	0.0835	101.75	0.0896	α	46.19	0.0061
	mid	53.13	0.0907	103.85	0.0947	α	50.72	0.0040
	high	59.75	0.0898	103.16	0.0959	α	43.41	0.0061
A2	pris	55.17	0.0809	102.10	0.0860	α	46.93	0.0051
	low	56.78	0.0837	101.61	0.0866	α	44.83	0.0029
	mid	58.32	0.0839	99.07	0.0881	α	40.75	0.0041
	high	60.63	0.0868	101.74	0.0937	α	41.11	0.0069
A3	pris	54.60	0.0859	99.09	0.0885	α	44.49	0.0025
	low	53.27	0.0863	102.18	0.0870	α	48.91	0.0007
	mid	57.91	0.0878	101.31	0.0901	α	43.40	0.0023
	high	60.05	0.0870	102.52	0.0931	α	42.47	0.0061
A4	pris	42.54	0.0873	101.07	0.0861	β	58.53	-0.0013
	low	56.16	0.0850	102.17	0.0903	α	46.01	0.0053
	mid	55.15	0.0871	102.41	0.0922	α	47.26	0.0050
	high	58.68	0.0930	103.50	0.0963	α	44.82	0.0033
AT1	pris	49.42	0.0856	102.67	0.0862	α	53.25	0.0005
	low	51.74	0.0895	106.28	0.0851	β	54.54	-0.0044
	mid	50.70	0.0951	110.56	0.0859	β	59.86	-0.0092
	high	50.31	0.0859	103.24	0.0958	α	52.93	0.0099
AT2	pris	48.66	0.0948	108.56	0.0826	β	59.90	-0.0122
	low	52.23	0.0909	107.10	0.0910	α	54.87	0.0002
	mid	51.92	0.0879	109.12	0.0842	β	57.20	-0.0037
	high	48.31	0.0903	105.31	0.0931	α	57.00	0.0028
E1	pris	39.70	0.0835	100.15	0.0829	β	60.45	-0.0006
	low	55.28	0.0883	102.96	0.0931	α	47.68	0.0048
	mid	56.84	0.0834	101.89	0.0938	α	45.05	0.0105
	high	62.34	0.0875	104.38	0.0997	α	42.04	0.0122
E2	pris	53.51	0.0800	101.74	0.0864	α	48.23	0.0063
	low	54.21	0.0905	101.63	0.0968	α	47.42	0.0063
	mid	59.26	0.0874	101.76	0.0970	α	42.50	0.0095
	high	63.15	0.0840	103.51	0.0933	α	40.36	0.0093
D1	pris	44.54	0.0891	100.73	0.0804	β	56.19	-0.0087
	low	47.62	0.0932	99.69	0.0859	β	52.07	-0.0073
	mid	48.21	0.0948	101.21	0.0879	β	53.00	-0.0068
	high	46.93	0.0968	105.96	0.0849	β	59.03	-0.0119

D.3 – DMA Comparison

Test Group		Peak β		Peak α		ΔT (°C)	$\Delta \text{Tan}\delta$
		Temp (°C)	Tan δ	Temp (°C)	Tan δ		
Irradiated	Pris	48.4	0.086	101.1	0.087	52.7	0.0012
	Low	55.4	0.085	101.9	0.088	46.5	0.0038
	Mid	56.1	0.087	101.7	0.091	45.5	0.0038
	High	59.8	0.089	102.7	0.095	43.0	0.0056
Irradiated + TVAC	Pris	49.0	0.090	105.6	0.084	56.6	-0.0059
	Low	52.2	0.090	106.7	0.088	54.7	-0.0021
	Mid	52.6	0.092	109.8	0.085	58.5	-0.0065
	High	49.3	0.088	104.3	0.089	55.0	0.0002
Irradiated + Annealed	Pris	44.5	0.089	100.7	0.080	56.2	-0.0087
	Low	47.6	0.093	99.7	0.086	52.1	-0.0073
	Mid	48.2	0.095	101.2	0.088	53.0	-0.0068
	High	46.9	0.097	106.0	0.085	59.0	-0.0119



Appendix E - DSC Data

E.1 - DSC Data Irradiated

{'Heat cycle 1'}

	Tg (°C)	Cp (J/g°C)	Tm (°C)	Tp (°C)	ΔH (J/g)
Pristine - 46_1	98.31	-0.0049	280.9	292.82	-0.0355
Pristine - 46_2	90.55	-0.006	282.25	294.82	-0.0946
Low - 28_1	90.07	-0.0113	284.68	292.79	-0.164
Low - 28_2	100.32	-0.0051	283.41	294.27	-0.1087
Mid - 2_1	91.79	-0.0055	275.74	294.37	-0.0931
Mid - 2_2	89.91	-0.0205	286.35	291.79	-0.116
High - 34_1	102.24	-0.006	277.92	285.95	-0.0762
High - 34_2	93.59	-0.0259	279.63	284.08	-0.1085

{'Cool cycle 1'}

	Tg (°C)	Cp (J/g°C)	Tm (°C)	Tp (°C)	ΔH (J/g)
Pristine - 46_1	90.96	-0.0162	252.53	242.76	-0.1511
Pristine - 46_2	88.17	-0.0161	249.64	240.2	-0.1299
Low - 28_1	96.14	-0.0126	249.64	240.1	-0.141
Low - 28_2	91.18	-0.0147	250.67	239.11	-0.1651
Mid - 2_1	88.25	-0.0148	249.54	238.05	-0.1458
Mid - 2_2	90.4	-0.0195	248.67	239.69	-0.1333
High - 34_1	88.68	-0.0247	238.2	230.12	-0.1421
High - 34_2	91.04	-0.0307	237.72	230.74	-0.1347

{'Heat cycle 2'}

	Tg (°C)	Cp (J/g°C)	Tm (°C)	Tp (°C)	ΔH (J/g)
Pristine - 46_1	101.65	-0.0184	268.63	275.76	-0.2225
Pristine - 46_2	102.12	-0.019	272.75	280.14	-0.198
Low - 28_1	91.81	-0.0171	272.54	280.09	-0.1903
Low - 28_2	96.1	-0.0211	272.91	280.25	-0.2145
Mid - 2_1	96.75	-0.0209	272.65	279.92	-0.1925
Mid - 2_2	90.53	-0.0276	271.8	278.62	-0.2197
High - 34_1	100.85	-0.0172	265.1	272.87	-0.1902
High - 34_2	90.59	-0.0158	263.26	271.72	-0.2019

{'Cool cycle 2'}

	Tg (°C)	Cp (J/g°C)	Tm (°C)	Tp (°C)	ΔH (J/g)
Pristine - 46_1	91.2	-0.0084	250.42	234.86	-0.1671
Pristine - 46_2	88.03	-0.0159	248.61	238.43	-0.1619
Low - 28_1	92.05	-0.0155	248.2	238.12	-0.1378
Low - 28_2	94.98	-0.0183	248.62	238.05	-0.1748
Mid - 2_1	90.28	-0.0183	247.69	237.28	-0.13
Mid - 2_2	90.91	-0.0182	247.44	237.43	-0.127
High - 34_1	95.1	-0.0337	236.77	230.49	-0.1546
High - 34_2	88.75	-0.0398	236.06	230.64	-0.1355

{'Heat cycle 3'}

	Tg (°C)	Cp (J/g°C)	Tm (°C)	Tp (°C)	ΔH (J/g)
Pristine - 46_1	90.64	-0.0219	269.33	276.36	-0.2274
Pristine - 46_2	93.31	-0.018	272.89	280.51	-0.2031
Low - 28_1	94.16	-0.018	272.83	280.46	-0.2005
Low - 28_2	96.29	-0.0181	272.7	280.85	-0.2126
Mid - 2_1	93.87	-0.0184	272.72	280.46	-0.1925
Mid - 2_2	96.56	-0.028	271.85	278.86	-0.2226
High - 34_1	97.08	-0.0173	265.28	272.97	-0.1832
High - 34_2	93.39	-0.0164	263.66	272.1	-0.2002

ΔH for pristine_1 HC1 corrected

Tg appears to reset to 95°C for 3rd HC, not for 2nd HC, however DSC is not the most reliable way to retrieve Tg for crystalline materials.

HC 1 mean Tg 94.60°C – standard deviation $\sigma = 4.65^\circ\text{C}$

HC 2 mean Tg 96.30°C – standard deviation $\sigma = 4.60^\circ\text{C}$

HC 3 mean Tg 94.41°C – standard deviation $\sigma = 2.00^\circ\text{C}$

E.2 - DSC Data Pristine

{'Heat cycle 1'}					
	<u>Tg (°C)</u>	<u>Cp (J/g°C)</u>	<u>Tm (°C)</u>	<u>Tp (°C)</u>	<u>ΔH (J/g)</u>
Pellet - 0_1	94.25	-0.0024	269.46	295.27	-0.1506
Pellet - 0_2	101.01	-0.0145	277.17	282.84	-0.1698
Filament - 0_1	97.47	-0.0095	279.31	290.77	-0.1853
Filament - 0_2	93.24	-0.006	282.47	292.77	-0.1292
Printed - 0_1	98.31	-0.0049	280.9	292.82	-0.0355
Printed - 0_2	90.55	-0.006	282.25	294.82	-0.0946
{'Cool cycle 1'}					
	<u>Tg (°C)</u>	<u>Cp (J/g°C)</u>	<u>Tm (°C)</u>	<u>Tp (°C)</u>	<u>ΔH (J/g)</u>
Pellet - 0_1	92.67	-0.0223	245.93	236.51	-0.1705
Pellet - 0_2	100.01	-0.0179	247.2	236.88	-0.1587
Filament - 0_1	88.4	-0.0148	252.68	240.19	-0.1547
Filament - 0_2	92.42	-0.0102	254.48	238.06	-0.1472
Printed - 0_1	90.96	-0.0162	252.53	242.76	-0.1511
Printed - 0_2	88.17	-0.0161	249.64	240.2	-0.1299
{'Heat cycle 2'}					
	<u>Tg (°C)</u>	<u>Cp (J/g°C)</u>	<u>Tm (°C)</u>	<u>Tp (°C)</u>	<u>ΔH (J/g)</u>
Pellet - 0_1	102.3	-0.0403	275.99	284.04	-0.432
Pellet - 0_2	91.81	-0.0403	277.95	284.74	-0.3237
Filament - 0_1	103.43	-0.0278	273.58	280.03	-0.215
Filament - 0_2	96.72	-0.0177	272.86	281.49	-0.2507
Printed - 0_1	101.65	-0.0184	268.63	275.76	-0.2225
Printed - 0_2	102.12	-0.019	272.75	280.14	-0.198
{'Cool cycle 2'}					
	<u>Tg (°C)</u>	<u>Cp (J/g°C)</u>	<u>Tm (°C)</u>	<u>Tp (°C)</u>	<u>ΔH (J/g)</u>
Pellet - 0_1	92.02	-0.0784	239.75	235.67	-0.2164
Pellet - 0_2	94.94	-0.0657	239.73	235.38	-0.2092
Filament - 0_1	95.72	-0.0162	251.18	238.11	-0.1765
Filament - 0_2	92.57	-0.0163	251.05	238.13	-0.18
Printed - 0_1	91.2	-0.0084	250.42	234.86	-0.1671
Printed - 0_2	88.03	-0.0159	248.61	238.43	-0.1619
{'Heat cycle 3'}					
	<u>Tg (°C)</u>	<u>Cp (J/g°C)</u>	<u>Tm (°C)</u>	<u>Tp (°C)</u>	<u>ΔH (J/g)</u>
Pellet - 0_1	95.27	-0.0502	277.27	284.52	-0.4881
Pellet - 0_2	92.9	-0.0452	278.11	284.51	-0.3444
Filament - 0_1	97.99	-0.027	273.64	280.42	-0.2362
Filament - 0_2	100.66	-0.0169	273.54	281.83	-0.2352
Printed - 0_1	90.64	-0.0219	269.33	276.36	-0.2274
Printed - 0_2	93.31	-0.018	272.89	280.51	-0.2031

Tg appears to reset to 95°C for 3rd HC, not for 2nd HC, however DSC is not the most reliable way to retrieve Tg for crystalline materials.

HC 1 mean Tg 95.81°C – standard deviation $\sigma = 3.48^\circ\text{C}$

HC 2 mean Tg 99.67°C – standard deviation $\sigma = 4.11^\circ\text{C}$

HC 3 mean Tg 95.13°C – standard deviation $\sigma = 3.35^\circ\text{C}$

E.3 - DSC Data Annealed

{'Heat cycle 1'}

	Tg (°C)	Cp (J/g°C)	Tm (°C)	Tp (°C)	ΔH (J/g)
Pellet - 0_1	94.25	-0.0024	269.46	295.27	-0.1506
Pellet - 0_2	101.01	-0.0145	277.17	282.84	-0.1698
Pellet - 1_1	90.46	-0.0113	240.01	253.6	-0.7473
Pellet - 1_2	96.72	-0.0074	240	254.45	-0.7587
Pellet - 2_1	97.13	-0.0171	242.76	261.2	-0.8587
Pellet - 2_2	95.78	-0.0168	243.05	263.98	-0.7469
Pellet - 3_1	101.55	-0.0214	245.21	264.79	-1.1202
Pellet - 3_2	102.33	-0.0249	249	266.86	-1.0384
Pellet - 4_1	98.49	-0.0189	244.63	266.49	-1.1325
Pellet - 4_2	93.7	-0.0302	253.08	268.81	-1.0838
Pellet - 5_1	100.86	-0.017	246.61	273.9	-1.0707
Pellet - 5_2	94.06	-0.0237	250.01	269.49	-1.1471
Filament - 0_1	97.47	-0.0095	279.31	290.77	-0.1853
Filament - 0_2	93.24	-0.006	282.47	292.77	-0.1292
Filament - 1_1	102.69	-0.0195	240	250.02	-0.6719
Filament - 1_2	94.11	-0.0424	285.11	288.98	-0.7756
Filament - 2_1	92.75	-0.028	244.17	257.95	-0.8961
Filament - 2_2	100.88	-0.0262	243.01	258.12	-0.9069
Filament - 3_1	95.84	-0.0273	244.39	259.23	-0.9629
Filament - 3_2	98.82	-0.0195	242.49	258.55	-0.8626
Filament - 4_1	104.96	-0.0276	243.92	260.17	-1.0627
Filament - 4_2	99.32	-0.0258	244.17	261.42	-1.0111
Filament - 5_1	92.72	-0.0181	243.52	263.91	-1.012
Filament - 5_2	93.85	-0.0188	244	263.39	-1.011

{'Cool cycle 1'}

	Tg (°C)	Cp (J/g°C)	Tm (°C)	Tp (°C)	ΔH (J/g)
Pellet - 0_1	92.67	-0.0223	245.93	236.51	-0.1705
Pellet - 0_2	100.01	-0.0179	247.2	236.88	-0.1587
Pellet - 1_1	94.87	-0.0194	246.1	235.75	-0.1769
Pellet - 1_2	88.21	-0.0254	244.52	236.28	-0.1939
Pellet - 2_1	92.23	-0.0134	248.26	235.95	-0.1555
Pellet - 2_2	97.82	-0.0074	251.29	231.41	-0.2543
Pellet - 3_1	96.45	-0.015	248.22	236.75	-0.1368
Pellet - 3_2	96.01	-0.0129	248.66	236.57	-0.1668
Pellet - 4_1	94.3	-0.014	249.49	237.1	-0.1396
Pellet - 4_2	92.38	-0.0147	247.93	236.58	-0.1733
Pellet - 5_1	91.45	-0.0118	248.85	236.02	-0.1712
Pellet - 5_2	91	-0.0151	248.01	236.61	-0.1626
Filament - 0_1	88.4	-0.0148	252.68	240.19	-0.1547
Filament - 0_2	92.42	-0.0102	254.48	238.06	-0.1472
Filament - 1_1	92.3	-0.0129	251.36	237.95	-0.16
Filament - 1_2	88.49	-0.0112	254.49	238.36	-0.1606
Filament - 2_1	91.94	-0.0139	251.04	238.2	-0.1629
Filament - 2_2	93.66	-0.0145	250.11	237.78	-0.1624
Filament - 3_1	88.07	-0.0113	253.19	237.43	-0.151
Filament - 3_2	99.1	-0.0118	252.17	237.34	-0.1481
Filament - 4_1	90.84	-0.0137	251.77	238.07	-0.1705
Filament - 4_2	90.18	-0.0142	251.54	238.2	-0.1704
Filament - 5_1	93.24	-0.0158	250.72	237.99	-0.1611
Filament - 5_2	92.34	-0.0148	249.92	237.12	-0.1605

{'Heat cycle 2'}

	Tg (°C)	Cp (J/g°C)	Tm (°C)	Tp (°C)	ΔH (J/g)
Pellet - 0_1	102.3	-0.0403	275.99	284.04	-0.432
Pellet - 0_2	91.81	-0.0403	277.95	284.74	-0.3237
Pellet - 1_1	104.86	-0.0376	277.25	285.46	-0.4366
Pellet - 1_2	93.76	-0.0428	276.9	284.46	-0.4373
Pellet - 2_1	97.75	-0.042	276.51	283.62	-0.3649
Pellet - 2_2	90.91	-0.0478	276.2	283.26	-0.3964
Pellet - 3_1	97.56	-0.0393	276.45	283.98	-0.3938
Pellet - 3_2	96.02	-0.0381	276.23	284.13	-0.3814
Pellet - 4_1	96.01	-0.0449	275.97	282.76	-0.3748
Pellet - 4_2	97.29	-0.0389	275.79	283.06	-0.3489
Pellet - 5_1	95.97	-0.0351	275.88	283.05	-0.3143
Pellet - 5_2	94.84	-0.0367	274.98	282.18	-0.3277
Filament - 0_1	103.43	-0.0278	273.58	280.03	-0.215
Filament - 0_2	96.72	-0.0177	272.86	281.49	-0.2507
Filament - 1_1	96.2	-0.0204	273.32	281.36	-0.2336
Filament - 1_2	96.73	-0.0208	273.14	280.79	-0.2284
Filament - 2_1	93.42	-0.023	273.71	280.93	-0.2289
Filament - 2_2	96	-0.0197	273.56	281.45	-0.2198
Filament - 3_1	101.32	-0.0193	273.22	281.33	-0.2339
Filament - 3_2	95.55	-0.0164	273.31	282.02	-0.2289
Filament - 4_1	97.03	-0.0259	273.45	280.25	-0.2307
Filament - 4_2	95.87	-0.0246	273.35	280.25	-0.2258
Filament - 5_1	98.18	-0.0204	273.15	280.99	-0.246
Filament - 5_2	95.55	-0.0163	273.59	282.04	-0.2374

{'Cool cycle 2'}

	Tg (°C)	Cp (J/g°C)	Tm (°C)	Tp (°C)	ΔH (J/g)
Pellet - 0_1	92.02	-0.0784	239.75	235.67	-0.2164
Pellet - 0_2	94.94	-0.0657	239.73	235.38	-0.2092
Pellet - 1_1	92.06	-0.0644	239.67	235.28	-0.235
Pellet - 1_2	88.26	-0.0707	239.69	235.55	-0.192
Pellet - 2_1	100.84	-0.0711	240.04	235.63	-0.2248
Pellet - 2_2	94.67	-0.0491	241.96	235.76	-0.1999
Pellet - 3_1	88.44	-0.046	241.85	235.78	-0.2148
Pellet - 3_2	89	-0.0381	242.81	235.63	-0.2177
Pellet - 4_1	92.54	-0.0382	243.57	236.22	-0.226
Pellet - 4_2	88.43	-0.0454	242.02	235.72	-0.196
Pellet - 5_1	89.81	-0.0347	243.05	235.57	-0.2074
Pellet - 5_2	93.57	-0.0304	243.95	235.6	-0.1892
Filament - 0_1	95.72	-0.0162	251.18	238.11	-0.1765
Filament - 0_2	92.57	-0.0163	251.05	238.13	-0.18
Filament - 1_1	91.44	-0.0171	250.18	237.93	-0.1764
Filament - 1_2	91.5	-0.0159	251.76	238.33	-0.1809
Filament - 2_1	91.02	-0.017	249.85	237.74	-0.1749
Filament - 2_2	89.02	-0.0233	247.16	237.76	-0.1831
Filament - 3_1	92.75	-0.0178	249.74	237.5	-0.1743
Filament - 3_2	95.96	-0.0206	248.35	237.52	-0.1798
Filament - 4_1	96.01	-0.0163	250.13	237.25	-0.179
Filament - 4_2	90.36	-0.0165	249.87	237.26	-0.1796
Filament - 5_1	90.42	-0.0243	248.34	238.12	-0.1826
Filament - 5_2	92.39	-0.0186	248.97	237.34	-0.1744

{'Heat cycle 3'}

	Tg (°C)	Cp (J/g°C)	Tm (°C)	Tp (°C)	ΔH (J/g)
Pellet - 0_1	95.27	-0.0502	277.27	284.52	-0.4881
Pellet - 0_2	92.9	-0.0452	278.11	284.51	-0.3444
Pellet - 1_1	91.67	-0.0371	277.9	285.74	-0.4085
Pellet - 1_2	91.96	-0.0467	278.53	284.74	-0.3321
Pellet - 2_1	88.75	-0.0525	278.1	285.1	-0.4432
Pellet - 2_2	99.63	-0.0594	277.39	284.25	-0.4967
Pellet - 3_1	98.99	-0.0447	277.44	284.63	-0.4369
Pellet - 3_2	94.54	-0.0459	277.56	284.89	-0.4575
Pellet - 4_1	94.13	-0.0533	277.23	284.17	-0.4715
Pellet - 4_2	96.39	-0.048	277.4	284.51	-0.4381
Pellet - 5_1	100.71	-0.0439	277.73	285.18	-0.4179
Pellet - 5_2	96.96	-0.06	277.38	284.12	-0.4672
Filament - 0_1	97.99	-0.027	273.64	280.42	-0.2362
Filament - 0_2	100.66	-0.0169	273.54	281.83	-0.2352
Filament - 1_1	96.1	-0.0181	273.22	281.84	-0.2415
Filament - 1_2	92.37	-0.0187	272.98	281.24	-0.2431
Filament - 2_1	93.96	-0.0209	273.61	281.37	-0.2317
Filament - 2_2	91.62	-0.0177	273.42	281.86	-0.227
Filament - 3_1	102.55	-0.019	273.6	281.72	-0.2434
Filament - 3_2	97.3	-0.0146	273.27	282.33	-0.2222
Filament - 4_1	96.74	-0.0262	273.57	280.47	-0.2344
Filament - 4_2	91.25	-0.0248	273.59	280.52	-0.2307
Filament - 5_1	93.36	-0.0182	273.17	281.28	-0.2273
Filament - 5_2	94.89	-0.0153	273.71	282.35	-0.2347

HC3 approaches a Tg of 95°C, however still with a significant standard deviation.

HC 1 mean Tg 97.21°C – standard deviation $\sigma = 3.78^\circ\text{C}$

HC 2 mean Tg 96.88°C – standard deviation $\sigma = 3.25^\circ\text{C}$

HC 3 mean Tg 95.45°C – standard deviation $\sigma = 3.41^\circ\text{C}$

Tm&Tp for Fil1_2 HC1 corrected

Filament 1_1 & 1_2 both have two endothermic peaks in HC1, for F1_2 the second peak is slightly bigger, which explains the deviating Tm and Tp of this sample.

Ts1 fil = X pel = 236.36°C

Ts2 fil = 237.749°C Pel = 235.64°C

Appendix F – FTIR Characteristic Peak Assignments

Wavelength (cm ⁻¹)	Functional group
3600 - 3200	O-H stretching
3024	Aromatic CH stretching
2992, 2966, 2960, 2950, 2949, 2932, 2922, 2920, 2917, 2915, 2865, 2858, 2855, 2848, 2847, 2845, 2838	C-H stretching
2917, 2849	=C-H stretching
1768, 1743, 1740, 1731, 1721, 1713, 1634, 1223	C=O stretching
1605, 1167	C=C stretching
1602, 1601, 1503, 1494, 1492, 1409, 904	Aromatic ring stretching
1451, 1331, 1255, 1166, 964, 904, 840	C-H bending
1241, 1238, 1223, 1186, 1158, 1141, 1094, 1020	C-O stretching / C(=O)O stretching
1099, 997, 808	C-C stretching
1027	Aromatic CH bending
1013	Aromatic CH in plane bending
967, 966, 759	=C-H bending
828, 759, 720, 698, 694, 537	Aromatic CH out-of-plane bending
808	C-CH stretching
750, 687	C=O bending
600	O-H bending
(Veerasingam et al., 2021)	